Universität Hamburg
DER FORSCHUNG | DER LEHRE | DER BILDUNG

Formation of dense gaseous structures in disc galaxies via spiral arms, magnetic fields and self-gravity

by

Raghav Arora

Dissertation
zur Erlangung des Doktorgrades
an der Fakultät für Mathematik, Informatik und Naturwissenschaften
Fachbereich Physik
der Universität Hamburg

Hamburg
March 2025

Declaration of oath

I hereby declare and affirm that this doctoral dissertation is my own work and that I have not used any aids and sources other than those indicated.

If electronic resources based on generative artificial intelligence (gAI) were used in the course of writing this dissertation, I confirm that my own work was the main and value-adding contribution and that complete documentation of all resources used is available in accordance with good scientific practice. I am responsible for any erroneous or distorted content, incorrect references, violations of data protection and copyright law or plagiarism that may have been generated by the gAI.

Hamburg, 29/03/2025

City, Date

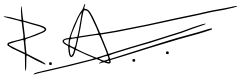

Signature

Gutachter/innen der Dissertation:	Prof. Dr. Robi Banerjee Prof. Christoph Federrath
Zusammensetzung der Prüfungskommission:	Prof. Dr. Robi Banerjee Prof. Christoph Federrath Prof. Mark Krumholz Prof. Dr. Jochen Liske Prof. Dr. Marcus Brüggen
Vorsitzende/r der Prüfungskommission:	Prof. Dr. Jochen Liske
Datum der Disputation:	21/05/2025
Vorsitzender des Fach-Promotionsausschusses PHYSIK:	Prof. Dr. Wolfgang J. Parak
Leiter des Fachbereichs PHYSIK:	Prof. Dr. Markus Drescher
Dekan der Fakultät MIN:	Prof. Dr.-Ing. Norbert Ritter

Contents

Acknowledgements

I find it rather hard to capture the gratitude I feel. Nonetheless, I hope to represent a sliver of this truth here.

I feel to be in a very privileged position, that I am allowed to pursue and spend time in such an esoteric profession. Countless events that were out of my control had to align together to make this possible, and so I acknowledge this coincidental confluence. Born at the right time in history, in the right country, city and to the right parents and family. I acknowledge the presence of this inherent randomness in my initial conditions, and the unpredictable, sauntering path that lead me here.

I acknowledge the nameless people in the society that oil and keep in motion the different cogs that must work together, in order for me to sustain myself. Be it the farmer, the worker in factories, the public servant, the doctor, the merchant, or the cleaner.

I acknowledge all those who have supported my tepid inclination towards science throughout these years. My parents and brother (bha), who incubated my interests and have sacrificed their own for my sake. The teachers at school, cram school, and at the university, who encouraged questions and fostered my curiosity. Who showed me glimpses of rational beauty, with nothing more than a chalk and a blackboard. All my friends and connections I made along the way, who showed solidarity in tough times and gave meaning to my joys. I cannot attempt to name you all - but if you care to read this, you are probably one of them.

Lastly, I would like to express my gratitude towards my supervisors - Robi Banerjee, Christoph Federrath, Mark Krumholz and Bastian Körtgen. Who have displayed immense patience over the years and have helped me mature as a researcher and a person. If it weren't for their opportunities, their encouragement for my ideas, their careful eye, or their advice and insight. None of this work would have been possible.

As a finishing note, I repeat what was recently spoken to me: "Umuntu ngumuntu ngabantu", which is Zulu for "A person is a person through other people".

Abstract

Dense structure in nearby spiral galaxies exhibits partial spatial regularity on kiloparsec scales. This is displayed both by the clumps arranged in beads-on-a-string pattern along spiral arms, and by filamentary features called feathers in the inter-arm regions. Both have shown evidence of hosting active star forming regions and young stellar clusters within them, making them important for gauging initial conditions for star formation. Their spatial regularity hints at galactic instabilities playing a part in their origin.

We study the role of gravity, spiral arms and magnetic fields on the formation of dense clumps in the arm and feathers in the inter-arm regions of disc galaxies. We do this by running a suite of global magnetohydrodynamical simulations of isolated disc galaxies.

We find that the spiral arm instability can give rise to semi-regularly spaced dense clumps along its length, that agree with the range found in observations. However, these clumps do not shear into the inter-arm regions to give rise to feathers. Moreover, the instability is affected by the presence of ubiquitous magnetic fields, depending upon their initial strength. Moderate magnetic fields stabilise the spiral arms via magnetic pressure, while weak initial fields destabilise them by increasing the growth rate within a factor of two. We find indications of the Parker instability in action in the latter case, which wasn't captured in earlier works due to their local, 2D approximations.

Furthermore, our galaxies form feathers via global galactic-scale gravitational instability, independent of the need of spiral arms or magnetic fields, contrary to what was suggested in previous works. This behaviour is quantified by the Toomre-Q parameter of the galaxy. We find that the morphological properties of feathers and timescales of their formation depend upon a second dimensionless parameter of the galaxy - the rotational mach number $\mathcal{M}_{\rm c} = v_{\rm c}/c_{\rm s}$ (ratio of the circular velocity to the sound speed). We find that our empirical scaling of feather spacing with $\mathcal{M}_{\rm c}$ agrees well with the available observations of nearby galaxies. This hints at a much simpler explanation for the origin of feathers.

Zusammenfassung

Die dichte Struktur in nahen Spiralgalaxien weist eine teilweise räumliche Regelmäßigkeit auf Kiloparsec-Skalen auf. Dies zeigt sich sowohl in den Klumpen, die wie Perlen an einer Kette entlang der Spiralarme angeordnet sind, als auch in fadenförmigen Ausbildungen, die Federn genannt werden, in den Regionen zwischen den Armen. Beide haben Anzeichen dafür geliefert, dass sie aktive Sternentstehungsgebiete und junge Sternhaufen beherbergen, was sie für die Beurteilung der Anfangsbedingungen für die Sternentstehung wichtig macht. Ihre räumliche Regelmäßigkeit deutet auf galaktische Instabilitäten hin, die bei ihrer Entstehung eine Rolle spielen.
Wir untersuchen die Rolle der Schwerkraft, der Spiralarme und der Magnetfelder bei der Bildung von dichten Klumpen in den Armen und Federn in den Regionen zwischen den Armen von Scheibengalaxien. Dazu führen wir eine Reihe globaler magnetohydrodynamischer Simulationen von isolierten Scheibengalaxien durch.
Wir stellen fest, dass die Instabilität des Spiralarms zu Klumpen mit halbwegs regelmäßigen Abständen entlang seiner Länge führen kann, die mit dem in Beobachtungen gefundenen Bereich übereinstimmen. Diese Klumpen führen jedoch nicht notwendigerweise zur Bildung der Federn. Darüber hinaus wird die Instabilität durch das Vorhandensein von Magnetfeldern beeinflusst, je nach deren anfänglicher Stärke. Mäßig starke Magnetfelder stabilisieren die Spiralarme durch magnetischen Druck, während schwache Anfangsfelder sie destabilisieren, indem sie die Wachstumsrate um einen Faktor zwei erhöhen. Im letzteren Fall finden wir Hinweise auf die Parker-Instabilität, die in früheren Arbeiten aufgrund ihrer lokalen 2D-Näherungen nicht erfasst wurde.
Darüber hinaus bilden unsere Galaxien Federn durch eine globale Gravitationsinstabilität auf galaktischer Ebene, unabhängig von der Notwendigkeit von Spiralarmen oder magnetischen Feldern, im Gegensatz zu dem, was in früheren Arbeiten vorgeschlagen wurde. Dieses Verhalten wird durch den Toomre-Q-Parameter der Galaxie quantifiziert. Wir stellen fest, dass die morphologischen Eigenschaften der Federn und die Zeitskala ihrer Entstehung von einem zweiten dimensionslosen Parameter der Galaxie abhängen - der Rotations-Machzahl $\mathcal{M}_\mathrm{c} = v_\mathrm{c}/c_\mathrm{s}$ (Verhältnis der Kreisgeschwindigkeit zur Schallgeschwindigkeit). Wir stellen fest, dass unsere empirische Skalierung des Federabstands mit $\mathcal{M}_\mathrm{c}$ gut mit den verfügbaren Beobachtungen naher Galaxien übereinstimmt. Dies deutet auf eine viel einfachere Erklärung für den Ursprung der Federn hin.

List of Figures

List of prior publications

The following articles have been published during the undertaking of this dissertation

1. Role of magnetic fields in disc galaxies: spiral arm instability Raghav Arora, Christoph Federrath, Robi Banerjee, Bastian Körtgen A&A 687 A276 (2024) DOI: 10.1051/0004-6361/202348719

2. Formation of filaments and feathers in disc galaxies: Is self-gravity enough? Raghav Arora, Christoph Federrath, Mark Krumholz, Robi Banerjee A&A 695 A155 (2025) DOI: 10.1051/0004-6361/202453501

1 Introduction

Stars studding the night sky have always formed an essential part of our world-view. Owing to the limitations of our visual receptors, that are sensitive only to a narrow range of electromagnetic radiation, we were left with a biased view of it. One dominated by a concentrated curving band of stars obscured with dark spots scattered across its length. Hindu traditions from South Asia, saw this band as a manifestation of the (holy) river Ganges in the sky and named it आकाशगंगा (Akashganga): the sky Ganges. The Swedes called it Vintergatan, meaning the winter street. The Greeks named it Γαλαξίας (Galaxias), derived from the word 'Gala' meaning milk. The word's literal translation has been adapted by the scientific community to name the band and our own galaxy as the well-known Milky Way. While the Greek word itself has been used to name galaxies in general. Today, galaxies are roughly defined as "a gravitationally bound stellar system with gas and dark matter within a particular size and mass range". The name or its description, does not conjure the symbolic milky appearance, nor metaphors or stories connected with our daily lives. But reflects the transition and abstraction of our world-view towards falsifiable scientific knowledge.
Even in the scientific community, the word *galaxies* was adopted only at the start of the last century and has undergone its own evolution. Before this, they were known as nebulae and were still considered to be a part of the Milky Way, rather than being entities similar to and separate from it. This is because of their diffusive appearance in old telescopes, that was reminiscent of gas clouds. The transformation happened after what is known as the great debate between the two astronomers - Harlow Shapley and Heber Curtis in 1920. Shapely was in motion for the nebulae lying on the outskirts of the Milky Way, while Heber pressed that they were independent objects or 'island universes' like the Milky Way. The debate had more at stake than just the distance of these peculiar objects - Shapley's argument implied that the Milky Way was the extent of the universe, while Heber's side inflated its size by orders of magnitude. The debate was settled later in the decade in favour of the island universes hypothesis with fresh observations from Edwin Hubble, who estimated the distance of the Andromeda galaxy (then nebula). This turned out to be too far to lie within our galaxy and established it as the first island universe. Today, we know that the universe is brimming with galaxies - with Milky Way being one of trillions in the observable universe.
Milky Way is a disc galaxy, with grand-design spiral arms, a central bar and a bulge of old stars near the centre. Apart from us residing within one, disc galaxies are of particular interest because they harbour majority of star formation activity in the current epoch. These are relatively gas-rich flattened disc systems with well-defined rotation profiles. The gas present in between the stars in such a galaxy, is invariably responsible for all star formation activity, and is subject to the physical conditions prevalent inside it. The gas's systematic motion, for instance, largely follows the rotation profile of the galaxy and is confined within the thin-plane of the disc. While its turbulent motion is mediated by instabilities. Moreover, the rotating gas is also subject to its self-gravity, large scale magnetic fields, gravity of background stars etc. The focus of the current work is to study the effects of these different physical processes on gas in a galaxy. Particularly, we study the role of galactic-scale gas instabilities in forming dense structures in disc galaxies that might lead to star formation.
The following sections give a brief overview of topics that contextualise the work

in more detail. Section 1.1 outlines the gaseous medium present between stars in a galaxy, Section 1.2 gives an overview of star formation in galaxies, Section 1.3 goes into the details of the observed dense gas distribution in nearby galaxies and Section 1.4 deals with the theoretical background of various galactic instabilities that could dictate this organisation. Finally, in Section 1.5, we present an overview of galaxy simulations and why they have become a necessary tool in galaxy evolution studies.

1.1 The interstellar medium

> "Hier ist wahrhaftig ein Loch im Himmel."
>
> Herschel (1785)

The interstellar medium (ISM) is the baryonic matter present between stars in a galaxy. Without considering the dark matter that dominates the mass budget, the gas mass fraction of the ISM in nearby star forming galaxies is merely around 10% of the total (Aditya, 2023), mostly being dominated by stars. Despite this low number, which has reduced with cosmic evolution (Fensch and Bournaud, 2021), the ISM still plays a pivotal role in galaxy evolution.

The ISM is a complex amalgamation of many constituents. It consists of neutrals, charged species threaded by magnetic fields, cosmic rays and photons. Dominated largely by primordial H and He, heavier elements are present in varying quantities and forms (e.g. dust), albeit with abundances a few orders of magnitude less than the two (for detailed solar abundances see Asplund et al., 2009). These are synthesised in stellar nucleosynthesis (till Fe) and explosions (heavier than Fe). Coincidently, it was the peculiar behaviour of one of the lines of one such element, that sparked the discovery of this medium between stars. Hartmann (1904), while taking the spectra of the spectroscopic binary δ Orionis, realised that the CaII H and K lines in the spectrograph remained narrow and stationary, in contrast to the other Doppler broadened lines as was expected from the motion of the binary. This lead to the hypothesis of an intervening medium between the stars.

Other than acting as observational diagnostics for probing the medium, the elemental composition of the ISM also dictates the thermodynamics of the gas by deciding the dominant heating and cooling processes. Heating processes include photoelectric heating from small dust grains, Polycyclic Aromatic Hydrocarbons (PAHs), heating and ionisation from cosmic rays and X-rays etc. Cooling arises from atomic, rotational and vibrational lines of various atomic and molecular species such as CO, H_2, CII etc. The dominance of cooling due to the OI and CII lines, results in the thermal instability at densities $n \sim 1$ cm^{-3} (Koyama and Inutsuka, 2000). This can create dense, cold molecular clouds from the warm, diffuse ISM (Koyama and Inutsuka, 2002; Vazquez-Semadeni et al., 2007; Hennebelle et al., 2008).

Figure 1 shows a modern view of the ISM in the nearby star forming spiral galaxy NGC 628 in different wavelength bands and exhibits the rich diversity of emission in them. The image is taken from a recent multi-wavelength survey Physics at High Angular resolution in Nearby GalaxieS [1], that takes advantage of the complex composition of

[1] https://sites.google.com/view/phangs/home

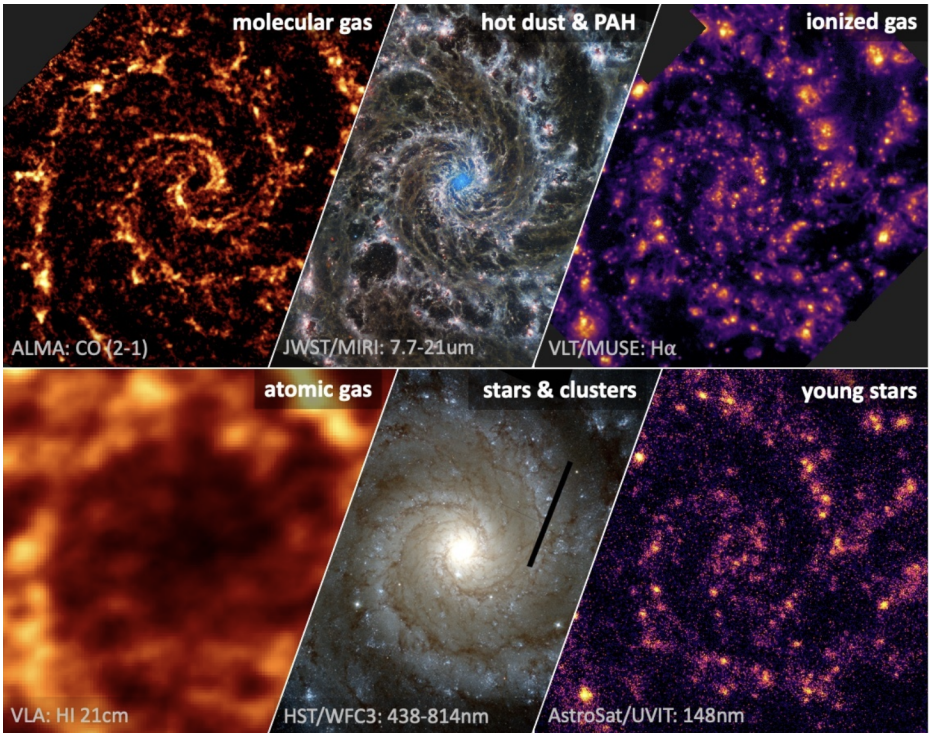

Figure 1: The galaxy NGC 628 as seen in various bands, tracing the different phases and constituents of the ISM. See text for details. Credits: Jiyayi Sun and PHANGS collaboration.

the ISM to probe different gas phases (Cox, 2005). Starting with the first row, the left-most panel shows the dense ($n \gtrsim 100$ cm^{-3}), cold ($T \lesssim 10$ K), molecular (H_2) gas phase as traced by the CO (2-1) transition at 2.6 mm by the ALMA interferometer. The middle-panel is emission from dust comprised of PAHs in the range 7.7–21 μm, taken from the JWST/MIRI instrument, which has recently been shown to trace the total gas content (Chown et al., 2024; Sandstrom et al., 2023). The upper-right row is $H\alpha$ emission that traces the ionised gas ($n \approx 0.1$ cm^{-3}, $T \approx 8000$ K) from the VLT using the MUSE instrument. For the bottom row, the left panel is the neutral atomic gas ($n \approx 0.1$–50 cm^{-3}, $T \approx 50$–5000 K) using the HI 21 cm emission from the VLA. The middle one is stellar component taken from the HST. And lastly, on the bottom right is the UV emission from young massive stars from AstroSat.
These different phases of the ISM are used as diagnostics of physical processes in the galaxy: Hα and UV emission, which result from ionising radiation due to massive stars, are used to estimate star formation rates. The distinct organisation of the cold, molecular gas in the form of spirals and the regularly spaced inter-arm features visible in dust emission, as we will see later, could be indications of the response of the gas to galactic instabilities.

1.2 Star formation

Ultimately, all stars in a galaxy are sourced from the ISM. This plants star formation as an innate cog of galaxy evolution. The phenomena acts both as a *sink*, as well as a *source* of baryons. Nascent stars are born out of the gas in the ISM, some of it (chemically enriched and dusty) is injected back into it while a fraction is lost

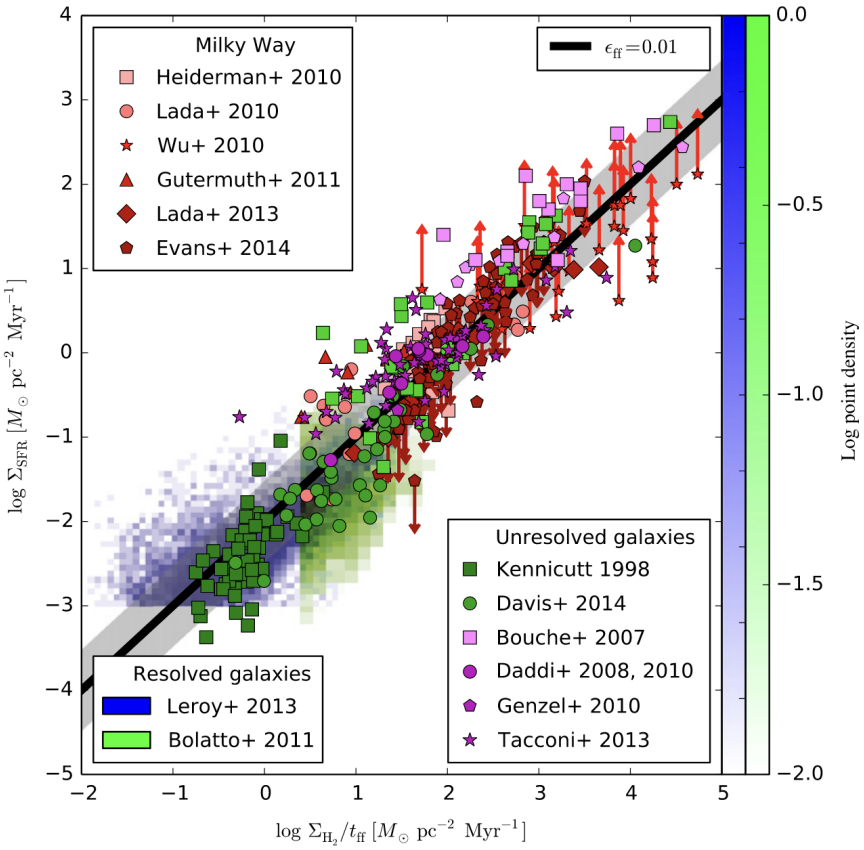

Figure 2: Example of a Kennicutt-Schmidt relation. The plot shows the observed molecular gas surface densities $\Sigma_{\rm H_2}$ normalised by the free-fall time $t_{\rm ff}$, against the star formation rate surface densities $\Sigma_{\rm SFR}$. The dataset spans Milky Way clouds, resolved galaxies and unresolved galaxies at $z = 0$ and $z > 0$ (magenta points) compiled from various sources as indicated in the legend. The black line is a fit with $\epsilon_{\rm ff} = 0.01$, with the grey bands showing a factor of three scatter around this value. The figure is taken from Krumholz (2014).

in the formation of compact objects such as white dwarfs, neutron stars and black holes. These injection mechanisms come in myriad forms, each with their own energy budget and a range of relevant spatial scales that are affected by them. These include protostellar outflows, photoionisation, radiation pressure, winds from massive stars and supernovae (Dale, 2015). Feedback from stars drive gas flows by spewing radiation and depositing energy and momentum, even on kiloparsec scales relevant to the galaxy. For instance, supernovae, in the presence of magnetic fields and cosmic rays, have been shown to launch sustained galactic outflows from the disc that extend hundreds of kiloparsec from the its mid-plane (Kjellgren et al., 2025). Within the disc, supernovae are known to punch low-density holes known as bubbles in the ISM, seen both in simulations (Khullar et al., 2024) and resolved in observations of nearby galaxies (e.g. Thilker et al., 2023).

Star formation is correlated with the dense gas content of a galaxy. A power-law relation between the surface density of star formation ($\Sigma_{\rm SFR}$) and the gas surface densities (Σ) was suggested as far back as 1950s (Schmidt, 1959). This was later observationally tested on external galaxies and improved at the turn of the century by Kennicutt (1989, 1998). Such empirical laws, that relate the surface densities of

SFR of galaxies with the gas content came to be known as the Kennicutt-Schmidt relations in their honour. This relation of remarkable simplicity, has been shown to be valid across varying environments and spatial scales. This is demonstrated in Figure 2, that shows the $\Sigma_{\rm SFR}$ against the gas surface densities normalised by the local free-fall times $t_{\rm ff} = \sqrt{3\pi/32G\rho}$, taken from Krumholz (2014). The data includes environments ranging from resolved regions within the Milky Way, local galaxies, to unresolved galaxies (including starbursts) that are treated as point objects both at $z = 0$ and $z > 0$. The black straight line is a fit of the form

$$\Sigma_{\rm SFR} = \epsilon_{\rm ff} \frac{\Sigma_{\rm H_2}}{t_{\rm ff}}, \tag{1}$$

where $\epsilon_{\rm ff}$, is the star formation efficiency per free-fall time, and is $= 0.01$ for the fit. This low value of $\epsilon_{\rm ff}$ has put forth star formation as an inefficient process. Where magnetic fields, turbulent flows (Krumholz and McKee, 2005; Padoan and Nordlund, 2011; Hennebelle and Chabrier, 2011; Federrath and Klessen, 2012), and various feedback processes (Thompson et al., 2005; Ostriker and Shetty, 2011) from formed stars in the ISM prevent the gas from collapsing within a free-fall time, acting as regulation mechanisms.

Even though Figure 2 suggests a universal scaling independent of the galactic environment, recent observations of nearby galaxies have shown indications of variations in the $\epsilon_{\rm ff}$ between the centre and the outskirts (e.g. Sun et al., 2023; Pessa et al., 2022). This suggests that star formation might not be entirely decoupled from its nascent galaxy. Moreover, the dense molecular gas must originate from the diffuse gas in the galaxy in the first place. The following sections explore observations that suggest this, and how this could be achieved.

1.3 Dense gas in galaxies

The cold dense gas in galaxies, in the form of neutral HI and molecular H_2, constitute the major mass budget of the ISM ($\geq 50\%$), while only occupying a fraction of its volume ($\leq 10\%$). Together, these gaseous phases thus decide the initial conditions of the gas that will form stars which makes them important constituents of interest in the study of galaxy evolution.

How is this dense gas organised in galaxies? Given the high mass and corresponding low volume fractions, one can see that the cold HI and H_2 are both likely present in dense agglomerations. These are referred to as HI clouds (Elmegreen and Elmegreen, 1987) and giant molecular clouds respectively (see Chevance et al., 2023, for a recent review). The later have been suggested to be enveloped within larger HI superclouds. Getting a statistical view on their galaxy-wide organisation and morphology has been more challenging. Our biased position within the galactic disc has line-of-sight effects, while observations of external galaxies have suffered from limited resolutions. Recent advancements in observational facilities, though, are allowing us to view this organisation in more detail. Taking CO observation in the mm range as an example, their spatial resolutions in nearby galaxies have improved from ~ 1 kpc (e.g. Leroy et al., 2009) to ~ 100 pc (Leroy et al., 2021) in around a decade.

The information on the organisation of dense gas on galactic scales, its regularity or lack thereof, can inform us about the relative relevance of various processes in determining gas flows. The next two subsections will elucidate this organisation, as seen in observations.

1.3.1 Spiral arms: Beads on a string

"Bright stars, strung out like pearls along the arms. "

Baade (1963)

While the origin of spiral arms in galaxies still remain debated (see review by Dobbs and Baba, 2014), it is clear that gaseous spirals contain most of the dense gas content and massive star forming (HII) regions in a spiral galaxy. The HII regions, along with young stellar clusters are found to be spaced at irregular intervals along the spiral arms. In a HST survey of 200 nearby star forming galaxies, around 10% have been shown to have clouds spaced at regular distances (Elmegreen and Elmegreen, 1983). These are referred to as "beads on a string" pattern. Hints of such spatial regularity were already observed decades ago in our own galaxy, where HI clouds were found to be strung regularly along one of Milky Way's arms (McGee and Milton, 1964; Elmegreen and Elmegreen, 1987). This was later found to be the case for the Cygnus and Carina arms of the Milky Way (Efremov, 2009) and one of the arms of M31 as well (Efremov, 2010).

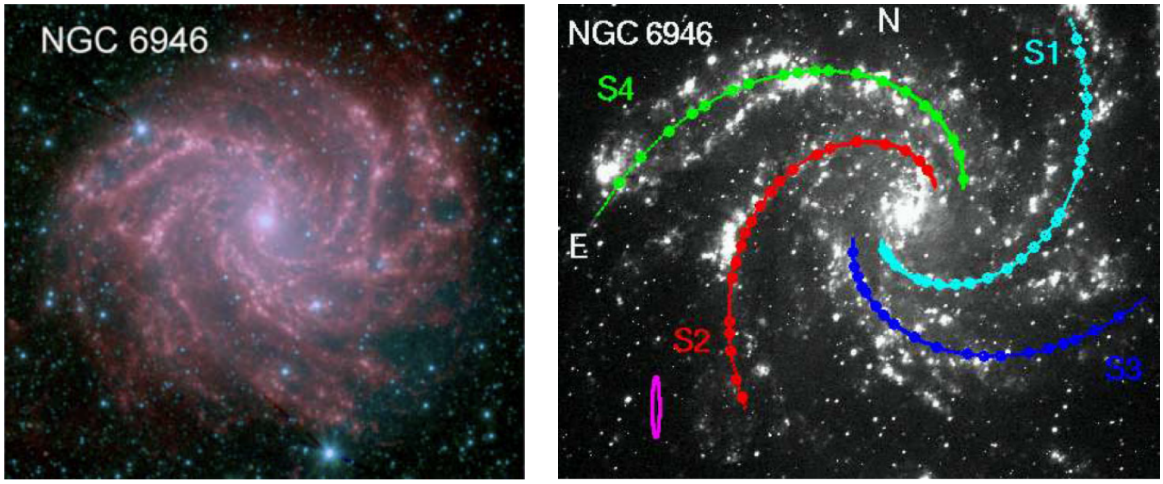

Figure 3: Beads on a string pattern seen along multiple spiral arms of the flocculent spiral galaxy NGC 6946 at two different wavelengths. Left panel shows the IR composite that consists of 3.6 μm (blue), 4.5 μm (green) and 8 μm (red), taken from Elmegreen and Elmegreen (2019). Right panel is the same galaxy in Hα from Gusev et al. (2022), with overlaid lines tracing different spiral arms that are strung with beads representing peaks in Hα luminosity.

In observations of external galaxies, these regularities have been argued to be obscured due to extinction in optical wavelengths and young stellar feedback destroying any evidence of their natal clouds (thus the low 10% detection rates). Taking advantage of the IR observations from Spitzer proved fruitful, for it revealed IR cores extincted in optical, dotting most spiral features in the sample of 22 spiral galaxies observed (Elmegreen et al., 2006, 2014, 2018; Elmegreen and Elmegreen, 2019). These included flocculent, multiple and grand design spiral galaxies. Moreover, they had signs of embedded star formation, which is a short and early phase of the process - recent

estimates from nearby galaxies predict this phase to last 2–7 Myrs (Kim et al., 2021). The short timescales indicate that there is a connection between the formation of these beads and the initiation of star formation within them.
Figure 3 shows the mosaic of one such studied galaxy - NGC 6946 in two different bands. Taken from Elmegreen and Elmegreen (2019), the left panel shows the galaxy in a composite of three infrared bands; 3.6 μm (blue), 4.5 μm (green) and 8 μm (red). The right panel shows the same in Hα, which is taken from Gusev et al. (2022). We can see that there are regular concentration of emission along the spiral features in both the panels. The right panel highlights this further, with analytical fits tracing the spiral arms, where the beads represent peaks in Hα luminosity. Using this fitting technique on a sample of four spiral galaxies - NGC 628, NGC 895, NGC 5474 and NGC 6946, Gusev et al. (2022) concluded that the adjacent separations of these star forming regions were in the range 350–500 pc and integer multiples of this. This range also agrees with the spacing of IR cores in spiral galaxies (Elmegreen et al., 2018), and even that of young stellar groupings, star formation regions along rings in galaxies (Gusev and Shimanovskaya, 2020; Proshina et al., 2022).
This semi-regularity of IR cores with signs of embedded star formation, massive star forming regions and young stellar clusters along the length of spirals and rings in nearby galaxies hint at an evolutionary sequence of events. One that could be initiated via galactic instability that creates dense structures on a preferred length-scale. We explore this possibility further in Section 1.4.2.

1.3.2 Feathers

> "The limits of my language are the limits of my mind."
>
> Ludwig Wittgenstein

Spiral patterns were known to humans long before they were seen in galaxies. Thus, one could imagine that when William Parsons viewed M51 in 1845, it was straightforward for him to describe it as a spiral nebula (Rosse, 1850; Bailey et al., 2005). Further categorisation of spiral features, however, required more creativity. The term "Feathers" was coined by Lynds (1970) to attribute the thin dust lanes that were seen protruding regularly from the inner edges of the main bulky spiral arms of a few nearby spiral galaxies. A striking feature of feathers, was that they were seen cutting across multiple spiral arms - displaying coherency on kiloparsec scales. Feathers, were also seen to be associated with another regular spiral feature, comprising of OB associations and HII regions, called "spurs"[2] (Weaver, 1970; Elmegreen, 1980). Similar to feathers, spurs were seen jutting out from the spiral arms. However, in contrast to kpc-scale feathers that displayed varying pitch angles, spurs were uniformly perpendicular to the arms and were much shorter compared to the feathers. The relation between spurs and feathers remain debated.
In the last decade, elongated ($\geq$ 100 pc), filamentary and dense features that thread the mid-plane and are connected to spiral arms have also been found in our own

[2]The author found the following general definition of the word **Spur**: A device for pricking the side of a horse in order to urge it forward, consisting of a small spike or spiked wheel attached to the rider's heel. Oxford University Press. (n.d.). "Spur" Oxford English Dictionary. Retrieved February 11, 2025, from https://www.oed.com

galaxy (Goodman et al., 2014; Ragan et al., 2014; Zucker et al., 2015; Veena et al., 2021). These are dubbed as the "bones" of the underlying skeleton of the Milky Way. However, our position inside the mid-plane of the disc makes them harder to catalogue. Nearby face-on external galaxies make ideal candidates for a statistical view of such structures due to the birds-eye-view granted by them.

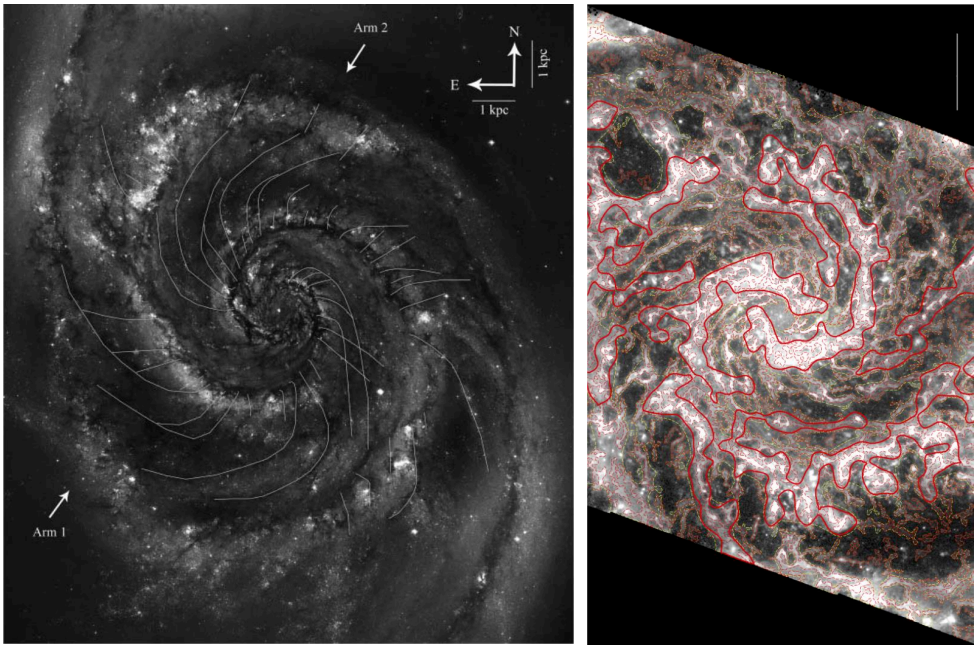

Figure 4: Feathers, as seen in two nearby spiral galaxies. Left panel shows NGC 5194 in optical, overlaid with feathers in white, taken from La Vigne et al. (2006). The right panel is NGC 628 in the 7.7 μm band from Thilker et al. (2023), with feathers highlighted in dashed and solid contours using 25 pc and 200 pc filament masks.

The first detailed survey that catalogued feathers in external galaxies was performed using the HST archival data, where feathers were seen as optically attenuated dark features (La Vigne et al., 2006). The authors found an occurrence rate of 20% across all spiral galaxies and of around 83% in galaxies with well-defined spiral arms (Sb-Sc galaxies). Later, they were also seen as emission features in the infrared band with Spitzer (Elmegreen et al., 2006, 2014, 2018; Elmegreen and Elmegreen, 2019). Fresh high-resolution infrared data from the JWST/MIRI of nearby galaxies (Williams et al., 2022; Thilker et al., 2023; Meidt et al., 2023) has revealed them in unprecedented detail. We show the feathers in optical and infrared bands for two galaxies in Figure 4. The left panel shows HST observation of NGC 5194 from La Vigne et al. (2006), with the optically extincted feathers hand-drawn and highlighted in white. The right panel shows NGC 628 in the 7.7 μm band of the JWST/MIRI from Thilker et al. (2023), where feathers are marked in contours with a filament identification algorithm. We can see that in both the cases, feathers are kpc-scale regular lattice features that thread the galaxy. Both the attenuation of optical light and the emission in mid-infrared band ($\approx 5 - 40$ μm) point towards the presence of dust in feathers. Microphysical modelling of dust emission has demonstrated that the emission in mid-infrared is likely dominated by PAHs (Lai et al., 2020). Moreover, feathers have been found recently to host HII regions and numerous embedded young stellar clusters within them (Schinnerer et al., 2017; Thilker et al., 2023). Their ubiquity in spiral galaxies,

regularity on kpc-scales, and evidence of hosting star forming regions makes them an ideal candidate to probe the effects of galactic dynamics on the initial conditions of star formation.
We still lack a resolution on the understanding of their origin. Multiple mechanisms have been proposed to bring about their existence. Kiloparsec scale magnetic fields that destabilise the disc on a preferred length-scale (Körtgen et al., 2019), clustered supernovae that drive gas flows from the spiral arms into the inter arm regions at a regular spacing (Kim et al., 2020), or instabilities within the gaseous spiral arms that fragment into over-dense regions and get sheared into the interarm region (e.g. Mandowara et al., 2022). Some works have also suggested that result from a global gravitational instability in action (Griv and Gedalin, 2012; Meidt et al., 2023). These mechanisms are further discussed in the next section.

1.4 Disc instabilities

The semi-regularity exhibited by the dense gas within the spiral arms and in the inter-arm regions suggests that galactic instabilities might be responsible for their origin. An instability, generally refers to the tendency of a system to deviate from equilibrium configurations into run-away growth.
To a good approximation, we can physically define the ISM as a non-relativistic, compressible, ideal magnetised fluid. That is, an inviscid, neutral fluid consisting of charged (electrons and ions) and neutral species that are coupled together due to frequent collisions. We can do this because the typical length scales ($\sim$ pc) and time scales ($\sim$ Myr) under our consideration are much larger than the mean free path of the particles, and the Debye length and the inverse of the plasma frequency respectively (Shukurov and Subramanian, 2021). Under these conditions, the equations of the ISM-fluid may be written as (see Choudhuri, 1998, for detailed derivation)

$$\frac{\partial \rho}{\partial t} + \nabla.(\rho\vec{v}) = 0, \tag{2}$$

$$\frac{\partial(\rho\vec{v})}{\partial t} + \vec{\nabla}.(\rho\vec{v}\vec{v}) = -\vec{\nabla}P - \rho\vec{\nabla}(\Phi_{\rm g} + \Phi_{\rm ext}) + \frac{1}{4\pi}(\vec{\nabla}\times\vec{B})\times\vec{B}, \tag{3}$$

$$\frac{\partial \vec{B}}{\partial t} = \vec{\nabla}\times\left(\vec{v}\times\vec{B}\right), \tag{4}$$

$$P = P(\rho), \tag{5}$$

$$\nabla^2\Phi_{\rm g} = 4\pi G\rho, \tag{6}$$

$$\vec{\nabla}.\vec{B} = 0. \tag{7}$$

where ρ is the density, $\vec{v}$ is the velocity, P is the pressure, $\Phi_{\rm g}$ is the gravitational potential of gas self-gravity and $\Phi_{\rm ext}$ is the total potential of the dark matter, old stars or other components such as the bulge, bar or the spiral and $\vec{B}$ is the magnetic field. The following sections will outline various kinds of instabilities that result from linear perturbation analysis of these equations under various approximations.

1.4.1 Safranov-Toomre instability

Most over-densities in the universe arise from the long-range attractive force of gravitation. Here, we use linear stability analysis to examine its role in case of razor-thin

gaseous discs. Originally performed independently by Safronov (1960) and Toomre (1964).
The density of an infinitesimally-thin, uniform disc can be written as

$$\rho(R, z) = \Sigma_0 \delta(z), \tag{8}$$

where Σ_0 is the uniform surface density of the disc and $\delta(z)$ is the dirac-delta function that peaks at $z = 0$ and R is the cylindrical radius. In equilibrium, we expect the disc to be circularly rotating about the centre. Thus, the gas velocity may be written as

$$\vec{v_0} = R\Omega(R)\,\hat{\theta}, \tag{9}$$

where $\Omega(R)$ is the radially dependent angular velocity and $\hat{\theta}$ is the unit vector in the azimuthal direction. Now, considering the gas in the galaxy to be an unmagnetised, isothermal fluid, the equation set 2 - 7 become

$$\frac{\partial \rho}{\partial t} + \vec{\nabla}.(\rho \vec{v}) = 0, \tag{10}$$

$$\frac{\partial(\vec{v})}{\partial t} + (\vec{v}.\nabla).\vec{v} = -\frac{\vec{\nabla} P}{\rho} - \vec{\nabla}(\Phi_{\rm g} + \Phi_{\rm ext}), \tag{11}$$

$$\nabla^2 \Phi_{\rm g} = 4\pi G \rho, \tag{12}$$

$$P = \rho c_{\rm s}^2, \tag{13}$$

where $c_{\rm s}$ is the uniform sound speed of the medium and other symbols have their usual meanings. For the equilibrium configuration of the disc, we use the steady-state condition $\partial/\partial t = 0$, and plugging-in the circular velocity (Eq. 9) in Eq. 11, we have

$$R\Omega^2 = \vec{\nabla}_R(\Phi_{\rm g0} + \Phi_{\rm ext}) = \vec{\nabla}_R(\Phi_0), \tag{14}$$

where the $\vec{\nabla}_R = \hat{R}.\vec{\nabla}$ is the radial gradient of the potential. Thus, the gravitational potential of the gas + stars+ dark matter together provide the force for the centripetal acceleration of the gas rotating around the centre.
Now that the initial state of our disc is determined, we perturb the quantities to study its deviation from equilibrium. We assume axisymmetric perturbations ($\partial/\partial\theta = 0$) in the plane of the disc. Let the perturbed density, velocity and gas gravitational potential be

$$\rho_1 = \Sigma_1(R)\delta(z), \tag{15}$$

$$\vec{v_1} = v_R \hat{R} + v_\theta \hat{\theta}, \tag{16}$$

$$\Phi_{g1} = \Phi_1, \tag{17}$$

$$\tag{18}$$

respectively. The evolution of these perturbed quantities is still determined by the Equations 10 - 13. Thus, plugging in these quantities, we have

$$\frac{\partial \Sigma_1}{\partial t} + \vec{\nabla}.\left[(\Sigma_0 + \Sigma_1)(\vec{v}_0 + \vec{v}_1)\right] = 0 \qquad \text{, using } \tfrac{\partial \Sigma_0}{\partial t} = 0, \tag{19}$$

$$\frac{\partial \Sigma_1}{\partial t} + \vec{\nabla}.\left[\Sigma_0(\vec{v}_0 + \vec{v}_1) + \Sigma_1 \vec{v}_0\right] = 0 \qquad \text{, neglecting } \Sigma_1 \vec{v}_1, \tag{20}$$

$$\frac{\partial \Sigma_1}{\partial t} + \vec{\nabla}.\left[\Sigma_0 \vec{v}_1\right] = 0 \qquad \text{, axisymmetry } \partial/\partial\theta = 0, \tag{21}$$

$$\frac{\partial \Sigma_1}{\partial t} + \Sigma_0 \left[\frac{v_R}{R} + \frac{\partial v_R}{\partial R}\right] = 0. \tag{22}$$

Doing the same for the radial component of the Euler equation, where we neglect all 2nd order terms and using the condition of axisymmetry, we have

$$\frac{\partial v_R}{\partial t} + v_R \frac{\partial v_R}{\partial R} - \frac{(R\Omega + v_\theta)^2}{R} = -\frac{1}{\Sigma_0 \delta(z)} \frac{\partial P}{\partial R} + \hat{R}.\vec{\nabla}(\Phi_0 + \Phi_1), \tag{23}$$

$$\frac{\partial v_R}{\partial t} - \Omega^2 R - 2\Omega v_\theta = -\frac{1}{\Sigma_0 \delta(z)} \frac{\partial P}{\partial R} + \hat{R}.\vec{\nabla}(\Phi_0 + \Phi_1), \text{neglecting } \mathcal{O}(2) \text{ terms}, \tag{24}$$

$$\frac{\partial v_R}{\partial t} - 2\Omega v_\theta = -\frac{c_s^2}{\Sigma_0} \frac{\partial \Sigma_1}{\partial R} - \hat{R}\vec{\nabla}(\Phi_1) \qquad \text{, using } Eq \text{ 13, 14.} \tag{25}$$

Similar steps with the azimuthal component gives

$$\frac{\partial v_\theta}{\partial t} + v_R \left[\Omega + \frac{\partial (R\Omega)}{\partial R}\right] = 0. \tag{26}$$

The first order Poisson equation, thus becomes,

$$\nabla^2(\Phi_1) = 4\pi G \delta(z) \Sigma_1. \tag{27}$$

Using the axisymmetric ansatz $\propto f(z) \exp i(kR + \omega t)$ for all first order terms of the perturbed quantities, the equations of motion become

$$i\omega \Sigma_1^* + \Sigma_0 \left[\frac{v_R^*}{R} + ikv_R^*\right] = 0, \tag{28}$$

$$i\omega v_R^* - 2v_\theta^* \Omega = -\frac{c_s^2}{\Sigma_0}(ik\Sigma_1^*) - ik\Phi_1^*, \tag{29}$$

$$i\omega v_\theta^* + v_R^* \left[\Omega + \frac{\partial (R\Omega)}{\partial R}\right] = 0, \tag{30}$$

$$\frac{d^2\Phi_1^*}{dz^2} + \frac{k\Phi_1^*}{R}\left[i - kR\right] = 4\pi G \Sigma_1^* \delta(z), \tag{31}$$

where the starred variables are the respective functions of the ansatz. First, we solve for the Φ_1^* under the assumption that $kR \gg 1$, also known as the short-wavelength assumption. Physically, this means that we look at perturbations $\ll$ than the spatial scale of the disc. This is a realistic assumption since any perturbers in real discs will likely be of the order of the scale height of the disc, which is negligible compared to the radial lengths for thin-discs considered here. This allows us to simplify Eq. 31 to

$$\frac{d^2\Phi_1^*}{dz^2} = k^2 \Phi_1^* + 4\pi G \Sigma_1^* \delta(z). \tag{32}$$

Assuming solutions of the form $A\exp(-|kz|)$, which is inspired from vanishing solutions in the absence of the gravitating term. We can determine the A by integrating the equation from $z=-\epsilon$ to $z=+\epsilon$, where ϵ is vanishingly small. This takes out the term $k^2\Phi_1^*$ because it is a continuous function. Leaving

$$\left.\frac{d\Phi_1^*}{dz}\right|_{-\epsilon}^{+\epsilon} = 4\pi G\Sigma_1^*, \tag{33}$$

$$A = \frac{-2\pi G\Sigma_1^*}{|k|}. \tag{34}$$

Thus, the perturbed gravitational potential at the mid-plane is $-2\pi G\Sigma_1^*/|k|$. Now, we use all the equations to get $\omega(k)$ only in terms of the initial state of the disc defined by the free parameters $\{\Sigma, \Omega, c_\mathrm{s}\}$. For this, we use Eq. 30, Eq. 34 and substitute them in Eq. 29, this gives us

$$v_R^*\left(\omega - \frac{2\Omega}{\omega}\left[\Omega + \frac{\partial(R\Omega)}{\partial R}\right]\right) = \Sigma_1^*\left(-\frac{c_\mathrm{s}^2 k}{\Sigma_0} + \frac{2\pi G k}{|k|}\right) \tag{35}$$

finally, we also substitute for Σ_1^* under the approximation $kR \gg 1$ Eq. 28 reduces to $\Sigma_1^* = -k\Sigma_0 v_R^*/\omega$, which gives

$$\omega^2 - 2\Omega\left[\Omega + \frac{\partial(R\Omega)}{\partial R}\right] = -k\left(-c_\mathrm{s}^2 k + \frac{2\pi G\Sigma_0 k}{|k|}\right), \tag{36}$$

$$\omega^2 = k^2 c_\mathrm{s}^2 - 2\pi G\Sigma_0|k| + \kappa^2, \tag{37}$$

where $\kappa^2 = 2\Omega\left[\Omega + \partial(R\Omega)/\partial R\right]$ is the epicyclic frequency. This is the frequency of oscillations of a test mass in a circular orbit under the influence of an axisymmetric potential (Binney and Tremaine, 1987). For instance, a star in a galaxy. Eq. 37 is the dispersion relation, which gives ω as an explicit function of k. According to our ansatz, with physical quantities $\propto \exp i(kR + \omega t)$, we see that negative values of ω^2 will give us exponentially growing solutions. One can use this to determine the role played by quantities on the RHS of the dispersion relation. The positive terms - the pressure ($k^2c_\mathrm{s}^2$) and rotation (κ^2), act as stabilising agents, while the negative gravitational term ($-2\pi G\Sigma_0|k|$) act to destabilise the disc. Large spatial scales (low k) are stabilised by rotation while small spatial scales (large k) are stabilised by thermal pressure. Thus, an intermediate range of scales may be gravitationally unstable, that can quantified by requiring $\omega^2 < 0$. Since $\omega^2(k)$ is a concave-up quadratic function, it will suffice to require that its minima is ≤ 0, which gives

$$\kappa^2 - \left(\frac{\pi G\Sigma_0}{c_\mathrm{s}}\right)^2 \leq 0, \tag{38}$$

$$Q \leq 1, \tag{39}$$

where $Q = \kappa c_\mathrm{s}/\pi G\Sigma$ is a dimensionless parameter often referred to as the Toomre-Q. Thus, the instability criteria of an axisymmetric, razor-thin disc is quantified by a single dimensionless parameter. In deriving this, however, we have neglected various other components and physical processes present in real galaxies. These include the

effect of stars, dark matter particles, magnetic fields, spiral arms and cooling/heating, turbulent nature of the ISM etc.
Many of the aforementioned assumptions have been relaxed in works following the seminal work of Safronov (1960) and Toomre (1964). The effect of the gravitational component of background stars was included by Jog and Solomon (1984), who proposed the two-component Toomre-Q. Stars were shown to destabilise due to their gravity, while their random motions stabilised against this. The two-component Toomre-Q was later improved and simplified in many subsequent works (Elmegreen, 1995; Jog, 1996; Wang and Silk, 1994; Romeo and Wiegert, 2011). Effects of gas dissipation, which uses a time-dependent energy equation instead of a polytrope equation of state, was taken into account by Elmegreen (2011). Effects of disc thickness by Shu (1968); Vandervoort (1970) among others, and non-axisymmetry was explored in Griv and Gedalin (2012) and vertical (z) perturbations were studied recently in Meidt and van der Wel (2024). Relaxing the assumptions of axisymmetry and the inclusion of vertical perturbations lifted the condition for Q threshold for disc instabilities.
Rotation can also work together with self-gravity, instead of against it as in the case of the Toomre-instability, to give rise to disc instabilities. The mechanism by which self-gravity acts together with shear and epicyclic motions is termed the "swing-amplification" (Goldreich and Lynden-Bell, 1965; Julian and Toomre, 1966; Fuchs, 2001; Binney, 2020; Meidt and van der Wel, 2024). This is usually explained using shearing wavefront analysis, where shearing waves that go from leading to trailing configurations get amplified due to the action of self-gravity. This happens because the epicyclic motions also sweep in the same direction, thus, trapping the wave crests in regions of excess density and increasing the effect of self-gravity (Kim and Ostriker, 2001).
Observations reveal that most nearby star-forming disc galaxies have the two-component Q parameter (gas+stars) around 1–2 (Leroy et al., 2008, and references therein). This low spread in the Q suggests that the disc maintains marginal stability via some galactic regulation. We note that there are systematic uncertainties to these observational measurements - major ones arising from the estimates of velocity dispersion of gas, stars and the mass-to-light ratios used to estimate stellar surface densities.

1.4.2 Spiral arm instability

The theoretical plausibility of the existence of gaseous spiral arms was established in the 1960s. Where, modelling the gravitational potential of spiral stellar-overdensities via an analytical spiral potential, Fujimoto (1966) and Roberts (1969) showed that the gas in a galaxy will naturally develop galactic-scale gaseous spiral shocks in response to the spiral potential. Such shocks were later proposed to trigger star formation in the high-density spiral-shaped wakes (Roberts, 1970). The analytical form of the spiral potential used in these studies (and later on) is given by

$$\phi(R,\theta,t) = \phi_0(R,\theta)\cos\left(m\left(\theta - \Omega_{\rm p}t - \frac{1}{\tan i}\ln\left[\frac{R}{R_0}\right]\right)\right), \tag{40}$$

where $\phi_0(R,\theta)$ is a slowly-varying function of (R,θ), m is the number of spiral arms, $\Omega_{\rm p}$ is the angular speed of the potential, $\tan i$ is the pitch angle of the spiral and R_0 is a normalisation radius. We can visualise the spiral shape of the potential by looking at its equipotential surfaces. Plugging-in $\Omega_{\rm p} = 0$ and $m = 1$ for a one-armed

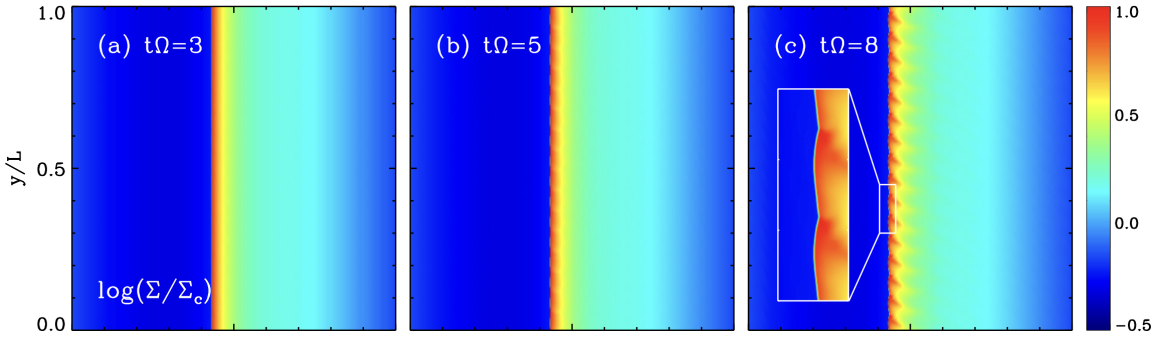

Figure 5: The development of the spiral arm instability on a spiral shock front. The three panels show time snapshots (increasing from left to right) of local boxes in the spiral arm coordinates: y is along the arm and x perpendicular to it. Taken from Kim et al. (2014).

stationary spiral, the cosine argument becomes

$$\eta = \theta - \frac{1}{\tan i}\ln(R/R_0) \qquad or, \tag{41}$$

$$R = R_0 e^{(\theta-\eta)\tan i}. \tag{42}$$

Given that $\phi_0(R,\theta)$ is a slowly varying function, $\eta =$ const gives us equipotential curves. Looking at Eq. 42, these are nothing other than a family of logarithmic spirals shifted by a constant phase η.

Very first numerical simulations, employing similar forms of the spiral potential as an external potential (see Eq. 3), found that the spiral arms themselves showed development of overdensities along them rather than in their wakes (Johns and Nelson, 1986). With higher resolution, the spiral arms were observed to be unstable to exponential growth via hydrodynamical instabilities (Kim and Ostriker, 2002; Chakrabarti et al., 2003; Wada and Koda, 2004). Their results were confirmed by subsequent linear stability analysis and high resolution two-dimensional (2D) simulations of local curvilinear spiral shaped boxes (Kim and Ostriker, 2006a; Lee and Shu, 2012; Kim et al., 2014; Lee, 2014; Kim et al., 2015). An example of such a simulation is shown in Figure 5, where a 2D box in the plane of the disc is simulated with (x, y) representing coordinates perpendicular and parallel to the spiral arm respectively. The spiral arm shock that runs through the middle of the domain can be seen getting unstable with time as we go from the left panel to the right, in around $t = 8\,\Omega^{-1} = 1.27\,t_{\rm rot}$ to regularly spaced "wiggles". Their spacing, representing the fastest growing mode of the instability.

Although its existence has been established by many independent works, the fundamental cause and nature of the spiral instability remained debated for more than a decade. For some, magnetic fields were the major perpetrators (Kim and Ostriker, 2006a; Lee and Shu, 2012), for others it was the familiar Kelvin-Helmholtz Instability (KHI) in action (Wada and Koda, 2004) or a new kind of hydrodynamical instability named as the Wiggle instability (Kim et al., 2014), for others that remained unconvinced it was an artifact of numerical noise (Hanawa and Kikuchi, 2012). Its nature was only recently shown to be a combination of KHI and a vorticity generating instability due to repeated passages of gas through the spiral shock (Mandowara

et al., 2022). Moreover, it was found to be highly non-linear and deviated from the expectations of linear analysis (Mandowara et al., 2022).
The effects of pervasive magnetic fields on the instability have been studied in many works, all reporting a stabilising effect to varying degrees. Shetty and Ostriker (2006) reported complete suppression of the hydrodynamical instability in the presence of B-fields, while Kim and Ostriker (2006b) simulations showed that spiral arms are still unstable in the presence of magnetic fields, but stabilise the vorticity generating hydrodynamical instability. In later studies, it was agreed by two independent works that magnetic fields stabilise the hydrodynamical instability by smoothing out the shocks. Kim et al. (2015) found a decrease in growth rate of the instability by a factor of four, however Lee (2014) reported only a small decrease in the growth rates. Most of these studies, however, were either local, or 2D. While these approximations can be necessary and useful for studying a phenomena in isolation, they fail to capture the effects of magnetic fields, that are 3D in nature. For instance, in-plane magnetic fields are known to destabilise the stratified medium of a galaxy (Parker, 1966). It is yet to be seen, what are the effects of B-fields in a 3D global setting. One, where the effects of magnetic fields both in the plane of the disc and perpendicular to it work in tandem (see Section 1.4.3 for details).
The spiral arm instability has been held responsible for various observed features associated with the spiral arms and the interarm regions in nearby spiral galaxies. These include the regular beads-on-a-string star forming regions and the spurs that jut out from the spiral arms (c.f. Section 1.3.1), as well as the dense feathers/filaments that extend from one arm to the other (Section 1.3.2).

1.4.3 Magnetic instabilities

> *"The magnetic field exists in the universe as an 'organism', feeding on the general energy flow of stars and galaxies."*
>
> - E. N. Parker (1979)

Magnetic fields, at a first glance, are expected to act as stabilising agents against instabilities due to the added magnetic pressure term (see Eq 3). It was Parker (1966), who first demonstrated that they instead destabilise the galactic disc, acting as a viable mechanism for molecular cloud formation. This unexpected behaviour was a consequence of an interplay between the stratified geometry of galactic disc, the anisotropy of magnetic pressure and flux-freezing of magnetic fields in the ISM.
Parker (1966) originally considered a local-patch of the stratified medium of a galaxy, neglecting the effects of rotation. He assumed large-scale uniform magnetic fields threading through the mid-plane of the galaxy, which in hindsight is a good approximation since kiloparsec-scale azimuthal magnetic fields have been observed in nearby galaxies in equipartition with a small-scale turbulent field (Beck et al., 2020). The local magnetised patch was assumed to sit in a background potential of stars and dark matter that provided a constant acceleration towards the mid-plane.
Considering a flux tube aligned with the frozen-in magnetic fields in the mid-plane of the disc, we will argue for its instability without the rigorous stability analysis as done by Parker. Due to random velocity fluctuations in the vertical direction,

a section of the flux tube may be displaced out of the mid-plane. Once displaced, the flux tube which is now a bump rising from the mid-plane, will rise further up rather than settling down. Thus exhibiting an instability. To see this, consider the gas in the bump of the flux tube that has risen. This gas will flow down to the mid-plane due to the gravitational pull of the disc. However, instead of flowing vertically downwards and ceasing to be the bump, as it would have done in the absence of magnetic fields. The gas instead, drains along the magnetic fields lines (due to flux-freezing) through the sloping flux-tube that connects the bump to the mid-plane of the disc. This draining of gas makes the bump lighter and more buoyant, and it is pushed further upwards due to the pressure difference, becoming unstable. The instability eventually saturates once the bump has risen into a steep hill. This is due to the magnetic tension in the bent magnetic field lines that opposes the pressure gradient responsible for accelerating the gas parcel. This instability creates a hills and valley morphology of gas in the vertical plane of the galaxy. One where the drained gas from the hills has accumulated in valleys to form dense condensations of molecular clouds. We have to be careful in extending this analogy though, since this might only be valid for the initial, linear stages of the instability.
The instability criteria for the same is given by (Mouschovias, 1996)

$$\lambda_y > \Lambda_y = 4\pi H \left(\frac{1}{1+2/\beta}\right)^{1/2}, \tag{43}$$

$$\lambda_z > \Lambda_z(\lambda_y) = \Lambda_y \left[1 - \left(\frac{\Lambda_y}{\lambda_y}\right)^2\right]^{-1/2} > \lambda_y. \tag{44}$$

Here, λ_y is the physical length scale in the plane of galaxy along the magnetic field lines and λ_z is the same in the vertical direction. We can see that there is a minimum length-scale, both in the plane of the galaxy and perpendicular to it, above which the instability is active. Physically, this can be thought of as a condition set by magnetic tension, where steeper hills (with $\lambda_y \ll \lambda_z$) will oppose the rise of the flux-tube due to higher magnetic tension. Although the dispersion relation is a fourth-order polynomial (see Eq. 17 in Mouschovias, 1996), the growth rate of the fastest growing mode is well approximated by

$$\omega_{\rm Parker} \sim \frac{v_{\rm a}}{H}, \tag{45}$$

where $v_{\rm a} = B/\sqrt{4\pi\rho}$ is the Alfvén speed and H is the scale-height of the galaxy. The maximum growth rate is achieved for $\lambda_z \to \infty$ and an intermediate value of λ_y which is a few times the disc scale-height.
The linear analysis of the instability have been furthered explored in many works. This includes the development of equilibrium states (Mouschovias, 1974), effects of differential rotation (Foglizzo and Tagger, 1994) and cosmic-ray diffusion (Kuznetsov and Ptuskin, 1983). Differential rotation has been showed to have a stabilising effect, while cosmic-ray anisotropic diffusion further enhances the instability due to their added pressure component and preferential diffusion along the magnetic field lines (Rodrigues et al., 2016, and references therein).
The non-linear states of the instability have been explored in numerical simulations (Basu et al., 1997; Kim et al., 2002; Rodrigues et al., 2016; Tharakkal et al., 2023a,b).

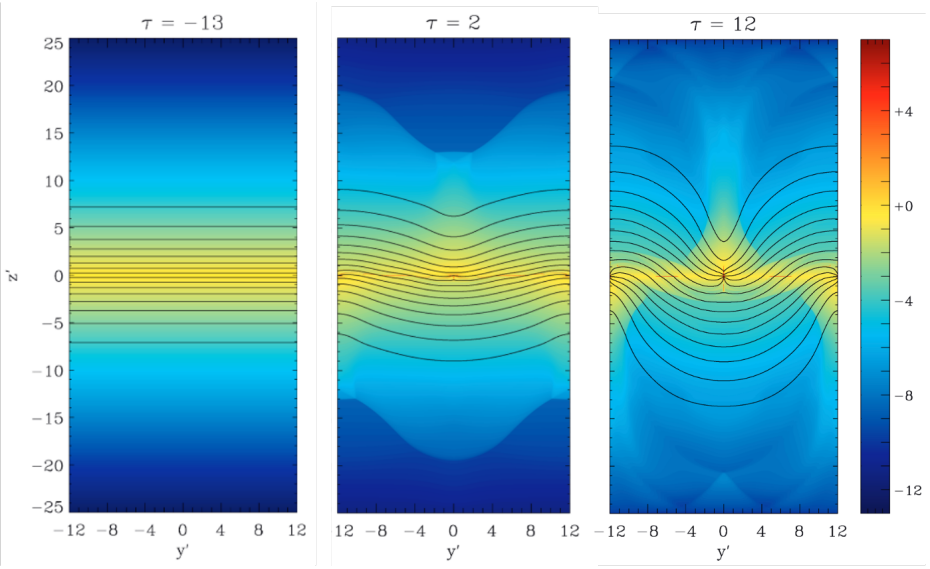

Figure 6: Development of the Parker instability in a controlled idealised numerical experiment. Each panel shows the dimensionless density of the gas, overlaid by the magnetic field lines. The progression from left to right exhibits the gradual formation of Parker hills, as the initial gas stratification is destabilised and deformed. Taken from Mouschovias et al. (2009).

In Figure 6, we show snapshots from one such numerical simulation taken from Mouschovias et al. (2009), that aimed to capture the Parker instability in a controlled numerical experiment. The three panels show the time evolution (from left to right) of the dimensionless density of the gas $\rho/\rho_{\rm ref}$, where $\rho_{\rm ref}$ is a reference density. The magnetic field lines, initially parallel to the plane of the disc (y' direction), are overlaid in black. The coordinates are normalised by the thermal scale height of the box, $c_{\rm s}^2/g = 35.45$ pc, and the time by the scale height sound crossing time $c_{\rm s}/g = 6.05$ Myr. We can see that the equilibrium stratified configuration of the first panel is progressively deformed into the magnetic hills and valley structure as we proceed towards the right. The non-linear phase of the instability is exhibited by the middle to right panel. We can see that within a time period of ~ 60 Myr, magnetic hills of height 10 times the scale height rise above and below the mid-plane, giving rise to accumulation of dense gas in the valleys.

Observational evidence for the Parker instability is sparse. Edge-on synchrotron mock observations have been shown to be dominated by the disc component (Rodrigues et al., 2016), with negligible variation in the presence of the instability. While Faraday rotation maps of simulated face-on galaxies have shown promise (Heintz et al., 2020), these have not been tested in observations. Still, rotation measure maps of a spiral arm of the face-on galaxy NGC 628, has displayed signs of magnetic Parker loops (Mulcahy et al., 2017) that are roughly coincident with the regularly spaced star-forming regions found along the length of the arm (Gusev and Efremov, 2013). A lack of a statistical study with a bigger sample, the difficulty of separating the effects of multiple physical mechanisms that act together, makes it challenging to find the Parker instability in action.

Large scale ordered magnetic fields also change the nature of gravitational instabilities in the plane of the disc itself. However, unlike their destabilising role in the plane

perpendicular to the disc, they can either act to stabilise or destabilise the disc. This depends upon their strength and the properties of the local shear flow. We can see this behaviour by considering an azimuthal equipartition B-field that aligns gas flows along its direction. This would thus, prevent radial motions and inhibit epicyclic oscillations. For low shearing regions, such as solid-body rotation with $q = \partial \ln \Omega / \partial \ln R = 0$, this prevents the epicyclic motions that stabilise against gravitational collapse (as seen in Section 1.4.1). This results in a "Jeans-like" instability in a rotating disc, where gravity is only opposed by pressure forces, called the Magneto-Jeans Instability (MJI) (Elmegreen, 1987; Kim and Ostriker, 2001). For regions with high shear, such as differentially rotating gas with $q = 1$ (as is often the case for galaxies), shearing motions result in growth via swing amplification mechanism (Julian and Toomre, 1966). In this case, magnetic fields act to stabilise both the shearing motions and the swing amplifier resulting from them. This is called the Magnetic Swing Amplifier (MSA) (Kim and Ostriker, 2001). However, even for the MSA, if the magnetic fields are in extremely strong ($\beta \ll 1$), they can completely prevent any shear action and transform the MSA to the MJI. One important implication of this destabilising nature of magnetic fields is that the MJI is also active at $Q \geq 1$, which allows for axisymmetric instability to proceed despite Q being above its traditional threshold.
Finally, even though the Parker instability, the MJI and MSA all work under moderate magnetisation, magnetic fields with very weak strengths ($\beta \leq 100$) also have dynamical effects in the disc. For differentially rotating discs ($q \geq 1$), magnetic tension is responsible for the radial transport of angular momentum inside-out. This is known as the Magnetorotational Instability (MRI) (Chandrasekhar, 1961; Balbus and Hawley, 1991). MRI has been proposed to generate turbulence for all kinds of astrophysical discs, be it accretion discs or galaxies (Balbus and Hawley, 1998; Kim et al., 2003).

1.5 Galactic simulations

Linear analysis offers insight into the physical mechanisms at play during the early-onset phase of instabilities, however it suffers from a few limitations. Linearising the fluid equations entails neglecting the higher-order terms, which invariably play a role in subsequent evolution since the variables grow exponentially after instability's onset. It also involves neglecting the non-linear advection term $((\vec{v}.\vec{\nabla})\vec{v})$, that is responsible for turbulence. Turbulence introduces randomness in gas flows and transfers kinetic energy from the large scale to small scales (Kolmogorov, 1941). Flows in the ISM are expected to be turbulent - due to the extremely high Reynolds number of the ISM, which is estimated to be $\sim 10^7$ for the WNM (Ferrière, 2020), and the ubiquity of turbulent driving mechanisms. There is also ample observational evidence that supports this (e.g. Larson, 1981; Armstrong et al., 1995). This makes non-linearity an essential ingredient of the ISM fluid. Apart from this, linear analysis also fails to account for processes abundant in the ISM, such as heating and cooling (c.f. Section 1.1), star formation and various feedback mechanisms (Section 1.2).
In light of these complications, numerical simulations have become the third pillar of astronomy, alongside theory and observations, in our attempts to understand ISM flows and astrophysical flows in general. Numerical simulations discretise and solve the partial differential equations of magnetohydrodynamics (equation 2-equation 7). Since there are numerous choices for both the discretisation (space or mass based for

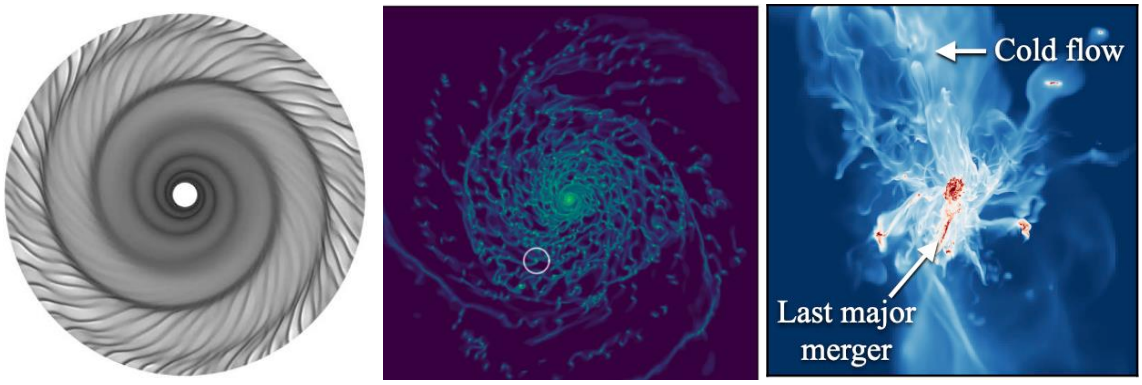

Figure 7: Snapshots from galactic simulations having varying focus and complexity. The leftmost panel, taken from Shetty and Ostriker (2006), shows a 2D isolated galaxy simulation with overlaid spiral arms. The middle panel, from Fensch et al. (2023), an isolated galaxy in 3D simulations with a zoomed-in kiloparsec region marked with a white circle. The right panel, from Agertz et al. (2021), shows a galaxy with sub-grid physics along with its external environment.

instance), as well as the specific algorithms employed to solve the resulting equations - there are a number of public community codes available for the simulations. This work employs the use of grid-based code `FLASH`, that uses spatial discretisation. `FLASH` is a modular, scalable and portable code written in `FORTRAN90` and `C`. It uses the Message-Passing Interface (MPI) library[3] for achieving parallelisation through inter-processor communication, along with the HDF5 library[4] for parallel Input/Output. Moreover, it employs an adaptive grid, where the size of the grid cells in the spatial domain can be varied upon user's discretion. This offers a more economical use of computational resources and is achieved in the code using an oct-tree data structure to store the data using the `PARAMESH` library (MacNeice et al., 2000).

Starting from one or 2D hydrodynamical simulations with very limited resolutions (e.g. Johns and Nelson, 1986; Kim et al., 2002), galaxy simulations have evolved considerably. Coupled advancements in both the hardware and computational software have made this possible. Comparing the peak computing power of a typical cluster in 1990's (Beowulf cluster[5]) of a few Gflops, to the cluster used in this work (Gadi[6]), which has a computational capacity of a few Pflops. We see a rise of around 7 orders in magnitude. Even with such gains, galaxy simulations still have to limit their scientific focus. This usually involves a trade-off for an economical use of computational resources. For instance, there are "realistic" galaxy simulations that employ sub-grid models in addition to hydrodynamics, such as models of star formation and their various feedback mechanisms, on-the-fly chemical reactions, radiative transfer (e.g. Goldbaum et al., 2016; Jeffreson et al., 2020; Khullar et al., 2024) etc. Another broad category that stands in contrast to this, has a focus on "minimal numerical experiments". These simulations purposefully reduce the complexity of the problem by choosing to include only a sub-set of physics. This is done in order to discern and understand the role of different physical mechanisms on a particular phenomena (e.g.

[3]https://www.open-mpi.org/
[4]https://www.hdfgroup.org/
[5]https://www.computerhistory.org/revolution/supercomputers/10/71/909
[6]https://nci.org.au/our-systems/hpc-systems

Wang et al., 2010; Fensch et al., 2023).
Figure 7 shows examples of three galactic simulations that exhibit this variety. The left-most panel is a snapshot from a hydrodynamical simulation of an isolated, isothermal razor-thin galaxy with an external spiral potential and resolution of ≈ 30 pc from Shetty and Ostriker (2006). The middle panel is a snapshot of a more recent 3D hydrodynamical simulation of an isolated galaxy, taken from Fensch et al. (2023), with a kiloparsec scale patch (marked in white circle) that reaches resolutions of ≈ 0.1 pc. An improvement of over 2 orders in magnitude in the range of physical scales simulated in these minimal numerical experiments. The rightmost panel, in contrast to the other two, shows a realistic simulation that has a star formation sub-grid model along with feedback prescriptions (from Agertz et al. (2021)) and its cosmological environment as well.

2 Paper I

Contribution

The idea of the work was author's own and he performed the simulations, developed the analysis methods and wrote the manuscript. Bastian Körtgen provided the numerical setup used in this work. Christoph Federrath and Robi Banerjee held weekly discussions and edited the manuscript.

A&A, 687, A276 (2024)
https://doi.org/10.1051/0004-6361/202348719

Astronomy & Astrophysics

Role of magnetic fields in disc galaxies: spiral arm instability*

Raghav Arora[1], Christoph Federrath[2], Robi Banerjee[1], and Bastian Körtgen[1]

[1] Hamburger Sternwarte, Universität Hamburg, Gojenbergsweg 112, 21029 Hamburg, Germany
e-mail: raghav.arora@hs.uni-hamburg.de
[2] Research School of Astronomy and Astrophysics, The Australian National University, Canberra, ACT 2611, Australia

Received 23 November 2023 / Accepted 15 April 2024

ABSTRACT

Context. Regularly spaced star-forming regions along the spiral arms of nearby galaxies provide insight into the early stages and initial conditions of star formation. The regular separation of these star-forming regions suggests spiral arm instability as their origin.
Aims. We explore the effects of magnetic fields on the spiral arm instability.
Methods. We use 3D global magnetohydrodynamical simulations of isolated spiral galaxies, comparing three different initial plasma β values (ratios of the thermal to magnetic pressure) of $\beta = \infty$, 50, and 10. We perform a Fourier analysis to calculate the separation of the over-dense regions that formed as a result of the spiral instability. We then compare the separations with observations.
Results. We find that the spiral arms in the hydro case ($\beta = \infty$) are unstable. The fragments are initially connected by gas streams that are reminiscent of the Kelvin-Helmholtz instability. For $\beta = 50$, the spiral arms also fragment, but the fragments separate earlier and tend to be slightly elongated in the direction perpendicular to the spiral arms. However, in the $\beta = 10$ run, the arms are stabilised against fragmentation by magnetic pressure. Despite the difference in the initial magnetic field strengths of the $\beta = 50$ and 10 runs, the magnetic field is amplified to $\beta_{\rm arm} \sim 1$ inside the spiral arms for both runs. The spiral arms in the unstable cases (hydro and $\beta = 50$) fragment into regularly spaced over-dense regions. We determine their separation to be ∼0.5 kpc in the hydro and ∼0.65 kpc in the $\beta = 50$ case. These two values agree with the observed values found in nearby galaxies. We find a smaller median characteristic wavelength of the over-densities along the spiral arms of $0.73^{+0.31}_{-0.36}$ kpc in the hydro case compared to $0.98^{+0.49}_{-0.46}$ kpc in the $\beta = 50$ case. Moreover, we find a higher growth rate of the over-densities in the $\beta = 50$ run compared to the hydro run. We observe magnetic hills and valleys along the fragmented arms in the $\beta = 50$ run, which is characteristic of the Parker instability.

Key words. instabilities – magnetohydrodynamics (MHD) – stars: formation – ISM: magnetic fields – galaxies: ISM

1. Introduction

Star formation in spiral galaxies is driven by their spiral arms (Nguyen et al. 2017). Star-forming regions that resemble a beads-on-a-string pattern are ubiquitous in spiral arms of numerous nearby galaxies, even though their morphological features and physical properties are different (e.g. Elmegreen & Elmegreen 1983; Elmegreen et al. 2006). Recently, spiral arms were also seen in rings of barred (Gusev & Shimanovskaya 2020) and lenticular galaxies (Proshina et al. 2022). These star-forming regions are found to be bright in the IR (Elmegreen et al. 2006, 2018; Elmegreen & Elmegreen 2019) and at times also in the far-UV (FUV) and Hα (Efremov 2009, 2010; Gusev & Efremov 2013; Gusev et al. 2022) emission, where they trace various stages of star formation. Despite the variety in spiral galaxies that host these regular star-forming regions, the adjacent separations of these regions fall in the range 350−500 pc and (or) integer multiples of this range (cf. Gusev et al. 2022). For example, it was found that the adjacent separation of star-forming regions in the spiral arms of NGC 628 and M 100 were both ∼400 pc (Gusev & Efremov 2013; Elmegreen et al. 2018). Another prominent example is the north-western arm of M 31, where star complexes with a spacing of twice this value ∼1.1 kpc were found (Efremov 2009, 2010). This characteristic separation of these star-forming regions in spiral arms indicates that their origin might be through a spiral arm instability. Another interesting feature observed together with regular star-forming regions in M 31 were magnetic fields out of the plane of the galaxy, with a wavelength twice that of the adjacent separation of these regions (Efremov 2009, 2010). This indicates that magnetic fields could play an important role in the formation of these regions.

Beads-on-a-string patterns have been observed along spiral arms in numerical simulations (e.g. Chakrabarti et al. 2003; Wada & Koda 2004; Kim & Ostriker 2006; Shetty & Ostriker 2006; Wada 2008; Renaud et al. 2013). The physical mechanism responsible, however, has been debated. It was hypothesised to be the Kelvin-Helmholtz (KH) hydrodynamical instability (Wada & Koda 2004), an artefact of numerical noise (Hanawa & Kikuchi 2012) or of infinitesimally flat 2D discs (Kim & Ostriker 2006), a magnetic Jeans instability (MJI; Kim & Ostriker 2006), which was also called the feathering instability (Lee 2014), or a hydro instability along spiral shocks distinct from the KH instability, called the wiggle instability (Kim et al. 2014, WI). Its physical nature was recently established to be a combination of KHI (as proposed in Wada & Koda 2004) and a vorticity-generating instability due to repeated passages of spiral shocks (Mandowara et al. 2022). Restricting their physical setups to different physical processes, these works reported facets of the same physical instability around the spiral shock. However, we also know from 2D local simulations and linear analysis (Mandowara et al. 2022) that the spiral instability is highly non-linear and sensitive to the physical properties

* Movies are available at https://www.aanda.org

of the interstellar medium (ISM). This includes the sound speed (c_s) and the strength of the spiral shock. One of these important factors are magnetic fields.

Even though the role of magnetic fields has been explored, the effect they can have in a global realistic setting still remains to be determined. We expect from earlier works that they can affect the length and growth scales of the instability. For example, Lee (2014) showed that the spiral shock fronts were weaker in the presence of stronger magnetic fields, and the feather instability growth rate was not affected. However, the range of their parameter space only spanned from $\beta = 2$–4. Kim et al. (2014) reported based on a 2D local linear analysis and simulations that equipartition magnetic fields ($\beta = 1$) in comparison with very weak fields ($\beta = 100$) decreased the growth rate of the spiral arm instability by a factor of 4 and increased the wavelength of the dominant mode by a factor of 2 and had an overall stabalising effect overall. In 3D local box simulations, Kim & Ostriker (2006) found no vorticity generating instability and attributed this to magnetic fields ($\beta = 1$, 10), but found that the spiral shocks were still unstable in the presence of self-gravity and magnetic fields. This was also confirmed in global 2D simulations in Shetty & Ostriker (2006), where equipartition magnetic field strengths prevented the pure hydro vortical instability, but the spiral arms fragmented in the presence of self-gravity despite the magnetic fields. Most of these studies were made in 2D (Lee 2014; Kim et al. 2015; Shetty & Ostriker 2006) or were local (Lee 2014; Kim et al. 2015; Kim & Ostriker 2006), and all of them were isothermal. While there are more sophisticated magnetised galaxy simulations (Dobbs & Price 2008; Khoperskov & Khrapov 2018), they have focused on the global evolution of the disc and not on the spiral arm instability. It is yet to be determined how magnetic fields affect the spiral arm instability in 3D global disc galaxy simulations, where the spiral arm instability, MJI, and also the Parker instability (Parker 1966) that arises due to the stratified nature of the medium perpendicular to the disc are resolved.

In this study, we focus on the physical effects of magnetic fields on the spiral arm instability and its impact on the spacings of the over-densities that result in the spiral arms. We perform 3D self-gravitating magnetised disc galaxy simulations that employ fitted functions for equilibrium cooling, heating, and an external spiral potential. This allows us to capture the spiral arm instability in a more realistic environment and to study the effects of magnetic fields on it. For this purpose, we built a library of simulations with varying initial magnetisation.

The paper is organised as follows: Section 2 describes our library of simulations. In Sect. 3, we compare the models with different magnetisations and focus on the basic morphology of our galaxies, the approximate timescales of the spiral arm instability, and the cloud spacings of the unstable spiral arms. We discuss the caveats of this work and the role played by magnetic fields on the spiral arm instability, and we compare them with existing observations and simulations in Sect. 4. We summarise our results in Sect. 5.

2. Methods

Our 3D magnetohydrodynamical (MHD) disc galaxy simulations have self-gravity, an external spiral potential, magnetic fields, and fitted functions for optically thin cooling and heating that include heating from cosmic and soft X-rays, the photoelectric effect, and the formation and dissociation of H_2 (cf. Körtgen et al. 2019). The cooling and heating gives us a multiphase ISM consisting of the warm neutral medium (WNM), cold neutral medium (CNM), and a cold molecular medium (CMM). These form self-consistently in our simulations. The cooling and heating curve also has a thermally unstable regime, which is important for molecular cloud formation, in the density range $1 \leq n/\mathrm{cm}^{-3} \leq 10$. Our minimalist global models strike a balance by including dominant physical effects such as self-gravity, galactic shear, thermal instabilities, and magnetic fields, while at the same time avoiding complicated stochastic effects such as star formation and various feedback mechanisms. We do not study these mechanisms here because we focus on the effects of magnetic fields. We defer an investigation of the effects of feedback to a future study.

The system of equations that we solve is

$$\frac{\partial \rho}{\partial t} + \nabla.(\rho \boldsymbol{v}) = 0, \tag{1}$$

$$\frac{\partial (\rho \boldsymbol{v})}{\partial t} + \nabla \cdot (\rho \boldsymbol{v}\boldsymbol{v}) = -\nabla P - \nabla(\Phi_{\rm ext} + \Phi) + \frac{1}{4\pi}(\nabla \times \boldsymbol{B}) \times \boldsymbol{B}, \tag{2}$$

$$\frac{\partial \boldsymbol{B}}{\partial t} = \nabla \times (\boldsymbol{v} \times \boldsymbol{B}), \tag{3}$$

$$\nabla^2 \Phi = 4\pi G \rho, \tag{4}$$

$$\frac{\partial}{\partial t}\left(\frac{\rho v^2}{2} + \rho \epsilon_{\rm int} + \frac{B^2}{8\pi}\right) + \nabla \cdot \left[\left(\frac{\rho v^2}{2} + P + \rho \epsilon_{\rm int} + \frac{B^2}{8\pi}\right) \cdot \boldsymbol{v} + v_j \mathcal{M}_{ij}\right] = \frac{\rho}{m_{\rm H}}\Gamma - \left(\frac{\rho}{m_{\rm H}}\right)^2 \Lambda(T), \tag{5}$$

where ρ is the density, and $\boldsymbol{v}$, P, $\boldsymbol{B}$ are the velocity, pressure and the magnetic field of the gas. The gravitational potential of the gas and the external gravitational potential are given by Φ, $\Phi_{\rm ext}$. $m_{\rm H}$ is the mass of the hydrogen atom, and Γ, Λ are the heating and cooling rates, respectively (Koyama & Inutsuka 2002; Vázquez-Semadeni et al. 2007). $\mathcal{M}_{ij} = \frac{B^2}{8\pi}\delta_{ij} - \frac{B_i B_j}{4\pi}$, and we use the polytropic equation of state, which gives $\epsilon_{\rm int} = P/\rho(\gamma - 1)$, where $\gamma = 5/3$. These represent the ideal MHD equations, where we have neglected the magnetic diffusivity and fluid viscosity.

We use the FLASH (Fryxell et al. 2000; Dubey et al. 2008) grid-based MHD code to perform the simulations. The disc is initialised at the centre of a cuboidal box with a side length $L_{xy} = 30$ kpc in the plane of the disc and $L_z = 3.75$ kpc in the direction perpendicular to it. The minimum cell size of the base grid is 234 pc, that is, the base grid has a resolution of $128 \times 128 \times 16$ cells. However, we achieve a maximum resolution corresponding to a minimum cell size of 7.3 pc by using adaptive mesh refinement (AMR) with five levels of refinement, corresponding to a maximum effective resolution of $4096 \times 4096 \times 512$ cells, such that the local Jeans length was resolved with at least 32 grid cells (Federrath et al. 2011) for $R \geq 5$ kpc. We do this in two steps. First, we use four levels of refinement for the initial $0.3\,T_{\rm rot}$ (100 Myr) of the evolution. We then increase the maximum refinement level to five, which saves computational costs in the initial phases of the evolution, and allows us to achieve a higher refinement overall when the spiral arms start to develop. The initial Jeans length in our models is ∼1.8 kpc, and thus, we resolve it by two additional levels of refinement at the start. In order to avoid artificial fragmentation on the highest level of refinement due to violation of the Truelove criteria (Truelove et al. 1997), we have added an artificial pressure term that was adjusted so that the local Jeans length is resolved with at least four grid cells (Körtgen et al. 2019).

2.1. Basic setup

As in earlier studies (cf. Körtgen et al. 2018, 2019), we initialise the disc galaxies in our simulation suite by keeping the effective Toomre parameter ($Q_{\rm eff}$) constant, defined as

$$Q_{\rm eff} = \frac{\kappa\left(c_{\rm s}^2 + v_{\rm a}^2\right)^{1/2}}{\pi G\Sigma}, \tag{6}$$

where $\kappa = \sqrt{2}v_{\rm c}/r$ and Σ are the epicyclic frequency and the surface density of the disc, $c_{\rm s}$ is the sound speed, and $v_{\rm a}$ is the Alfvén speed of the medium. We do this so that all the simulations have a similar response to axisymmetric gravitational perturbations. Next, we use the scale height radial profile, $H(R)$, from HI observations of the Milky Way (Binney & Merrifield 1998), which gives us

$$\rho(R,z) = \frac{\kappa c_{\rm s}\sqrt{1+2\beta^{-1}}}{2\pi G Q_{\rm eff} H(R)}{\rm sech}^2\left(\frac{z}{H(R)}\right), \tag{7}$$

where $H(R) = R_\odot(0.0085 + 0.01719\,R/R_\odot + 0.00564(R/R_\odot)^2)$ with $R_\odot = 8.5$ kpc and $\beta = 2c_{\rm s}^2/v_{\rm a}^2$ is the plasma-beta (ratio of the thermal to magnetic pressure) of the disc. For numerical reasons, we define the inner 5 kpc region to be gravitationally stable and keep it unresolved with $Q_{\rm eff} = 20$. We focus on the disc with $R > 5$ kpc, where we have the initial $Q_{\rm eff} = 3$, making the region of interest gravitationally stable to axisymmetric perturbations since $Q \geq 1$. We also have pressure equilibrium at the boundaries to avoid any gas inflows and outflows for the same reason. We further apply a buffer zone of 1 kpc from the inner disc for our analysis to avoid any boundary effects.

We adopt a flat rotation curve for our galaxies, with the circular velocity in the plane of the galaxy given by

$$v_{\rm rot} = v_{\rm c}\frac{R}{\sqrt{R_{\rm c}^2 + R^2}}, \tag{8}$$

where $v_{\rm c} = 200\,{\rm km\,s^{-1}}$ for Milky Way-like galaxies, and $R_{\rm c} = 0.5$ kpc is the core radius. This is the exact solution for the adopted dark matter potential,

$$\Phi_{\rm dm} = \frac{1}{2}v_{\rm c}^2\ln\left\{\frac{1}{R_{\rm c}^2}\left[R_{\rm c}^2 + R^2 + \left(\frac{z}{q}\right)^2\right]\right\}. \tag{9}$$

We use a marginally lower value of $v_{\rm c} = 150\,{\rm km\,s^{-1}}$ compared to the Milky Way. We do this to isolate and focus on the effects of the spiral instability from the presence of swing instabilities in a low-shear environment.

2.2. Turbulent initial conditions

In addition to the circular velocity of the disc, we add a turbulent initial velocity field with $v_{\rm rms} = 10\,{\rm km\,s^{-1}}$ and a Kolmogorov scaling of $k^{-5/3}$ on scales [50, 200] pc. The turbulent velocity field was constructed to have a natural mixture of solenoidal and compressible modes, generated with the methods described in Federrath et al. (2010), using the publicly available `TurbGen` code (Federrath et al. 2022). The details of the initial turbulent perturbations are not critical for our numerical experiments, and they primarily serve to break the symmetries in the idealised setup. They also ensure that the perturbations for the instabilities under investigation here develop self-consistently and are not seeded by numerical noise. After the initial turbulent seeds have decayed, the ISM turbulence is primarily driven by gas flows and spiral arm dynamics.

2.3. Magnetic field

Magnetic fields are observed in nearby disc galaxies to be roughly in equipartition with the turbulent kinetic energy and in super-equipartition with the thermal energy in the ISM (Beck 2015, and references therein). We characterise the strength of the magnetic field with the plasma-beta (β), that is, the ratio of the thermal to the magnetic pressure of the medium, which is also equal to the ratio of the thermal to magnetic energies. Our initial values are $\beta \in \{\infty, 50, 10\}$, which represent the hydro, weak, and moderate magnetisation cases of our disc. We chose a higher value of β than observed ($\beta_{\rm obs} \leq 1$) because we expect it to decrease with the dynamical evolution of the galaxy. We initialise the magnetic fields to be completely toroidal ($m = 0$ mode), which is the dominant mode found in galaxies (Beck et al. 2020), with a dependence on the gas density, such that $B \propto n^\alpha$, where $\alpha = 0.5$ (as done in Körtgen et al. 2019).

2.4. Spiral potential

For generating the spiral arms, we adopt a rigidly rotating two-armed spiral potential (Cox & Gómez 2002) with a pattern speed of $13.34\,{\rm km\,s^{-1}\,kpc^{-1}}$, which gives us a co-rotation radius of =11.25 kpc and a pitch angle of $\alpha = 20°$. Thus, the external gravitational potential can be written as

$$\Phi_{\rm ext} = \Phi_{\rm dm} + \Phi_{\rm sp}, \tag{10}$$

where $\Phi_{\rm dm}$ is the dark matter potential that provides the flat rotation curve (Eq. (9)), and $\Phi_{\rm sp}$ is the spiral potential (cf. Eq. (8) in Cox & Gómez 2002). We chose the amplitude of the spiral such that the magnitude of the force due to the potential is ∼0.4 times that of the dark matter potential on average, analytically given by

$$\mathcal{F}_{\rm sp} = \left\langle\frac{\langle f_{\rm sp}\rangle_\phi}{f_{\rm dm}}\right\rangle_r \sim 0.40, \tag{11}$$

where $\langle f_{\rm sp}\rangle_\phi$ is the azimuthal average of $f_{\rm sp} = \nabla\Phi_{\rm sp}$ and $\langle\ldots\rangle_r$ denotes the radial average, taken over 6 to 11 kpc, which is our region of interest.

2.5. Simulation parameter study

Our library of simulations contains three runs having different initial magnetisations, with $\beta \in \{\infty, 50, 10\}$, all with the same strength of the spiral arm perturbation, $\mathcal{F}_{\rm sp} = 0.4$, a rotational velocity of $v_{\rm c} = 150\,{\rm km\,s^{-1}}$, and an effective $Q = 3$. From Eq. (7), it follows that fixing these values leads to an initial density field that differs only slightly (by ≤2%) between the simulations with different β. The key initial parameters are summarised in Table 1, where we also list the mass-weighted average density (n), the sound speed ($c_{\rm s}$), and the magnetic field magnitude of the disc region of interest. With this parameter set, we initialise our galaxies to be marginally stable to axisymmetric gravitational instabilities, the thermal instability as well as swing instabilities. Since we have an initial $Q > 1$, the mid-plane density is a factor of 2 lower than the thermally unstable regime, and the shear environment is low with $v_{\rm c} = 150\,{\rm km\,s^{-1}}$.

3. Results

Here, we discuss the main results of our simulations. First, we describe the basic evolution of the three runs, that is, their general morphology and the timescales of the spiral arm formation

Table 1. Initial conditions of the simulations.

Simulation number	β	Q	n (cm^{-3})	v_c (km s^{-1})	c_s (km s^{-1})	$\boldsymbol{B}$ (μG)	$\mathcal{F}_{sp}$	Spiral arm stability
1	∞	3	0.58	150	8.13	0	40%	Unstable
2	50	3	0.59	150	8.11	0.69	40%	Unstable
3	10	3	0.64	150	8.01	1.60	40%	Stable

Notes. The c_s and the B_{mag} are the mass-weighted averages of the disc region between $r = 6$ kpc and 10 kpc and $|z| \leq H$ (at: $R = 8.5$ kpc), calculated at $t = 2$ Myr.

and fragmentation in Sect. 3.1. In Sect. 3.2, we focus on the cases where the spiral arms fragment into over-dense regions. We also describe our method for extracting the separation of the clouds and then report them as well. We then present the physical properties of the spiral arms and the effects that magnetic fields have on them in Sect. 3.3.

3.1. Basic evolution

Here, we describe the basic morphology and evolution of our simulations. We first discuss the spiral arms that form self-consistently and then their subsequent fragmentation patterns in Sect. 3.1.1. We then quantify the timescales over which we see this evolution in Sect. 3.1.2.

3.1.1. Morphology

The basic morphology of the dense gas in our galaxy is presented in Fig. 1, where we show the projected density of the three models. The lower limit of the colour bar is chosen such that the denser and colder regions are highlighted in the simulations. The rows represent different time snapshots as indicated in the panels, and the columns represent the runs with varying magnetisation. Starting with the first row ($t = 0.5\,T_{rot}$), we can immediately see that the dense gas is dominantly present in the spiral arms. We can understand this simply by looking at the relevant drivers of the gas dynamics in the system. Since the rotation curve that we use is the analytical solution to the dark matter potential, it is the self-gravity, the magnetic fields, the external spiral potential, and the equilibrium cooling and heating that drive the time evolution of the gaseous disc. The spiral potential funnels the gas towards its minima. This forms the dense spiral arms in the presence of self-gravity and cooling, while the magnetic fields oppose this by magnetic pressure ($P_{mag} = B^2/8\pi$). Moreover, since the initial parameters of the galaxy are such that it is stable to Toomre, thermal and swing instabilities, the spiral arms dominates the formation of dense gas in our galaxies. We can see the effect of magnetic fields even as the spiral arms are forming, when we compare the three runs in the first row of Fig. 1. The spiral arms are visibly more diffuse with increasing magnetisation due to the additional pressure support of the magnetic fields. As expected, this effect is more pronounced in the $\beta = 10$ case because the β of the gas is considerably larger in this case than in the $\beta = 50$ run, where the magnetic fields are sub-dominant in the initial phases of the evolution.

We begin to see major differences in the evolutionary paths of the spiral arms between the three runs after they form, as seen in the next panel at $t = 0.75\,T_{rot}$, where the arms start fragmenting into a beads-on-a-string pattern for the hydro and $\beta = 50$ runs, while on the other hand, the spiral arms are diffusing away in the $\beta = 10$ case. This then leads to stark differences at $t = 0.9\,T_{rot}$, where the spiral arms that we see at $t = 0.75\,T_{rot}$ have distinctly separated into clouds for the hydro and $\beta = 50$ cases. While they are diffused away in the $\beta = 10$ case. Moreover, we see secondary arm formation for all the three cases, visible on the inner face of the fragmented arms in the hydro and $\beta = 50$ cases, and in the absence of a fragmented arm, solitary in the $\beta = 10$ case. We continue running the $\beta = 10$ simulation for $t = 1.67\,T_{rot}$ and observe that the disc goes through cycles of arm formation and diffusion, and that these arms never fragment.

Now, we focus on the two runs where we see the spiral arms fragment, namely $\beta = \infty, 50$. In the Fig. 1 we can see morphological differences between the two runs at $t = 0.75\,T_{rot}$, even though there are no notable differences at $t = 0.5\,T_{rot}$, when the spiral arms form. The differences are seen in the Fig. 2, where we plot the projected density of the two runs and highlight the cells in the spiral arms with a different colour scheme to accentuate the difference. The two rows are at different times, analogous to the last two rows in Fig. 1. We trace one of the arms using a friends-of-friends (FoF) algorithm with a linking length of 60 pc, using cells that are on the verge of being thermally unstable with $n_{thresh} = 0.9\,n_{crit}$, where $n_{crit} = 1$ cm^{-3} is the critical density of the thermally unstable medium. In the first panel, at $t = 0.75\,T_{rot}$, we can see that the dense structures in the $\beta = 50$ run are all radially elongated, while the $\beta = \infty$ run has roughly sphere-shaped overdensities. The second difference is that we see wiggles that are reminiscent of Kelvin-Helmholtz instabilities, which are continuously connected with the gas in the spiral arms in the hydro run. On the other hand, the spiral arms separate out into distinct clouds without any Kelvin-Helmholtz-like structures in the runs with magnetic fields. There are differences that persist even at late times. At $t = 0.9\,T_{rot}$ in Fig. 2 we see a larger number of fragments are more closely packed in the hydro run than in the magnetic field runs. This suggests that the fragmentation mode with magnetic fields is different from that without magnetic fields.

3.1.2. Timescales

A more quantitative picture of the time evolution of the dense gas is presented in Fig. 3. Here, we show the time evolution of the mass-weighted average density of the gas above the density threshold for the thermally unstable regime, $n > 1$ cm^{-3}. This is representative of gas that has the potential to become denser because it is in the thermally unstable regime. As expected, we find that this traced dense gas is predominantly present in the spiral arms. We visually confirm this by following the evolution of the disc with 10^5 passive tracer particles that are initialised at $t = 0$ in our region of interest (movies are provided in the supplementary material). The three solid lines in Fig. 3 are the three runs with different initial magnetisations. The stars indicate the times at which we show the disc in Fig. 1. We can separate the time evolution of the dense gas into two phases. In one phase,

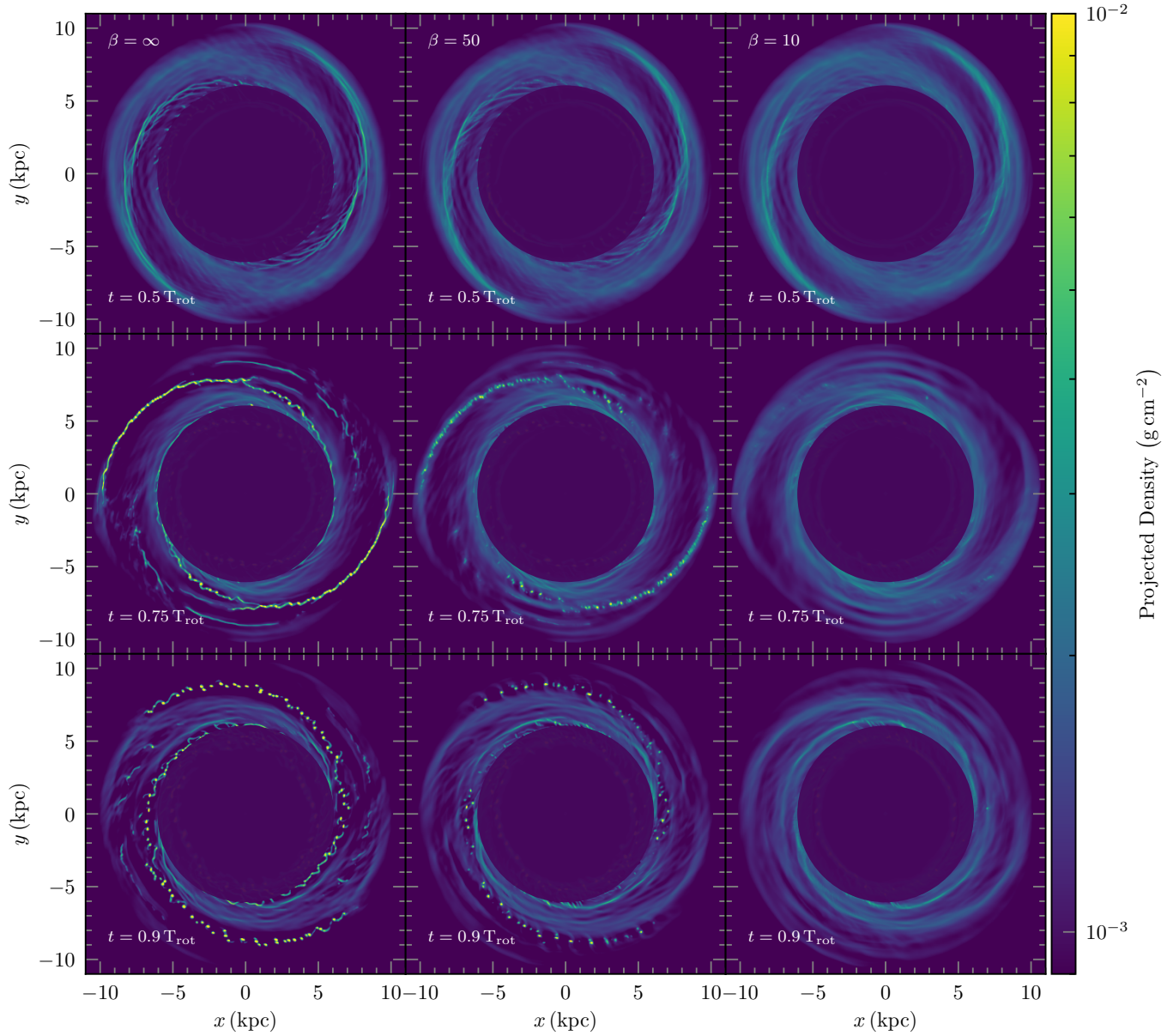

Fig. 1. Column density of the disc galaxies projected onto the z-plane. The columns represent the initial plasma β (ratio of thermal to magnetic pressure) of the runs, and the rows from top to bottom show the evolution of the galaxy. The panels roughly depict the times when the spiral arms first form, when the arms fragment into over-densities, and when they separate out into clouds. The disc becomes more diffuse with decreasing plasma β in the first row. The second and the third row highlight the magnetic field effects on the stability of the spiral arms. The $\beta = 10$ run is stable to fragmentation, while the hydro and $\beta = 50$ cases fragment and yet still have noticeable morphological differences.

the spiral arms grow, and in the second phase, the gas either fragments into clouds or diffuses. The spiral arm growth phase starts at $t \simeq 0.3\,T_{\rm rot}$ (100 Myr) for all the runs and lasts until $t \simeq 0.64\,T_{\rm rot}$ (210 Myr) for the hydro and $t \sim 0.70\,T_{\rm rot}$ (230 Myr) for the $\beta = 50$ run. In the $\beta = 10$ case, on the other hand, even though the spiral arms have an appreciable amount of gas around $n \sim 1\,{\rm cm}^{-3}$ (cf. Fig. 1), the arms never get denser. In the next phase of the evolution, the $\beta = 10$ run repeatedly forms transient arms that quickly diffuse after their formation. This phase is seen as small crests and troughs in the Fig. 3 at $t \simeq 0.54$, 0.74, $0.9\,T_{\rm rot}$. In contrast, the spiral arms in the other two cases fragment. This is visible as a sudden change in the slope of $\ln \bar{n}$ in the same figure Fig. 3, which marks the end of the spiral arm growth phase. During this phase, the average density rises at a faster rate in the $\beta = 50$ case than in the hydro run. For similar time intervals from $t = 230$ to $t = 290$ Myr, the density rises by a factor of just 2.2 for the hydro run, in contrast to the factor of 5 in the magnetic run. This is seen in the steeper slope of the former compared to the latter in Fig. 3. Looking at the tracer particle movies, we see that the hydro run separates into distinct clouds at around $t \simeq 290$ Myr, while the $\beta = 50$ run does this much quicker by $t \simeq 270$ Myr.

3.2. Cloud separation and fragmentation modes

Here we discuss the difference in the separation (spacing) of the clouds that form in the spiral arms of the $\beta = 50$ case and the hydro case. This gives us insight into the effects of the magnetic fields and on the fastest-growing mode of the spiral instability.

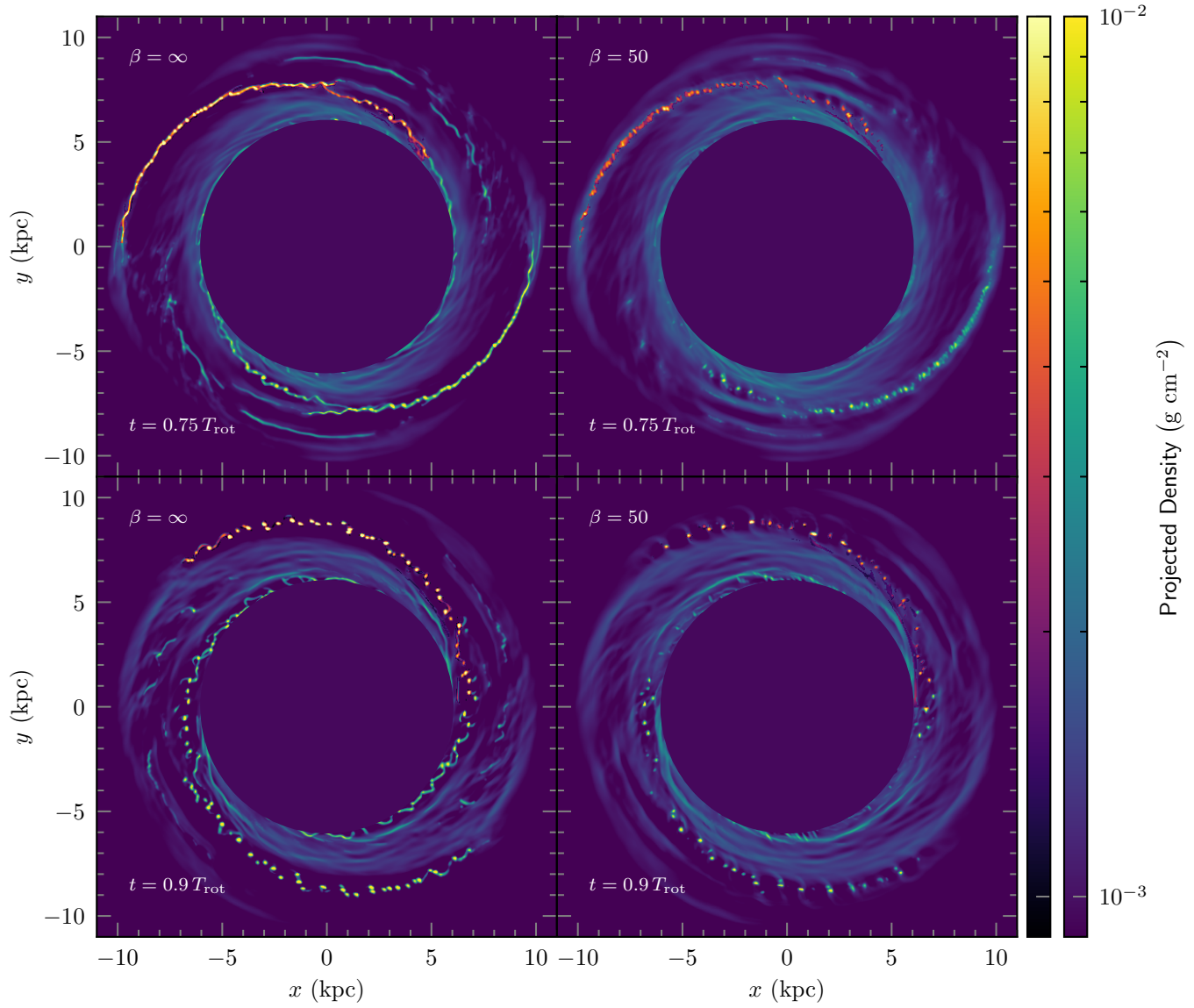

Fig. 2. Projected density as in Fig. 1, but only for the fragmenting cases ($\beta = \infty$ and 50). One of the arms is traced and highlighted in a different colour scheme. We can see morphological differences in the manner in which the spiral arm fragments in the presence of magnetic fields.

3.2.1. Extracting the cloud spacing

We quantify the separation of the clouds and the wavelength of the unstable modes by using a 1D Fourier analysis. We do this on the projected density binned along the length of the spiral arms. We first construct a spiral arm mask using analytical functions and then use this spiral coordinate to bin the density in preparation for the Fourier transformation.

Similar to Roberts (1969), we define

$$\xi = \ln(R/R_0)\sin p + \theta\cos p, \tag{12}$$
$$\eta = \ln(R/R_0)\cos p - \theta\sin p \tag{13}$$

as the spiral arm coordinates, where $R_0 = 1$ kpc is the scaling, and p is the pitch angle of the spiral arm under consideration. The (ξ, η) coordinates can be thought of as the $(\ln R, \theta)$-plane rotated counter-clockwise by the angle p. Here, ξ is the coordinate along the spiral arm, and η is locally perpendicular to it. To define a spiral arm region of a certain thickness, we use a rectangular mask in the (ξ, η)-plane, where the thickness is decided by the extent in the η coordinate. Our spiral arm mask is shown in Fig. 4, where the first panel shows the projected density of the galaxy at $t = 0.75\,T_{\rm rot}$ in the $(\ln R, \theta)$ plane along with the masked region (shaded) and the unit coordinate vectors $(\hat{e}_\xi, \hat{e}_\eta)$ at the bottom edge of the mask. The same plot is shown in the (x, y) plane in the second panel, and the third panel shows the binned projected density along the spiral arm (coordinate ξ). We construct the mask starting with an initial guess for the pitch angle, p_i, that determines the (ξ, η) plane. Next, we draw the rectangular mask in this plane that is then a rectangle bounded via fixed values of the lower edge $(\ln R_0, \theta_0)$ and the maximum radial coordinate $(\ln R_{\rm max})$, which we determine via visual inspection at the beginning. We then test the correctness of this initial rectangular mask by fitting a straight line to all the $(\ln R, \theta)$ coordinates of cells that lie in this mask, weighted by their densities. If it were a good mask that covers all the dense regions, then the slope of this line $m_{\rm line}$ would be close to $m_i = \tan p_i$. However, if it is not the case, we use it for the next iteration, where $p_{i+1} = \tan^{-1}(m_i)$. For convergence, we use an absolute tolerance of $p_{i+1} - p_i = 0.05°$. After we construct the mask, we simply bin the projected density on the coordinate along the spiral arm.

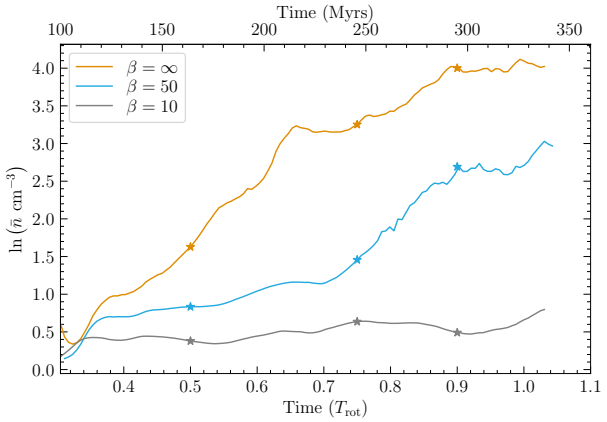

Fig. 3. Time evolution of the mass-weighted mean density ($\bar{n}$) of all the cells with $n \geq 1\,\mathrm{cm}^{-3}$. The bottom abscissa shows the time normalised by the rotation period, and the top abscissa shows the absolute time. The stars mark the times at which we show the disc morphology in the Fig. 1. The $\beta = 10$ case lacks appreciable mass above the threshold density of $1\,\mathrm{cm}^{-3}$, as opposed to the other two cases. After $t = 0.75\,T_{\rm rot}$, the mean density of the $\beta = 10$ run decreases slightly as the spiral arms diffuse, while it rises in the other two cases as the arms fragment into denser clouds.

Our algorithm is similar to what Gusev & Efremov (2013) used on observational data, but with one key difference. Here, we explicitly allow for a certain thickness of the spiral arm mask in the direction perpendicular to its length, while Gusev & Efremov (2013) did not. Instead, they just fit the curve $\eta = \text{const.}$ by selecting all the pixels that lay along the spiral arm by eye and determined the pitch angle p of the spiral arm via a least-squares fit.

The projected density on the coordinate along the spiral arm is shown in the bottom panel of Fig. 4. Here, the peaks in the column density are the encountered over-densities along the length of the spiral arm. We chose the number of bins such that there are ≥4 cells in each bin. With this binned density, we finally take the 1D discrete Fourier transform with the following convention:

$$\hat{\Sigma}_{\rm sp}[k] = \frac{1}{N}\sum_{m=0}^{N-1}\Sigma_{\rm sp,rel}[m]\exp\left(\frac{-2\pi i k m}{N}\right), \quad k = 0, 1, \ldots, N-1, \tag{14}$$

where N is the total number of bins, $\Sigma_{\rm sp,rel}[m] = \Sigma_{\rm sp}[m]/\bar{\Sigma}_{\rm sp} - 1$ is the relative surface density along the spiral in the mth bin, and k is the wave number in units of $1/L_{\rm spiral}$, with $L_{\rm spiral}$ being the length of the spiral arm. We calculate $L_{\rm spiral}$ by averaging over the lengths of the inner and outer edge of the spiral arms. The power is then taken to be

$$P[k] = \hat{\Sigma}_{\rm sp}[k]\hat{\Sigma}^{*}_{\rm sp}[k], \tag{15}$$

where $\hat{\Sigma}^{*}_{\rm sp}[k]$ is the complex conjugate of $\hat{\Sigma}_{\rm sp}[k]$. As a final step, we bin the resultant power spectrum in bins of length $k = 2$.

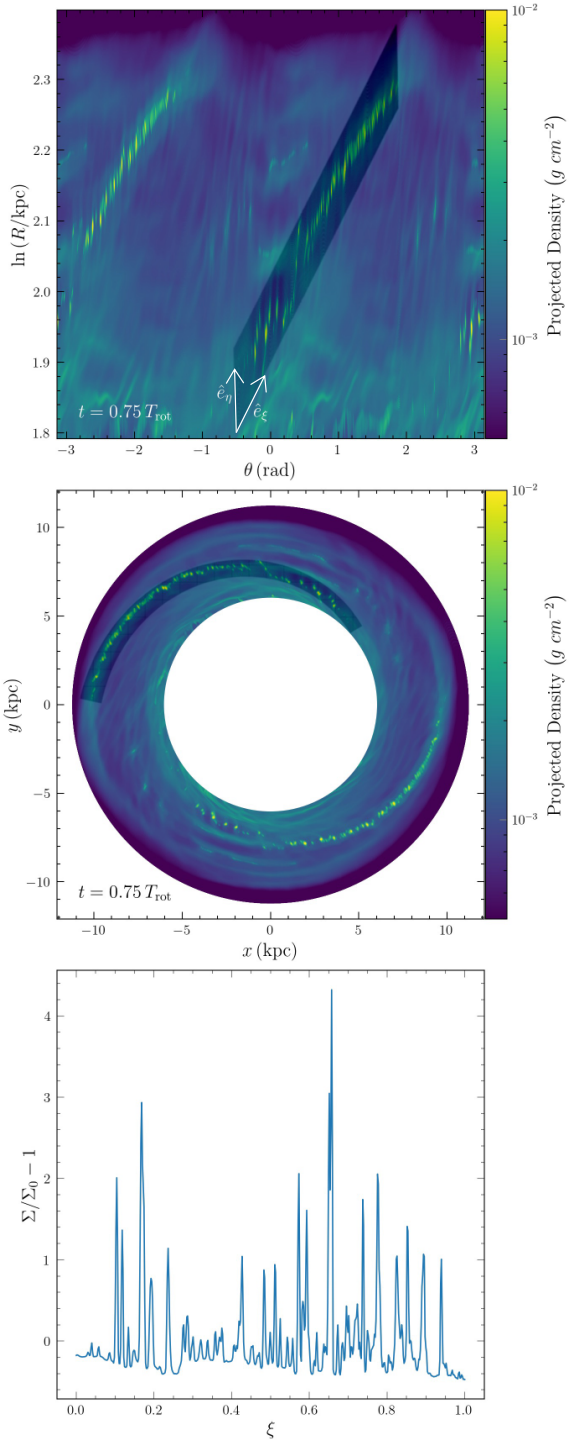

Fig. 4. The spiral arm mask overlaid on the column density of the disc galaxy. The first two panels show the spiral arm mask we used in the $(\ln R, \theta)$ plane and in the (x, y) plane, respectively. The first panel also shows the unit vectors $(\hat{e}_\xi, \hat{e}_\eta)$. The third panel shows the binned relative projected density $\Sigma/\Sigma_0 - 1$ along the arm. We can see the clumps as peaks in relative density in the third panel.

3.2.2. Cloud separation

We use the 1D power spectrum of the projected density derived in the last section to quantify the separation of the clouds in the spiral arms. We calculate the power spectrum at $t \in \{0.75\,T_{\rm rot}, 0.90\,T_{\rm rot}\}$ of one of the spiral arms as an example. These times correspond to the times shown in the bottom two panels of Fig. 2 and roughly indicate when the spiral arms are undergoing fragmentation and when the spiral arms separate into distinct clouds. The power spectrum for one of the arms is shown in Fig. 5, where the left panel shows the hydro run and the right panel the $\beta = 50$ case. The power on the vertical axis is plotted against the wave number k, which has units of $1/L_{\rm spiral}$, where $L_{\rm spiral}$ is the length of the spiral arm. We can see the rise in

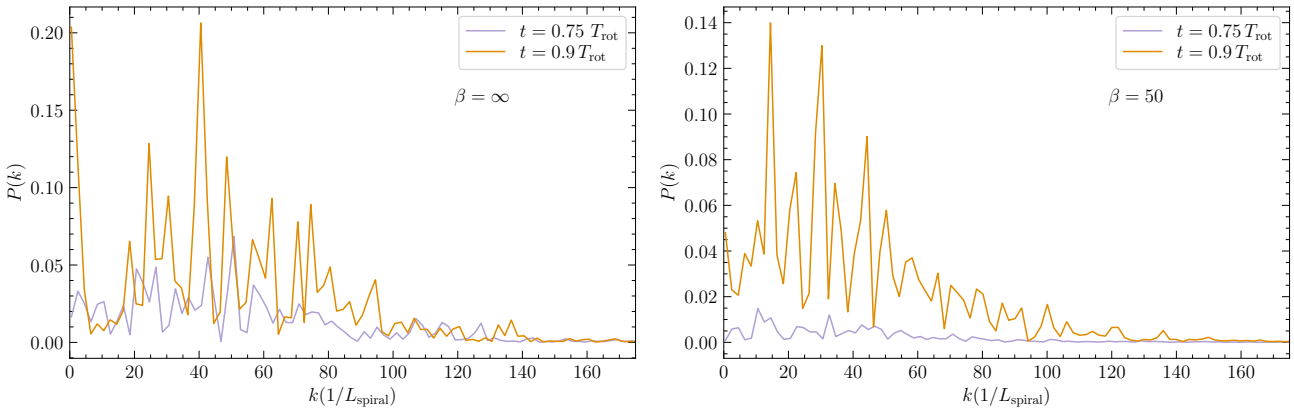

Fig. 5. Fourier transform of the projected density in the spiral arms for the $\beta = \infty$ and $\beta = 50$ runs. The two solid lines show the Fourier transforms at $t = 0.75, 0.90\,T_{\rm rot}$, analogous to the times shown in Fig. 1. The wave number k here is given in units of $1/L_{\rm spiral}$, i.e., $k = 1$ corresponds to the full length of the spiral arm under consideration. We can see that the $\beta = 50$ run has more power at lower k (larger scales) than the hydro run, as we visually saw in Fig. 2.

the power from $t = 0.75\,T_{\rm rot}$ to $t = 0.90\,T_{\rm rot}$ as the arm fragments and the clouds separate and become denser. This naturally produces a higher signal as the $\Sigma_{\rm sp,rel}$ grows and the spacing becomes more distinct. The hydro case has more power at early times than the $\beta = 50$ run, as expected, since it starts fragmenting $t \sim 20$ Myr earlier than the latter (cf. Fig. 3). At later times, $t = 0.9\,T_{\rm rot}$, we see distinct multiple peaks with similar power, where the majority of the power resides on larger scales with slight differences for both runs. For the hydro run, this is for $k \lesssim 80$ ($l \gtrsim 260$ pc), while for the magnetic case, we have $k \lesssim 50$ ($l \gtrsim 390$ pc).

The power spectrum also gives us insights into the regularity of the separation of the clouds in this particular arm. At $t = 0.90\,T_{\rm rot}$ the hydro run has a major peak at $k = 40$ ($l \sim 500$ pc). Similarly, in the $\beta = 50$ case, we see a major peak on larger scales at $k = 30$ ($l \sim 650$ pc). They both correspond to the total number of clouds we see in the respective arms. This signal in the Fourier analysis indicates that the adjacent separations of the clouds are regular. The magnetic case also has a major peak at $k = 14$ ($l \sim 1.4$ kpc), which corresponds to the number of brighter clouds along the spiral arm, as is also visible as the taller spikes in the bottom panel of Fig. 4.

An interesting feature in the Fourier transform common to both the runs is the presence of major peaks, which come in pairs of multiples of two. For example, we have $k \sim (24, 48)$, $(30, 60)$ and $(40, 80)$ in the hydro case and $k \sim (14, 30)$, $(22, 44)$ and $(34, 70)$ for the $\beta = 50$ case. This feature could be due to the combination of two reasons. The first is the physical presence of these modes due to the nature of the spiral arm instability, the second being the asymmetry in the negative and positive values in the function $\Sigma_{\rm sp,rel}[m] = \Sigma_{\rm sp}[m]/\bar{\Sigma}_{\rm sp} - 1$, of which we take the Fourier transform. In the latter case, we expect a single peak of the dominant mode followed by even harmonics with a decreasing power-law amplitude of the subsequent peaks. Looking at the lower panel of Fig. 4, we can see that the function $\Sigma/\Sigma_0 - 1$ is indeed asymmetrical. The voids between the clouds are not as under-dense as the clouds are over-dense. However, except for the dominant modes at low k, the higher k modes all have comparable amplitudes, and we therefore consider them to be physical modes in the system.

We test whether the differences observed in one of the spiral arms between the hydro and the magnetic cases can be generalised. For this, we run an identical pair of simulations for the hydro and $\beta = 50$ cases with a different random seed for the initial turbulence. We then also use both the spiral arms of each simulation in our analysis. As before, we calculate the power spectrum of the projected density along each of the arms. We show the peaks of the power spectrum in Fig. 6. Here, the error bars indicate the FWHM with a minimum value equal to the binning length $k = 2$ with respect to the physical scale in kpc on the horizontal axis. The left panel shows the hydro run and the right panel the $\beta = 50$ run. The different colours are for the runs with different initial turbulent seeds. The star and its error bars indicate the 50th (median) and the 16th to 84th percentile range after the points are binned in bins of 0.2 kpc.

We see from the Fig. 6 that the trends we observed in one of the spiral arms hold in the general case as well. The power in both cases exists on large scales, with the hydro run having major power over $l \gtrsim 300$ pc and the magnetic case having it on $l \gtrsim 400$ pc. We also see many significant peaks that are a multiple of 2 of a lower k mode in the magnetised and the hydro case. The rise in the cloud separation and unstable modes seen in the Fourier transform of one arm is also seen as a general trend of the presence of magnetic fields. Moreover, the power rises more steeply on small scales and also falls sharply after 1 kpc in the hydro case. For the magnetic field case, the rise in the power is shallower on smaller scales and spreads towards larger scales until 1.5 kpc. This is reflected in the percentiles of the distribution of the peaks, where the median and 16th to 64th percentile ranges of the hydro case rise from $0.73^{+0.31}_{-0.36}$ kpc to $0.98^{+0.49}_{-0.46}$ kpc in the magnetised case.

3.3. Effects of the magnetic fields on the physical properties of the spiral arms

As we have seen, the magnetic fields affect the evolution of the spiral arms, regardless of their strength. The magnetic fields themselves are also expected to evolve with the gas in our simulations. In order to gain insight into this, we explore the physical properties of the spiral arms in the three different runs with different initial magnetisation before they fragment or diffuse. We use one of the spiral arms in each simulation, since we find that they have very similar physical properties. As done in Fig. 2, we trace the gas in the spiral arm under consideration at $t = 0.5\,T_{\rm rot}$ using a friends-of-friends algorithm with a linking length of $l = 60$ pc, which is the approximate cell length of

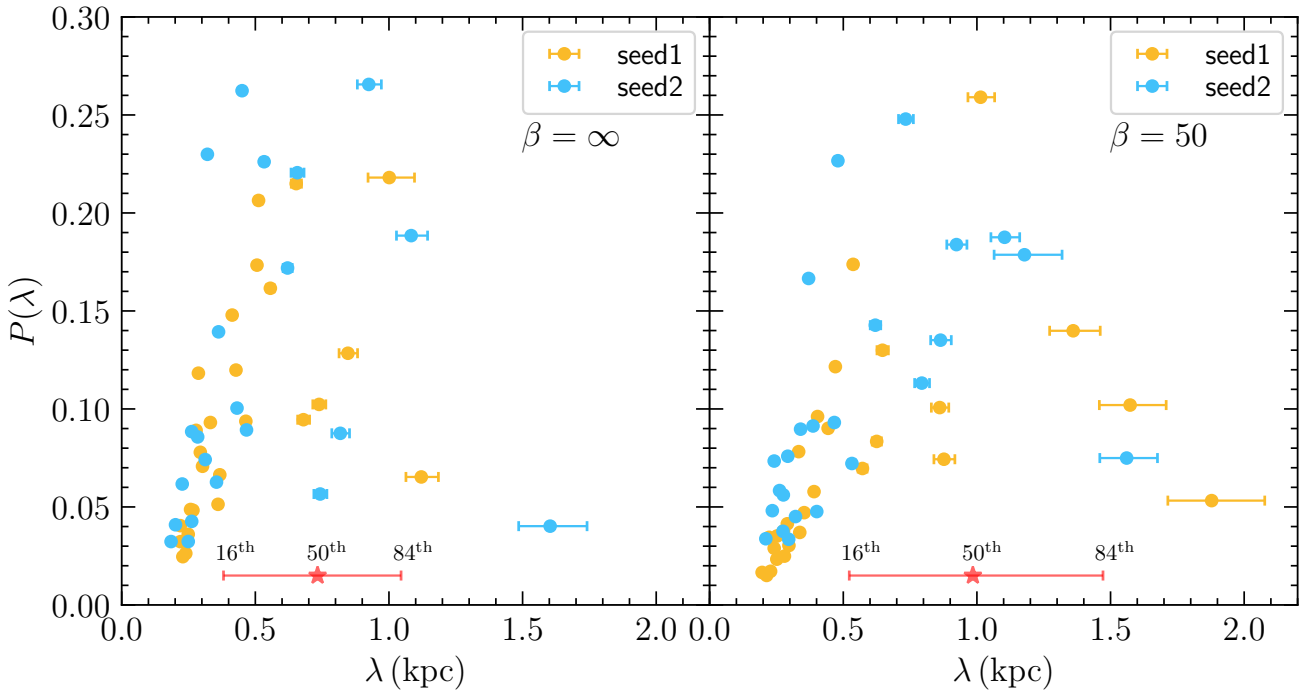

Fig. 6. Power ($P(\lambda)$) of the extracted peaks of the Fourier transforms of the projected density along the masked spiral arms plotted against the physical scale in kpc. The two panels show the hydro and the $\beta = 50$ cases at $t = 0.9\,T_{\rm rot}$. The two runs with different random seeds are shown in yellow and blue, respectively. In each case, we have included the peaks found for the two spiral arms. The star marks the 50th percentile, and the error bars indicate the range from 16th to 84th percentile of the peaks binned in 0.2 kpc bins. It increases from $0.73^{+0.31}_{-0.36}$ kpc in the hydro case to $0.98^{+0.49}_{-0.46}$ kpc in the magnetic case. However, peaks with the highest power in both the runs are present on length scales of ∼0.5−1.0 kpc.

the surrounding warm neutral medium around the spiral arms. In addition, we also use a density threshold of $n = 0.9\,{\rm cm}^{-3}$, which is similar to the critical density of the thermally unstable medium. The traced spiral arms are presented in Fig. 7, where we show the projected density of the three runs along with the traced spiral arms highlighted in a different colour scheme. We use these traced regions for all the properties we report in this section.

The total mass in the arms is similar, that is, $\log_{10}(M/(M_\odot) =$ 7.90, 7.85, and 7.71 for the hydro, $\beta = 50$, and $\beta = 10$ case, respectively. However, other physical properties vary systematically between them. We can see this in Fig. 8, where we show the mass-weighted probability density functions (PDFs) of the $\log_{10}$ of density in the left panel, the sound speed in the middle panel, and the cell-by-cell plasma-beta of the runs in the right panel. The stars in the histograms mark the average mass-weighted quantities in the respective vertical axis. In the left-most panel, as we saw in Sect. 3.1.2, we see that the spiral arms become more diffuse with increasing magnetisation. As seen in the mean density, which decreases by a factor of ∼2, possibly due to the additional opposing magnetic pressure. We find that the majority of the gas in the $\beta = 10$ case is present in the density range $\simeq$1−3 cm^{-3}, which is thermally unstable. Despite this, it never becomes denser because of the opposing magnetic pressure. We can also see this effect in the middle panel, where the gas in the hydro and the $\beta = 50$ cases have a lower sound speed than in the $\beta = 10$ case. This shows that the gas has already cooled in the former two cases, while it remains warm and close to its initial temperature in the latter. This is also reflected in the scale heights of the spiral arm, where the gas is found to be 50.2 ± 2.2 pc in the $\beta = 50$ case and 98.6 ± 3.9 pc in the $\beta = 10$ case. The details of the scale height calculation can be found in Appendix A. Thus the presence of magnetic fields largely causes the spiral arms to become more diffuse and hotter.

Interestingly, even though we start with a difference of a factor of 5 in the initial plasma-beta of the two magnetised runs, we note that they have similar values in the spiral arms. We see this in the right-most panel of Fig. 8, where the plasma-beta of the run with initial $\beta = 50$ has reduced by a factor of ∼25 to an average value of ∼2, and even has a non-negligible fraction of cells with values ≤1, where the magnetic fields dominate the gas pressure. The β in $\beta = 10$ run reduces by a factor of 5 to reach similar values as in the $\beta = 50$ case. This shows that the magnetic fields, even though not dynamically important at the beginning of the simulation, do become important later on in the spiral arms. This increase in field strength could be due to the combined effects of field tangling, adiabatic compression, and cooling or the presence of a dynamo (Federrath 2016). These effects are much more pronounced in the $\beta = 50$ case, where the gas compresses and cools in the absence of dynamically significant magnetic fields when compared to the $\beta = 10$ case, where they oppose compression and cooling. Thus, in the $\beta = 50$ case, we get magnetic fields that are dynamically significant after the spiral arms have become dense enough. This results in fragmentation in the presence of magnetic fields, and it changes the nature of the instability when compared with the hydro case. We discuss this in detail in the next section.

4. Discussion

Here, we discuss the physical effects of the magnetic fields on the spiral arm instability and compare them with previous theoretical and observational studies. First, we focus on the stabilising effect in Sect. 4.1, their destabilising effects in Sect. 4.2, and then go on

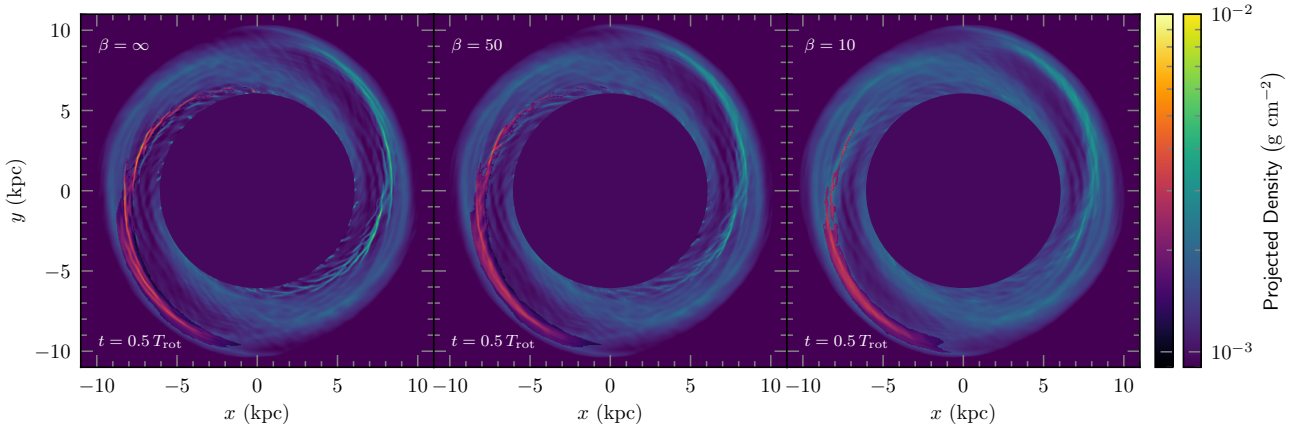

Fig. 7. Projected gas density of our models at $t = 0.5\,T_{\rm rot}$ along with the traced spiral arm highlighted with a different colour scheme. We can see that while the spiral arms in the hydro and $\beta = 50$ cases are morphologically similar to one another, there are noticeable differences with the $\beta = 10$ case.

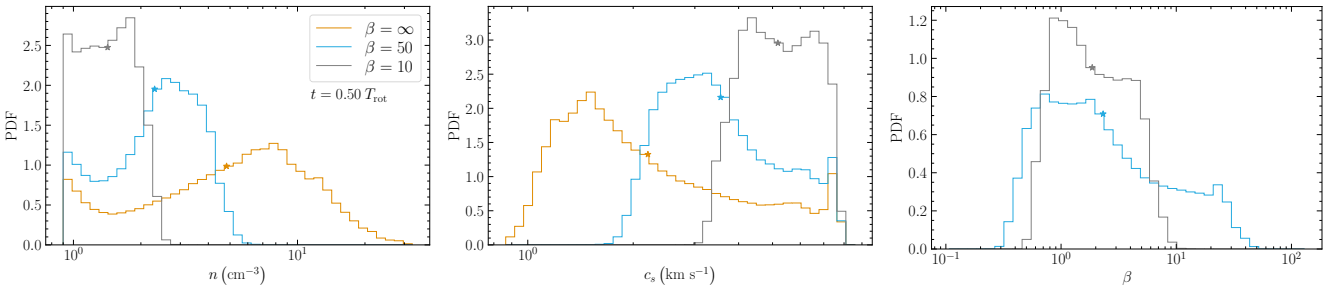

Fig. 8. Mass-weighted probability density functions (PDFs) of the $\log_{10}$ of the physical quantities of the gas in spiral arms. The left panel shows the gas density, the middle panel shows the sound speed and the right panel shows the cell-by-cell plasma-beta of the traced spiral arms at $t = 0.5\,T_{\rm rot}$. The stars mark the mass-weighted average of the $\log_{10}$ of the quantity in each case. In the left panel, we see that the spiral arms become more diffuse with increasing magnetisation. The middle panel shows that the gas becomes colder with increasing density as the cooling sets in. In the right panel we see that, the plasma-beta of the magnetic runs have decreased significantly in the arms (compared to the simulation starting value of β), especially for the $\beta = 50$ case, where the plasma-beta has risen from 50 to an average of 2.3, becoming comparable to the $\beta = 10$ case.

to discuss the cloud separation and unstable modes in Sect. 4.3. Lastly, we point out some caveats of our work in Sect. 4.4.

4.1. Stabilisation

We find that moderate initial magnetic fields with an initial $\beta = 10$ can stabilise the spiral arms against fragmentation. As seen in Fig. 8, the spiral arms that form in this case are more diffuse and hotter than in the other cases (hydro and $\beta = 50$ models), where they fragment. This is mainly due to the increased magnetic pressure of the B fields that prevents the gas from becoming any denser. This inhibition of compression due to the additional magnetic pressure agrees well with other global disc galaxy simulations (Dobbs & Price 2008; Khoperskov & Khrapov 2018; Körtgen et al. 2019). However, we note that our value of $\beta = 10$ for stabilisation is higher than the values observed in other studies, $\beta \leq 0.1$ (Dobbs & Price 2008) and $\beta \leq 1$ (Khoperskov & Khrapov 2018). As pointed out before, our models are initially gravitationally stable and also have low shear and a warm medium.

For weak magnetic fields, $\beta = 50$, even though the spiral arms fragment, they do so in a different morphological manner than in the hydro run. The KHI-like wiggles as seen in the hydro case (reported in Wada & Koda 2004; Wada 2008; Sormani et al. 2017; Mandowara et al. 2022) are absent in the weakly magnetised simulation because the magnetic field in the spiral arms becomes dynamically important, with $\beta_{\rm arm} \sim 2$, which then prevents the wiggles through magnetic tension. This stabilising effect of magnetic fields has indeed been reported for magnetic fields of near equipartition strengths in both global 2D (Shetty & Ostriker 2006) and local 3D simulations (Kim & Ostriker 2006).

4.2. Destabilisation

For the case with weak initial magnetisation, the magnetic fields rise to equipartition levels within the arm (cf. right panel of Fig. 8). However, instead of stabilising the arm, as we expect from the additional magnetic pressure, the arms still fragment. They do so by clearing out the gas within the arm into clouds ~20 Myr before the hydro case (cf. Sect. 3.1.2). We attribute this to the possible presence of the Parker instability within the spiral arms. The Parker instability (Parker 1966, 1967a,b, 1968a,b) arises in a magnetised plasma in a stratified medium similar to that of a disc galaxy. A fluid element with a low magnetic field over-density in the disc becomes more diffuse due to the added magnetic pressure and will tend to rise upwards. Since the medium is stratified, the fluid element looses more gas after rising to adjust to the decrease in the ambient pressure, thus becoming lighter and more unstable (Shukurov & Subramanian 2021). This eventually results in a characteristic magnetic field structure of regular hills and valleys above and below the galactic plane,

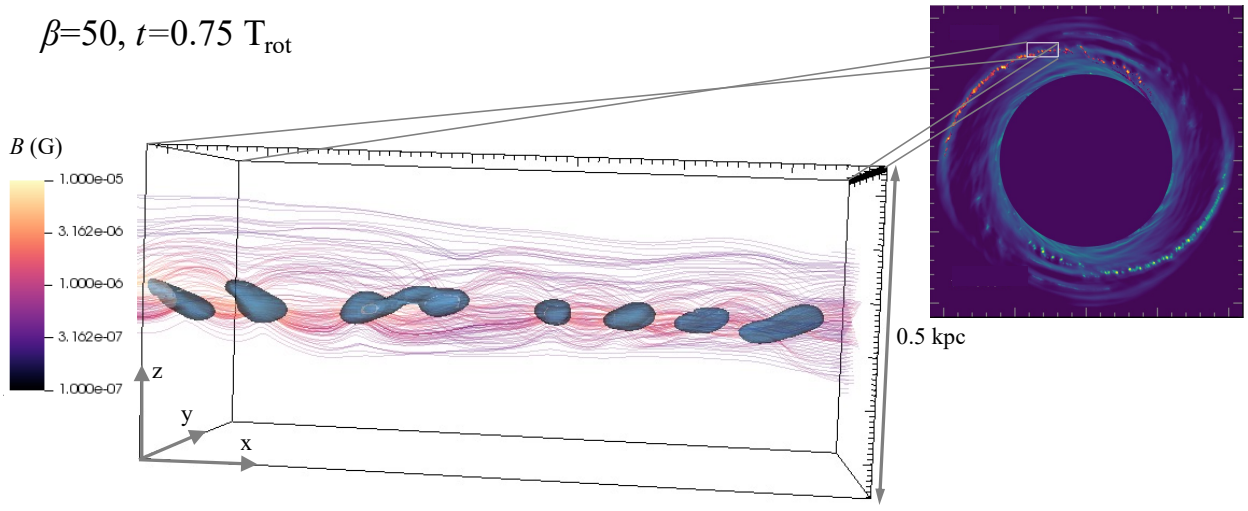

Fig. 9. Magnetic field lines in a section of one of the spiral arms for the $\beta = 50$ simulation at $t = 0.75\,T_{\rm rot}$. The magnetic field lines, coloured by their magnitude, were initialised on the right face (yz) of the region, in a circular plane of radius 250 pc, with its z-axis aligned with that of the clouds. The clouds are shown in blue iso-contours with a threshold density of about twice the critical density of the thermally unstable medium. We can see magnetic field loops rise above and below the plane of the clouds on scales of ∼100 pc. This is an indication that the Parker instability might play a role for the spiral arm stability.

where clouds are expected to form in the valleys of the magnetic field lines. In our simulations, we suspect that the initial magnetic over-densities are naturally provided by the spiral arms.

To test the presence of the Parker instability, we estimated the expected growth rates and the length scales from linear theory for the gas in the spiral arms before they fragment at $t = 0.50\,T_{\rm rot}$. Taking the average physical properties of the spiral arm presented in Sect. 3.3, with $c_{\rm s,arm} = 3.55\,{\rm cm\,s^{-1}}, \beta_{\rm arm} = 2.32$, $H_{\rm arm} = 50.2$ pc, and $\gamma_{\rm e} = 1$, we find an inverse growth rate of $\tau \simeq 33$ Myr, and the wavelength of the fastest growing mode ≃600 pc (cf. Eqs. (17) and (22) in Mouschovias 1996). As a result of the cooling in our simulations, the gas is also expected to cool in the valleys as it becomes denser (Kosiński & Hanasz 2006; Mouschovias et al. 2009). Along with self-gravity, this is expected to increase the growth rates of the instability, which makes both the length scales and time scales remarkably close to those we observe in the spiral arms. From Fig. 3, we can roughly estimate $\tau_{\rm arm} \sim 30$ Myr, and as we saw in Sect. 3.2, the cloud separation in the $\beta = 50$ runs is ≃650 pc.

In addition to this, we see the characteristic magnetic field morphology associated with the Parker instability in our spiral arms. A section of this characteristic field structure is shown at $t = 0.75\,T_{\rm rot}$ in Fig. 9. To produce this graph, we initialise the magnetic field lines at one yz face of the 3D box in a circular plane of radius 250 pc, coloured by the field strength. The clouds are solid iso-contours with a density of $2\,{\rm cm^{-3}}$, which is about twice the critical density of the thermally unstable medium. We can see the magnetic field lines rising above and below the plane of the spiral arm on scales of ∼100 pc. Since our thermally unstable medium is in the range $1-10\,{\rm cm^{-3}}$, the gas predominantly cools in the magnetic valley, as expected. Our results are in agreement with those of Mouschovias et al. (2009), who found that the Parker instability in unison with the thermal instability can lead to the formation of dense clouds in sections of spiral arms. We note here that the self-gravity, magnetic fields, and the thermal instability all act in synergy. The conditions are right for the Parker instability to play a role, but we cannot separate the non-linear interactions between the three in our simulations. In contrast to the $\beta = 50$ case, the seeds of the instability are never provided for the $\beta = 10$ case, since the spiral arms continue to disperse before they become dense enough to fragment when the field is too strong.

4.2.1. Comparison to observations

One nearby galaxy, NGC 628, was recently found to show evidence of magnetic Parker loops along one of its spiral arms in RM synthesis maps (Mulcahy et al. 2017). These loops are roughly coincident with the regularly spaced star-forming regions that were studied in Gusev & Efremov (2013). A similar pattern was reported in the NW arm of M 31, where the wavelength of the Parker loops, ∼2.3 kpc (Beck et al. 1989), was found to be twice the separation of the regularly spaced star-forming regions found along the arm (Efremov 2009, 2010). These are encouraging signs of the presence of the Parker instability. However, to draw firm conclusions, more detailed analyses of a wider sample of galaxies that exhibit this regular spacing of star-forming regions along their spiral arms is needed.

4.2.2. Comparison to simulations

Linear stability analysis and local 2D simulations have observed a reduction in the growth rate of the spiral instability by a factor of 4 in the presence of equipartition magnetic fields in comparison to the hydrodynamical case (Kim et al. 2014). This is in contrast to our results, where we see an increase in the growth rates. This discrepancy could be due to their 2D approximations, in which they did not capture the onset of the Parker instability, as observed in our simulations. Kim & Ostriker (2006) observed magnetic destabilisation in their local 3D simulations of the spiral shock fronts, but attributed it to the magneto-Jeans instability (MJI), as they did not observe the characteristic Parker loops. This is not the case in our simulations probably because the spiral arms separate into clouds when the arms are at considerably low densities ($n_{\rm av} \sim 5\,{\rm cm^{-3}}$). It was also argued later that the box size of Kim & Ostriker (2006) was insufficient perpendicular to

the plane of the disc to find the Parker modes (Mouschovias et al. 2009).

4.3. Cloud separation

4.3.1. Comparison to observations

Out of many others, only four spiral galaxies, namely NGC 628 (M 74), NGC 895, NGC 5474, NGC 6946, have been analysed in detail for the separation of the regularly spaced star-forming regions using a method similar to ours (Gusev & Efremov 2013; Gusev et al. 2022), where the spiral arm was parametrised in the $(\ln R, \theta)$ plane. It was found that adjacent star-forming regions in all four galaxies were either at a spacing of 350−500 pc and/or integer multiples (2−4) of this range. This range of separations is remarkably similar to what we find, that is, ≃500 pc in the hydro and ≃650 pc in the weakly magnetised run. This is despite the differences between the parameters of our models and these galaxies.

We found that the Fourier transform of the column density along the spiral arms exhibits peaks that are integer multiples of each other (cf. Fig. 5). This effect has also been reported in all the four galaxies mentioned here (cf. Gusev et al. 2022). Since we see this in both the hydro and the weakly magnetised cases, magnetic fields are probably not the main cause for this, as previously suggested in Efremov (2010). This intriguing trend is also reflected in the strings of HI super-clouds found in the Carina arm of the Milky Way, separated by 700 pc ± 100 pc, where more massive clouds are at about twice this separation (Park et al. 2023). To draw firm conclusions from the cloud separation themselves, however, we need to expand the parameter space and tune our models to different nearby galaxies. This will help us understand the dependence of the cloud separation on the global properties of the galaxy.

4.3.2. Comparison to simulations

Other numerical works have reported an increase in the cloud separation by a factor of 2 (in local 2D simulations by Kim et al. 2015) and 3 (in local 3D simulations by Kim & Ostriker 2006) in spiral arms in the presence of magnetic fields for plasma-beta values similar to ours. This is larger than what we find, that is, an increase by a factor of 1.3 in the adjacent cloud separation as well as in the average unstable mode along the spiral arms. This could be due to the limited number statistics of the clouds in their local simulation boxes ($\lesssim$10) or other limitations introduced by the local approximation, compared to global disc simulations.

4.4. Caveats

Since we focus on the effects of magnetic fields on the formation of clouds. For the sake of simplicity and computational costs, we do not include a star formation model or various feedback mechanisms, such as supernova feedback, ionising radiation, winds from massive stars, or cosmic rays. These processes might have an affect on the fragmentation process of the clouds and the structure of the spiral arms themselves. Models that include star formation and feedback will be considered in future studies. Moreover, we point out that our galaxy is isolated from its cosmological environment. Thus, we also neglect the physical effect due to fountain flows, accretion events, and mergers. Here, we focus solely on the effects of gas dynamics, which suggests that at least the onset of fragmentation of the spiral arms can be explained by self-gravity, cooling, and magnetic fields alone.

Our galaxies are gravitationally stable, have low shear (compared to the Milky Way), and initially are in the thermally stable regime. This is done to ensure that our galaxy is dominated by the spiral arms because we focus exclusively on the spiral arm instability.

5. Summary

We studied isolated spiral disc galaxies in global 3D simulations with self-gravity, magnetic fields, equilibrium heating and cooling, and an external spiral potential to study the impact of varying magnetic field strengths on the spiral arm instability. The spiral arms in our simulations form self-consistently and fragment into beads-on-a-string patterns. We found that the magnetic fields have a major dynamical impact on the spiral arm instability, which mainly depends upon their initial strength. Our conclusions are summarised below.

- For comparable spiral background potentials, moderate initial magnetic fields ($\beta = 10$) stabilise the spiral arms against fragmentation, in contrast to the hydro and weak-field case ($\beta = 50$), where the arms are unstable. The moderate magnetic field case forms arms that are more diffuse and hotter than in the other cases due to the additional opposing magnetic pressure.
- For the case of weak initial magnetic fields ($\beta = 50$), the spiral arms fragment in the presence of amplified equipartition magnetic fields in the arms ($\beta_{\rm arm} \sim 2.3$). The magnetic tension of the fields stabilises the vortical KHI-like wiggles in the hydro case.
- We estimate the adjacent cloud separations in the unmagnetised (hydro) case to be ∼500 pc, and ∼650 pc in the weakly magnetised case. This is remarkably close to the separations observed in many nearby spiral galaxies, which show separations of star-forming regions in the range 400−700 pc.
- The wavelength of the average unstable mode along the spiral arms increases in length from $0.73^{+0.31}_{-0.36}$ kpc in the hydro case, to $0.98^{+0.49}_{-0.46}$ kpc in the weakly magnetised case.
- Additionally, the peaks of the 1D Fourier power spectrum of the column density along the spiral arms show peaks that are integer multiples of each other for both the magnetic and un-magnetised cases. This has been reported for the nearby galaxies analysed for the regularity of star-forming regions along their spiral arms.
- The spiral arms in the weakly magnetised case separate into disjointed clouds along the arms around ∼20 Myr before the hydro case. We find indications that this may be due to the onset of the Parker instability in the spiral arms. The calculated linear growth rates and length scales of the Parker instability fall within the expected values seen in the simulation. We also showed the magnetic field morphology around the clouds in the arm that forms magnetic hills and valleys (cf. Fig. 9), as expected from linear theory.

With the advent of the *James Webb* Space Telescope, we can now resolve the infrared cores that are observed along the spiral arms of nearby galaxies (Elmegreen et al. 2006, 2018; Elmegreen & Elmegreen 2019) in unprecedented detail. Future parameter studies will aim to tailor our models to nearby galaxies for a more direct comparison with these observations.

Acknowledgements. The authors thank the anonymous referee for their constructive comments that have improved the clarity and quality of the paper. R.A. thanks Shivan Khullar and Chris Matzner for their time and insightful discussions. C.F. acknowledges funding provided by the Australian Research Council

(Future Fellowship FT180100495 and Discovery Project DP230102280), and the Australia-Germany Joint Research Cooperation Scheme (UA-DAAD). We further acknowledge high-performance computing resources provided by the Leibniz Rechenzentrum and the Gauss Centre for Supercomputing (grants pr32lo, pr48pi and GCS Large-scale project 10391), the Australian National Computational Infrastructure (grant ek9) and the Pawsey Supercomputing Centre (project pawsey0810) in the framework of the National Computational Merit Allocation Scheme and the ANU Merit Allocation Scheme. The simulation software, FLASH, was in part developed by the Flash Centre for Computational Science at the Department of Physics and Astronomy of the University of Rochester.

References

Beck, R. 2015, A&ARv, 24, 4
Beck, R., Loiseau, N., Hummel, E., et al. 1989, A&A, 222, 58
Beck, R., Chamandy, L., Elson, E., & Blackman, E. G. 2020, Galaxies, 8, 4
Binney, J., & Merrifield, M. 1998, Galactic Astronomy (Princeton: Princeton University Press)
Chakrabarti, S., Laughlin, G., & Shu, F. H. 2003, ApJ, 596, 220
Cox, D. P., & Gómez, G. C. 2002, ApJS, 142, 261
Dobbs, C. L., & Price, D. J. 2008, MNRAS, 383, 497
Dubey, A., Fisher, R., Graziani, C., et al. 2008, in Numerical Modeling of Space Plasma Flows, eds. N. V. Pogorelov, E. Audit, & G. P. Zank, ASP Conf. Ser., 385, 145
Efremov, Y. N. 2009, Astron. Lett., 35, 507
Efremov, Y. N. 2010, MNRAS, 405, 1531
Elmegreen, B. G., & Elmegreen, D. M. 1983, MNRAS, 203, 31
Elmegreen, B. G., & Elmegreen, D. M. 2019, ApJS, 245, 14
Elmegreen, D. M., Elmegreen, B. G., Kaufman, M., et al. 2006, ApJ, 642, 158
Elmegreen, B. G., Elmegreen, D. M., & Efremov, Y. N. 2018, ApJ, 863, 59
Federrath, C. 2016, J. Plasma Phys., 82, 535820601
Federrath, C., Roman-Duval, J., Klessen, R. S., Schmidt, W., & Mac Low, M. 2010, A&A, 512, A81
Federrath, C., Chabrier, G., Schober, J., et al. 2011, Phys. Rev. Lett., 107, 114504
Federrath, C., Roman-Duval, J., Klessen, R. S., Schmidt, W., & Mac Low, M. M. 2022, Astrophysics Source Code Library [record ascl:2204.001]
Fryxell, B., Olson, K., Ricker, P., et al. 2000, ApJS, 131, 273
Gusev, A. S., & Efremov, Y. N. 2013, MNRAS, 434, 313
Gusev, A. S., & Shimanovskaya, E. V. 2020, A&A, 640, L7
Gusev, A. S., Shimanovskaya, E. V., & Zaitseva, N. A. 2022, MNRAS, 514, 3953
Hanawa, T., & Kikuchi, D. 2012, in Numerical Modeling of Space Plasma Slows (ASTRONUM 2011), eds. N. V. Pogorelov, J. A. Font, E. Audit, & G. P. Zank, ASP Conf. Ser., 459, 310
Khoperskov, S. A., & Khrapov, S. S. 2018, A&A, 609, A104
Kim, W.-T., & Ostriker, E. C. 2006, ApJ, 646, 213
Kim, W.-T., Kim, Y., & Kim, J.-G. 2014, ApJ, 789, 68
Kim, Y., Kim, W.-T., & Elmegreen, B. G. 2015, ApJ, 809, 33
Kosiński, R., & Hanasz, M. 2006, MNRAS, 368, 759
Koyama, H., & Inutsuka, S.-I. 2002, ApJ, 564, L97
Körtgen, B., Banerjee, R., Pudritz, R. E., & Schmidt, W. 2018, MNRAS, 479, L40
Körtgen, B., Banerjee, R., Pudritz, R. E., & Schmidt, W. 2019, MNRAS, 489, 5004
Lee, W.-K. 2014, ApJ, 792, 122
Mandowara, Y., Sormani, M. C., Sobacchi, E., & Klessen, R. S. 2022, MNRAS, 513, 5052
Mouschovias, T. C. 1996, in The Parker Instability in the Interstellar Medium, ed. K. C. Tsinganos (Dordrecht: Springer), 475
Mouschovias, T. C., Kunz, M. W., & Christie, D. A. 2009, MNRAS, 397, 14
Mulcahy, D. D., Beck, R., & Heald, G. H. 2017, A&A, 600, A6
Nguyen, N. K., Pettitt, A. R., Tasker, E. J., & Okamoto, T. 2017, MNRAS, 475, 27
Park, G., Koo, B. C., Kim, K. T., & Elmegreen, B. 2023, ApJ, 955, 59
Parker, E. N. 1966, ApJ, 145, 811
Parker, E. N. 1967a, ApJ, 149, 517
Parker, E. N. 1967b, ApJ, 149, 535
Parker, E. N. 1968a, ApJ, 154, 49
Parker, E. N. 1968b, ApJ, 154, 57
Proshina, I. S., Moiseev, A. V., & Sil'chenko, O. K. 2022, Astron. Lett., 48, 139
Renaud, F., Bournaud, F., Emsellem, E., et al. 2013, MNRAS, 436, 1836
Roberts, W. W. 1969, ApJ, 158, 123
Shetty, R., & Ostriker, E. C. 2006, ApJ, 647, 997
Shukurov, A., & Subramanian, K. 2021, Astrophysical Magnetic Fields: From Galaxies to the Early Universe, Cambridge Astrophysics (Cambridge: Cambridge University Press)
Sormani, M. C., Sobacchi, E., Shore, S. N., Treß, R. G., & Klessen, R. S. 2017, MNRAS, 471, 2932
Truelove, J. K., Klein, R. I., McKee, C. F., et al. 1997, ApJ, 489, L179
Vázquez-Semadeni, E., Gómez, G. C., Jappsen, A. K., et al. 2007, ApJ, 657, 870
Wada, K. 2008, ApJ, 675, 188
Wada, K., & Koda, J. 2004, MNRAS, 349, 270

Appendix A: Scale height estimation

We estimate the scale height around the spiral arms by quantifying the density as a function of the z-coordinate, which is perpendicular to the plane of the galactic disc. We take the spiral arms traced via the friends-of-friends (FoF) algorithm (cf. Section 3.3). For each (x,y) in the arms, we define $z = 0$ as the point of maximum density. This ensures that we trace the spiral arms in three dimensions. We then bin the density in bins of 20 pc. This is shown in Figure A.1, where the density is plotted on the vertical axis and the z-coordinate on the horizontal axis. For the scale height calculation, we then fit the functional form $\rho(z) = \rho_0 \exp(-|z|/H)$ to the binned data. The fits are shown as dotted lines in Figure A.1. This gives us ρ_0 and the scale height H. The scale heights are found to be 50.2 ± 2.2 pc for the $\beta = 50$ case and 98.6 ± 3.9 pc for the $\beta = 10$ case.

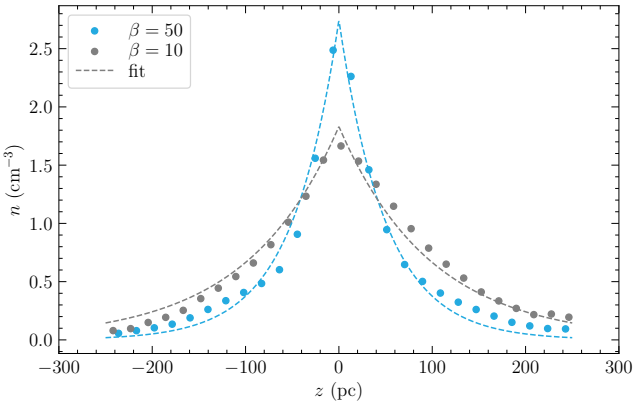

Fig. A.1. Gas density as a function of the z-coordinate around the traced spiral arms at $t = 0.50\,T_{\rm rot}$. The fit is of the functional form $\rho(z) = \rho_0 \exp(-|z|/H)$.

3 Paper II

Contribution

The idea was author's own. He developed the simulation setup, analysis pipeline and wrote the manuscript. Christoph Federrath, Mark Krumholz and Robi Banerjee held regular discussions, directed the progress, edited the manuscript and the referee report.

A&A, 695, A155 (2025)
https://doi.org/10.1051/0004-6361/202453501

Astronomy & Astrophysics

Formation of filaments and feathers in disc galaxies: Is self-gravity enough?

Raghav Arora[1,⋆], Christoph Federrath[2,3], Mark Krumholz[2], and Robi Banerjee[1]

[1] Hamburger Sternwarte, Universität Hamburg, Gojenbergsweg 112, 21029 Hamburg, Germany
[2] Research School of Astronomy and Astrophysics, The Australian National University, Canberra, ACT 2611, Australia
[3] Australian Research Council Centre of Excellence in All Sky Astrophysics (ASTRO3D), Canberra, ACT 2611, Australia

Received 18 December 2024 / Accepted 10 February 2025

ABSTRACT

Context. Dense filaments, also known as feathers, are kiloparsec-scale dusty features present in nearby main sequence galaxies. Distinct from the spiral arms, filaments constitute a major portion of dense gas concentration. They are expected to play an important role in star formation and are known to harbour embedded star-forming regions and H II regions.
Aims. We explore the origin of filaments and feathers in disc galaxies via global gravitational instability.
Methods. We conduct a parameter study using three-dimensional hydrodynamical simulations of isolated disc galaxies that are isothermal, self-gravitating and are initialised in equilibrium. Our galaxies are uniquely characterised by two dimensionless parameters, the Toomre Q and the rotational Mach number, $\mathcal{M}_c = v_c/c_s$ (ratio of circular velocity to sound speed). We carry out simulations covering a wide range in both parameters.
Results. We find that galaxies with $Q = 1$ form filaments within a single rotation, while galaxies with $Q \geq 2$ do not, even within a couple of rotations. These filaments are kiloparsec long and are semi-regularly spaced along the azimuth of the galaxy. Their morphology, density contrast and formation timescale vary with $\mathcal{M}_c$, with filament spacing and instability onset time both inversely proportional to $\mathcal{M}_c$ and the density contrast increasing with $\mathcal{M}_c$. However, filament growth rates in all $Q = 1$ galaxies are $\sim 0.5\,\Omega$, where Ω is the angular frequency. We compare the filament spacing in our simulations with the ones in JWST/Mid-Infrared Instrument and HST observations of nearby galaxies and find them to be in agreement.
Conclusions. Our study suggests that self-gravity and rotation alone are sufficient to form filaments and feathers, even in the absence of spiral arms or magnetic fields. The morphologies of the resulting filaments are determined primarily by $\mathcal{M}_c$, which parametrises the importance of thermal versus rotational support.

Key words. methods: numerical – ISM: structure – galaxies: evolution – galaxies: ISM – galaxies: star formation

1. Introduction

There has been mounting observational evidence in the past few years that star-forming disc galaxies harbour a complex, filamentary network of dense gas and dust (Thilker et al. 2023, and references therein). These are elongated, kiloparsec-scale, dense features known to host star-forming regions, H II regions and young star clusters (Schinnerer et al. 2017; Williams et al. 2022). Not only are they found in external galaxies, but there has also been evidence of such large-scale filamentary structures in the Milky Way (Zucker et al. 2015; Pantaleoni González et al. 2021; Kuhn et al. 2021; Veena et al. 2021). External galaxies, however, give us the advantage of the 'birds eye view', which allows us to study filament structure and morphology. Because of their richness in dust, they are visible as attenuation features in Hubble Space Telescope (HST) images (Elmegreen 1980; La Vigne et al. 2006), or as emission features in the near/mid-infrared, for example in the 8 μm infrared band of Spitzer (Elmegreen et al. 2006, 2014, 2018; Elmegreen & Elmegreen 2019) and in recent JWST/Mid-Infrared Instrument (MIRI) observations (Williams et al. 2022; Thilker et al. 2023; Meidt et al. 2023), which have reached unprecedented resolutions of ∼10 pc. This enables us for the first time to compare the detailed morphology of dense gas in simulations with observations of nearby galaxies and to test the theories for the origins of filamentary structures.

The question of their origin is far from settled, and a number of different mechanisms have been proposed. Filaments have been most commonly found in grand-design spiral galaxies, and within spirals most frequently in Sb-Sc galaxies (La Vigne et al. 2006). This increased detection frequency in grand-design spirals has led some authors to posit that filament formation is driven by spiral arms, and to carry out linear stability analyses and two-dimensional (2D) simulations showing that gas traversing arms created by an external spiral potential is prone to a hydrodynamical instability that causes them to develop over-densities, which are then sheared into filamentary structures in the inter-arm regions (Wada & Koda 2004; Dobbs & Bonnell 2006; Lee & Shu 2012; Kim et al. 2014; Lee 2014; Kim et al. 2015; Sormani et al. 2017; Mandowara et al. 2022). Other authors have attributed filaments to Parker instability driven by large-scale magnetic fields (Körtgen et al. 2019) or supernova feedback from star-forming regions in the arms (Kim et al. 2020). Yet other authors suggest that gas self-gravity alone could potentially create filamentary structures without the need to invoke external potentials, supernova feedback or magnetic fields (Griv & Gedalin 2012; Meidt 2022).

At present, however, we lack a systematic, 3D, global, numerical study that aims to disentangle the contribution of

⋆ Corresponding author; raghav.arora@uni-hamburg.de

different physical processes to dense structure formation in galaxies. Prior works that explicitly focus on gravitational instability in a galactic disc are either 2D (Shetty & Ostriker 2006; Griv & Wang 2014) or are low-resolution models with limited parameter space that were unable to resolve the spatial scales necessary for filament formation (Kim & Ostriker 2006; Wang et al. 2010). More recent and higher resolution simulations have different aims. Some are focused on studying Milky-Way analogues that have similar mid-plane pressures, distribution of the total mass into the halo, stellar bulge and the gas components as our own Galaxy (Kim et al. 2016; Jeffreson et al. 2020). Others include complex physical processes such as an external spiral potential and subgrid models for star formation and feedback that make it hard to separate effects of different physical processes (for example; Tress et al. 2020; Robinson & Wadsley 2024; Zhao et al. 2024; Khullar et al. 2024).

The aim for this study is to use numerical simulations to determine the conditions of filament formation in an idealised setting where we have control over the different potential drivers of filament formation and thereby can carry out clean numerical experiments to gain insight into the underlying physics. To this end, we carry out high-resolution 3D simulations of isothermal, self-gravitating isolated disc galaxies that are initialised in equilibrium. The main question we address is whether self-gravity by itself, in the absence of the other mechanisms described above (such as magnetic fields, stellar spiral potentials, supernovae), is sufficient to create the dense filamentary network observed in galaxies. We demonstrate that it is, and conduct a parameter study to quantify the morphological features of the filamentary structures that form in our simulations. Finally, we compare the physical spacing of the simulated filaments with recent observations.

The paper is organized as follows: Section 2 describes our simulation setup, initial conditions and the library of simulations used in this work. In Section 3, we discuss the basic morphology of our galaxies and the filaments that form in them. We further quantify the dependence of the morphology and filament formation timescales on the initial galaxy-wide parameters. In Section 4, we compare our results with observations and existing theoretical and numerical work. Finally, we summarise our conclusions in Section 5.

2. Methods

2.1. Physical setup

Our 3D disc galaxy simulations consist of self-gravitating isothermal gas in an analytical axisymmetric, time-steady dark matter plus stellar potential with a flat rotation curve. We initialise our disc galaxies in equilibrium using the "potential method" described by Wang et al. (2010). Here, we briefly describe the setup.

2.1.1. Basic setup

We seek to initialise our simulated galaxies in equilibrium, such that the forces due to thermal pressure, self-gravity, dark matter and rotation balance in both the radial and vertical directions. The surface density of the galaxies follows a modified exponential profile given by

$$\Sigma(R) = \Sigma_\circ \exp\left[-\frac{R}{R_\mathrm{d}} - \beta \exp\left(-\alpha \frac{R}{R_\mathrm{d}}\right)\right], \tag{1}$$

where R is the galactic (cylindrical) radius, $\Sigma_\circ$ is a scaling constant that will vary from run to run, $R_\mathrm{d} = 3$ kpc is the disc scale length, and $\alpha = 2$ and $\beta = 1/2$ are constants that determine the shape of the surface density profile near the centre of the galaxy. We use this function instead of the pure exponential in order to flatten the surface density profile close to the centre and guarantee that the scale height there is resolved well enough (≥4 cells) to avoid artificial numerical oscillations due to inadequate resolution of the vertical pressure gradient that balances self-gravity. Since we are not interested in the central part of the galaxy, this does not affect our results.

The rotation profile of the disc is given by

$$v_\mathrm{rot} = v_\mathrm{c} \frac{R}{\sqrt{R^2 + R_\mathrm{c}^2}}, \tag{2}$$

where v_c is the saturated circular velocity of the gas and $R_\mathrm{c} = 2$ kpc. The gas follows an isothermal equation of state with

$$P = \rho {c_\mathrm{s}}^2, \tag{3}$$

where P is the gas pressure, ρ is the density, and c_s is the sound speed.

We use the constraint of radial equilibrium to determine the stellar plus dark matter potential ϕ_dm. For the exact expression and details regarding the procedure, the reader is referred to Appendix A. We then use this to place the disc in vertical equilibrium, where we balance the force due to the gas self-gravity and the gravity due to the stellar and dark matter components with the vertical pressure gradient of the gaseous disc at each galactocentric radius,

$$\rho \frac{\partial}{\partial z}\left(\phi_\mathrm{g} + \phi_\mathrm{dm}\right) + {c_\mathrm{s}}^2 \frac{\partial \rho}{\partial z} = 0, \tag{4}$$

where ϕ_g is the gravitational potential of the self-gravitating gas (see Appendix A). This is subject to the constraint that

$$2 \int_0^\infty \rho(R, z)\, \mathrm{d}z = \Sigma(R), \tag{5}$$

where $\Sigma(R)$ is the surface density profile (Equation (1)). Since ϕ_g and ϕ_dm do not depend on ρ in our simple approximation, we can find a vertical profile $\rho(R, z)$ that satisfies these two constraints numerically. We do this by starting with an initial guess of the midplane density $\rho(R, 0)$ and integrating Equation (4) to obtain the profile $\rho(R, z)$, which is then rescaled by a constant factor in order to satisfy Equation (5). We point out that this is an approximate procedure rather than exact, since the gas gravitational potential ϕ_g should depend on ρ. However, we have found that the approximation is sufficiently accurate that our initial discs quickly relax to an exact equilibrium.

Finally, we immerse our galactic discs in a uniform hot circum-galatic medium (CGM) with a constant $T_\mathrm{CGM} = 10^7$ K and density. We transition from the cold galactic disc to the hot CGM when our discs reach a fixed transition density of $\rho = 10^{-28}\,\mathrm{cm}^{-3}$, which is ∼5 orders of magnitude less than the central density of our models. The density of the CGM is such that there is no pressure gradient between the two media.

2.1.2. Turbulent velocity field

The rotation curve (Equation (2)) gives the mean initial velocity of the gas, but we also impose a perturbation on top of this to seed the instabilities that we strive to study. Our procedure for

doing so mirrors that described in Arora et al. (2024): we impose a turbulent initial velocity field with a sonic Mach number $\mathcal{M} = 0.5$ and a Kolmogorov scaling of $k^{-5/3}$ on scales [50, 200] pc. These are close to the driving scales of turbulence of $\sim$140 $\pm$ 80 pc estimated in the Milky Way (Chepurnov et al. 2010). The turbulent velocity field contains a natural mixture of solenoidal and compressible modes, and we generate it with the methods described in Federrath et al. (2010), using the publicly available TurbGen code (Federrath et al. 2022).

2.2. Parameter study

We characterise our disc galaxies with two dimensionless parameters,

$$\langle Q \rangle = \frac{1}{R_{\rm max}} \int_0^{R_{\rm max}} Q(R)\,{\rm d}R = \frac{1}{R_{\rm max}} \int_0^{R_{\rm max}} \frac{\kappa c_{\rm s}}{\pi G \Sigma}\,{\rm d}R, \tag{6}$$

$$\mathcal{M}_{\rm c} = \frac{v_c}{c_{\rm s}}, \tag{7}$$

where κ is the epicyclic frequency given by $\kappa^2 = 4\Omega^2 + 2R\Omega({\rm d}\Omega/{\rm d}R)$, $\Omega = v_{\rm rot}/r$ is the angular frequency, and we take $R_{\rm max} = 8$ kpc. The first parameter above is the mean value of the Toomre-Q parameter $Q(R)$ (Toomre 1964) over the inner 8 kpc of the galaxy; it quantifies the gravitational stability of our galaxies. The second parameter describes the ratio of rotation speed to sound speed in the region $R \gg R_{\rm c}$ where the rotation curve reaches its full speed; it relates to the rotational and thermodynamic properties of the galaxy and controls its thickness[1]. We show in Appendix B that these two dimensionless parameters, along with the auxiliary dimensionless ratios $R_{\rm max}/R_{\rm d}$, $R_{\rm c}/R_{\rm d}$, α, β, and q that we do not vary, fully determine both the initial state and the subsequent evolution of the system. In particular, we note that disc thickness is not an independent parameter, but is instead fully determined by $\langle Q \rangle$ and $\mathcal{M}_{\rm c}$ – primarily the latter.

The parameter space of our simulations can be split into two main groups. The first group varies Toomre-Q with $\langle Q \rangle \simeq \{1, 2, 3\}$. (The precise values are not exactly 1, 2, and 3, and are given in Table 1.) We show the radial profiles of $Q(R)$ for these three cases in Figure 1. The solid lines show Q at the specified galactocentric radius and the dot-dashed lines indicate the average $\langle Q \rangle$ in the region $0 \le R/{\rm kpc} \le 8$. The second group has constant $\langle Q \rangle = 1$, but varies $\mathcal{M}_{\rm c}$ with $\mathcal{M}_{\rm c} \simeq \{14, 21, 29, 36\}$; in terms of dimensional parameters, we do this by varying $v_{\rm c}$ while keeping $c_{\rm s} = 7$ km s^{-1} fixed. The range of $v_{\rm c}$ is chosen to reflect the range of rotation speeds observed in galaxies, with $v_{\rm c} \in \{100, 150, 200, 250\}$ km s^{-1} (Levy et al. 2018; Lang et al. 2020). Our full parameter space is summarised in Table 1. For the sake of brevity, we refer to the different runs using the rounded-off values of the dimensionless parameters in the rest of the work.

2.3. Numerical methods

We use the FLASH hydrodynamical code for performing the simulations (Fryxell et al. 2000; Dubey et al. 2008). The disc is initialised at the centre of a cuboidal box with side length $L_{\rm x} = L_{\rm y} =$ 20 kpc in the plane of the disc and $L_{\rm z} = 2.5$ kpc in the direction perpendicular to it. We use outflow boundary conditions as in earlier works (Körtgen et al. 2019; Arora et al. 2024), but the region we use for our analysis is limited to $2 \le R\,({\rm kpc}) \le 4$ and $H \le 250$ pc for our thickest galaxy, far enough from the edges of our box that the boundaries have negligible effects.

We use adaptive mesh refinement (AMR) for our simulations. Our base grid is $256 \times 256 \times 32$ cells, giving a cell size $\approx$80 pc. However, we achieve a maximum effective resolution of $4096 \times 4096 \times 512$, cells corresponding to a minimum cell size of $\approx$4.8 pc, by adding 4 additional levels of refinement. We apply this extra refinement to the same geometric region in all the simulations: a cylinder whose centre coincides with the centre of the galaxy and with radius $R_{\rm cyl} = 6$ kpc and half-height $|H_{\rm cyl}| = 100$ pc centred on the galactic plane. This ensures that all the simulations have identical spatial resolutions. For our thinnest disc, at this resolution we have $\ge$4 cells per galactic scale height at galactic centre, and $\ge$8 cells per scale height for our region of interest. Outside the cylindrical region where we enforce the highest refinement level, we refine and coarsen based on the condition that the Jeans length be resolved by at least 32 and not more than 64 grid cells (Federrath et al. 2011).

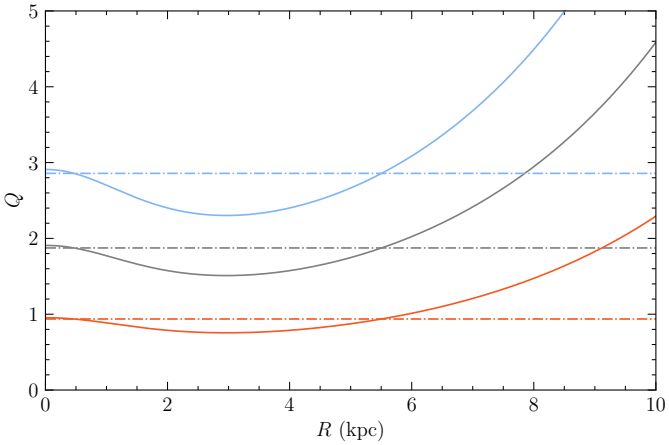

Fig. 1. Initial radial Toomre-Q (see Equation (6)) profiles of our galaxies. The solid lines show Q as a function of galactocentric radius and the dot-dashed lines show $\langle Q \rangle$, the average of the solid curves over the disc region $0 \le R/{\rm kpc} \le 8$.

Table 1. Parameter space of our simulations.

	Model name	$\langle Q \rangle$	$\mathcal{M}_{\rm c}$	$v_{\rm c}$ (km s^{-1})	$c_{\rm s}$ (km s^{-1})	$\Sigma_\circ$ (M$_\odot$ pc^{-2})
1	$Q1\_\mathcal{M}36$	0.94	35.7	250	7	224
2	$Q1\_\mathcal{M}29$	0.94	28.6	200	7	179
3	$Q1\_\mathcal{M}21$	0.94	21.4	150	7	134
4	$Q1\_\mathcal{M}14$	0.94	14.3	100	7	89.5
5	$Q2\_\mathcal{M}29$	1.87	28.6	200	7	89.5
6	$Q3\_\mathcal{M}29$	2.86	28.6	200	7	58.4

Notes. The value of Q used to parameterise the simulations is the radial average of the initial analytical profile from $R = 0$ kpc to $R = 8$ kpc.

3. Results

3.1. Disc morphology

We begin our analysis by showing the time evolution of one example run, $Q1\_\mathcal{M}29$ (that is, $\langle Q \rangle \simeq 1$ and $\mathcal{M}_{\rm c} = 29$), in

[1] Our $\mathcal{M}_{\rm c}$ parameter is similar to the quantity $v_{\rm c}/\sigma$ used in studies of galaxy kinematics to distinguish rotation-dominated from dispersion-dominated galaxies. Note that these are not fully identical since in observations σ contains both thermal and non-thermal contributions to the velocity dispersion. By contrast, for $\mathcal{M}_{\rm c}$ our dispersion is purely thermal.

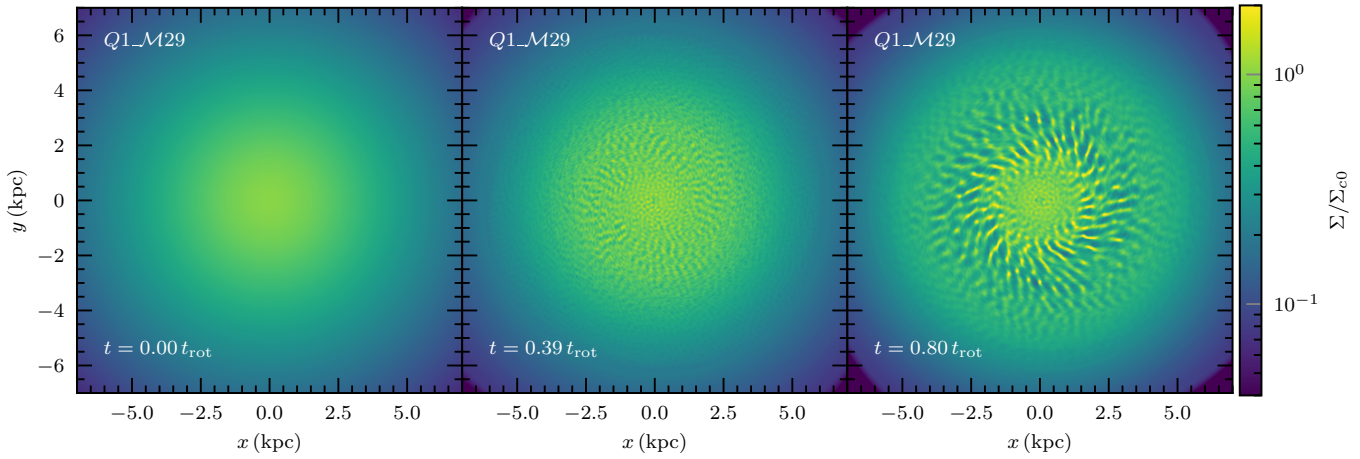

Fig. 2. Projected density of the $Q1\_\mathcal{M}29$ model in the z-plane. The projected density is normalised by the initial central projected density of the galaxy, shown at 0, 0.4, and 0.8 rotational times ($t_{\rm rot}$), from left to right. We see the gradual emergence of filamentary structures around R = 2–4 kpc.

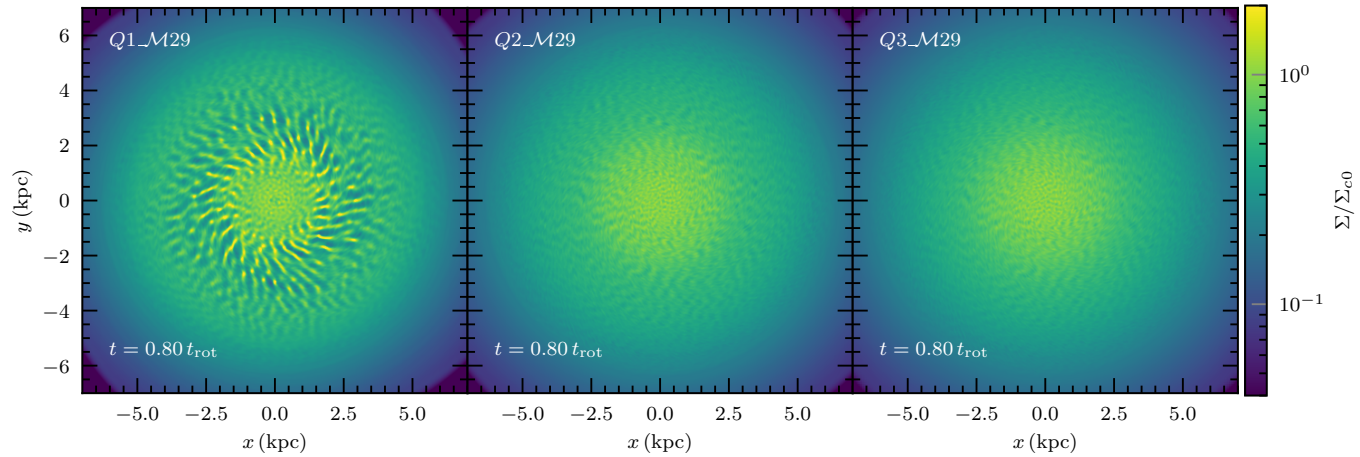

Fig. 3. Same as Figure 2, but for runs with $\langle Q\rangle$ = 1, 2, 3 (from left to right) at $t = 0.8\,t_{\rm rot}$. We see that the filamentary structures only emerge for the $\langle Q\rangle$ = 1 run.

Figure 2. Each panel depicts a time snapshot of the projected density of the disc in the z-plane. Time is expressed in units of $t_{\rm rot} = 2\pi R/v_{\rm rot}$, calculated at $R = 3$ kpc, increasing from left to right. The colourbar is normalised to the initial central surface density of the disc, that is, $\Sigma_{c0} = \Sigma(R = 0, t = 0)$. Following the evolution of the galaxy, we can see that it forms dense structures in less than one rotation period. These structures are ∼ kiloparsec long, uniformly spaced in azimuth, and pitched back as a result of differential rotation. For reference, we will refer to these structures interchangeably as feathers or filaments for the rest of the work. They are most prominent at radii $R \sim$ 2–4 kpc, which Figure 1 shows is the region of maximum Toomre instability, where Q dips well below unity. These features develop even in the absence of magnetic fields, spiral arms or feedback from stars, establishing that self-gravity alone is sufficient to produce them.

Interestingly, we do not see the development of feathers in the region $R \leq 2$ kpc (at least up to the time we have run the simulations) even though it also has values of $Q \leq 1$. One possible explanation for why not is the difference in the amount of shear in the rotation curve at these smaller radii. We can quantify this through the shear parameter $q = -(\mathrm{d}\ln\Omega/\mathrm{d}\ln R)$, which is equal to zero for solid body rotation and one for a flat rotation curve. The value of q only rises to a value of 0.5 at $R = R_{\rm c} = 2$ kpc, and thus the lack of feathers at smaller radii is potentially a result of the low shear in this region.

3.1.1. Dependence on $\langle Q\rangle$

We next examine the dependence of feather formation on the initial $\langle Q\rangle$. Similar to Figure 2, we show the z projections of disc density in Figure 3 for the $\langle Q\rangle$ = 1, 2, 3 (from left to right) runs at fixed $\mathcal{M}_{\rm c} = 29$ at identical times $t = 0.80\,t_{\rm rot}$. We can immediately see the stark difference between the run with $\langle Q\rangle = 1$ and the ones that have a higher $\langle Q\rangle$. For $\langle Q\rangle \in \{2, 3\}$, we see diffuse and faint structures in the disc. This is in contrast to the dense network of filaments that emerge in the $\langle Q\rangle = 1$ simulation. We do see development of dense features in the $\langle Q\rangle = 2$ run at times later than that shown in the Figure, but the rate of growth of this run is an order of magnitude slower than the $\langle Q\rangle = 1$ run, and thus it does not reach significant density contrasts until much later than the other runs. We discuss this case further in Appendix C, and for the remainder of the main body of this paper we exclusively focus on the $\langle Q\rangle = 1$ runs that form dense structures within a single rotation.

3.1.2. Dependence on $\mathcal{M}_c$

We now examine the runs with $\langle Q \rangle = 1$ but varying $\mathcal{M}_c$. Figure 4 is similar to Figure 3 in that it shows the z projections of the disc density for different runs, but in this case with a common value of $\langle Q \rangle = 1$ but varying $\mathcal{M}_c \in \{14, 21, 29, 36\}$. All runs shown are at time $t = 0.8\, t_{\rm rot}$ except for the $\mathcal{M}36$ run, which we show at $t = 0.54\, t_{\rm rot}$ because it evolves faster than the other cases and collapses beyond our ability to resolve by $0.8\, t_{\rm rot}$. We see that all the runs form filaments, but that there is a systematic and striking change of feather morphology between the panels. With increasing $\mathcal{M}_c$, the feathers are thinner and more closely-spaced. The $\mathcal{M}_c = 29$ and 36 cases also exhibit formation of dense clumps, in contrast to the $\mathcal{M}_c = 14$ and 21 runs where we see uniform larger-scale radially extended filaments.

The filaments we see in Figure 4 are comparable to the dense filamentary network observed in nearby spiral galaxies with JWST/MIRI observations (Thilker et al. 2023; Meidt et al. 2023) and the lattice or elongated extinction features reported in HST observations (La Vigne et al. 2006). In addition to the lattice-like morphology, where the filaments are present throughout the azimuth of the galaxy, the $\mathcal{M}_c = 36$ case has the filaments arranged in the pattern of spiral arms. This arrangement of filaments is similar to "spurs" (see La Vigne et al. 2006) that are filamentary features connected to spiral lanes. A notable feature of spurs is that they emanate from spiral arms whose pitch angles are lower compared to the pitch angle of spurs. This is also reproduced in the $\mathcal{M}_c = 36$ case. We defer a more quantitative comparison to observations to Section 4.2.

3.2. Feather formation timescales

After establishing that the galaxies with $\langle Q \rangle = 1$ forms feathers, we now quantify the timescales of their formation. For this purpose we define the logarithmic surface density,

$$\eta = \ln\left(\frac{\Sigma}{\langle \Sigma \rangle}\right), \tag{8}$$

where $\langle \Sigma \rangle$ is the average surface density of some region of interest. We take our region of interest for this purpose to be an annulus 1 kpc thick centred at $R = 3$ kpc, which is the region where feathers appear (as seen in Figure 4). We use the logarithmic surface density in order to give equal weight to the under- and over-dense regions that differ by a similar factor relative to the average. The variance in the value of η over the region of interest, which we denote σ_η, therefore describes the strength of density variations in that region. We show the time evolution of this quantity in Figure 5. The left panel is for runs with varying $\langle Q \rangle$ and constant $\mathcal{M}_c = 29$, while the right panel is for the group with $\langle Q \rangle = 1$ but varying $\mathcal{M}_c$. The solid lines in both the panels depict the data from the simulations and the dashed lines in the second panel are empirical fits to the data that we describe below.

Starting with the left panel in Figure 5 which shows runs with varying $\langle Q \rangle$, we see that the variation in the clumping factor rises initially due to the turbulent velocity field causing fluctuations in the density field, and that this rise is similar in all runs. After this initial rise the value of σ_η stabilises, but at this point the runs begin to diverge. In the $\langle Q \rangle = 1$ run the variations begin to rise again after a short stagnation period, marking the onset of instability. By contrast the runs with $\langle Q \rangle = 2$, 3 show gradual decline followed by a phase of slow growth after around a rotation period – see Appendix C for further discussion of the long-time behaviour of the $\langle Q \rangle = 2$ run. For the group of runs with $\langle Q \rangle = 1$ but different $\mathcal{M}_c$ (right panel), we see an evolution similar to the $Q1\_\mathcal{M}29$ case for all but one of the runs. That is, an initial jump, followed by a period during which σ_η remains roughly constant, and then an epoch of exponential growth. The $\mathcal{M}_c = 14$ differs slightly from this pattern, showing a dip in the midst of its steady period before recovering and then embarking on exponential growth.

While the runs show similar qualitative behaviour, there are quantitative differences. First, we see that the disc develops stronger density fluctuations (higher σ_η) with increasing $\mathcal{M}_c$, despite the initial velocity perturbations being unchanged. Second, the exponential growth phase of the instability is systematically earlier for increasing $\mathcal{M}_c$. Third, the slopes of the rising curves are higher with increasing $\mathcal{M}_c$. We quantify these trends by carrying out a simple χ^2 fit for the time-evolution of σ_η at times $t \geq 0.15\, t_{\rm rot}$, which is approximately the time of the initial relaxation phase, to an empirically-motivated piecewise function of the form

$$\sigma_\eta(t) = \begin{cases} A e^{\omega t_{\rm onset}} & t \leq t_{\rm onset}, \\ A e^{\omega t} & t > t_{\rm onset}, \end{cases} \tag{9}$$

where A sets the amplitude of σ_η during the steady phase and ω and $t_{\rm onset}$ quantify the growth rate and the time of the onset of the instability, respectively. We report the best-fitting parameters and their uncertainties in Table 2 and plot the fits as the dashed lines in the right-hand panel of Figure 5; the figure demonstrates that these functional forms fit the data very well, particularly in the time after $t_{\rm onset}$. We do not fit for the $\mathcal{M}_c = 14$ run since it shows a more complex behaviour compared to the other three runs.

For our best fits, we find $t_{\rm onset} \propto \mathcal{M}_c^{-1}$ to within 5%. Compared to this dependence of the onset time, we find that the growth rate only weakly depends on $\mathcal{M}_c$, with the highest growth rate $\omega = 3.06 \pm 0.08\, {t_{\rm rot}}^{-1} = 0.49 \pm 0.01\, \Omega$ for the $\mathcal{M}_c = 36$ case and the slowest growth rate $\omega = 2.41 \pm 0.04\, {t_{\rm rot}}^{-1} = 0.38 \pm 0.01\, \Omega$ for the $\mathcal{M}_c = 21$ run. A decrease in the growth rate is expected as the galaxy gets thicker since the gravitational potential is smeared out in the thick disc case when compared to the thin disc case of equal Q value (Meidt 2022). To check the robustness of this result against resolution, we carry out a resolution study on the $Q1\_\mathcal{M}29$ run, which we discuss in Appendix D. The analysis there shows that the run is converged with respect to both the onset time of the instability and the growth rate.

Since the growth rate of density contrast depends on $\mathcal{M}_c$, it is natural to ask whether the difference in morphology visible in Figure 4 is solely the result of the instability being at different evolutionary stages. To answer this question in Figure 6 we again show projections of all the $\langle Q \rangle = 1$ runs, but now choosing times when the different runs are at a common value of $\log_{10} \sigma_\eta = -0.3$. The figure shows that, even though we are now examining comparable amplitudes of the instability, substantial morphological differences remain between the runs with differing $\mathcal{M}_c$. We quantify these morphological differences in the next subsection.

3.3. Feather geometry

In order to better visualise the morphology of the filamentary structures formed in our galaxies, we project the galaxy in the $(\ln R, \theta)$ plane, where R is the galactocentric radius in kpc and θ is the azimuth. This allows easy identification of spiral features, since spirals of the form $R = e^{\theta \tan \alpha}$ appear as straight lines of slope $\tan \alpha$ in the $(\ln R, \theta)$ plane. It also makes the azimuthal periodicity of the features more apparent to the eye. We show this

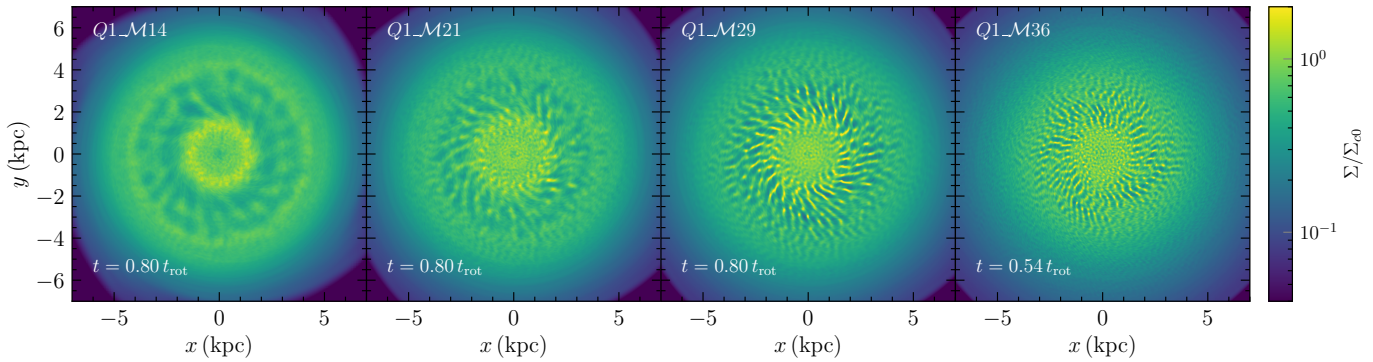

Fig. 4. Same as Figure 3, but for runs with $\mathcal{M}_c$ = 14, 21, 29, 36 (from left to right) and fixed $\langle Q \rangle$ = 1. All the discs are unstable to filament formation, but filament morphology differs starkly between the different runs, with higher $\mathcal{M}_c$ producing more and thinner filaments. The filaments also tend to be shorter at higher $\mathcal{M}_c$.

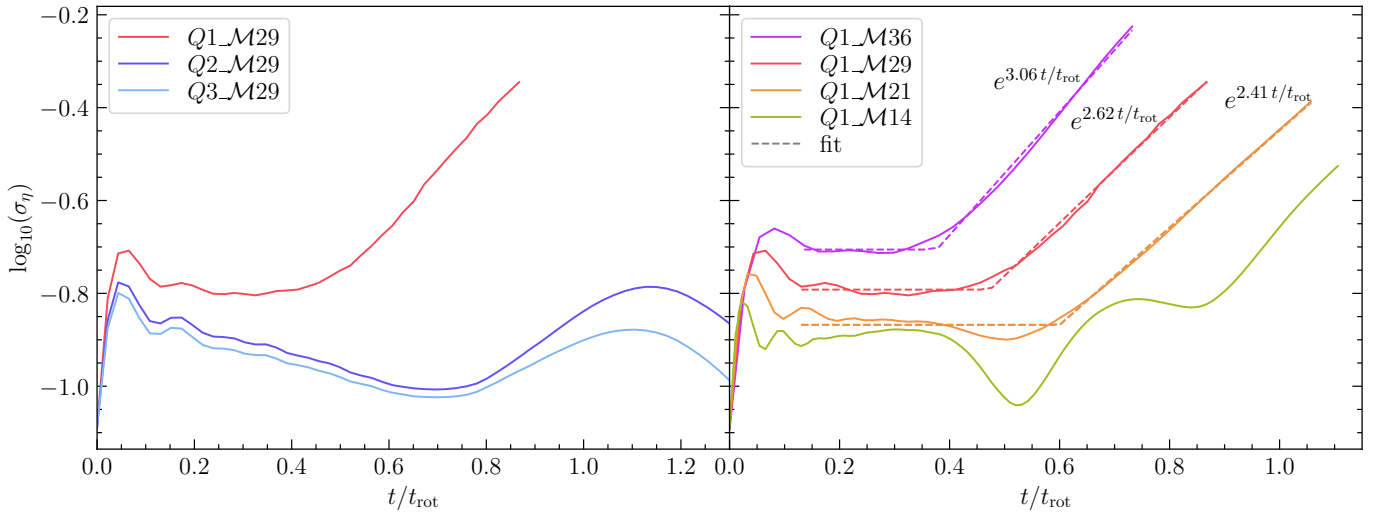

Fig. 5. Time evolution of the variance in the logarithmic surface density, σ_η, where η is defined in Equation 8. The panel on the left is for runs with varying $\langle Q \rangle$ and fixed $\mathcal{M}_c$ and the panel on the right for runs with varying $\mathcal{M}_c$ but fixed $\langle Q \rangle$, as indicated in the legends. The solid lines represent the simulation data and the dotted lines are piecewise fits with a constant and an exponential part. We see that the $\langle Q \rangle > 1$ runs are stable, while there is exponential growth in all the runs with $\langle Q \rangle$ = 1. For the unstable runs, we see that growth is faster for higher $\mathcal{M}_c$. We also observe a decrease in the time of the onset of the instability with increasing $\mathcal{M}_c$. We do not provide an analytical fit to the $\mathcal{M}_c$ = 14 case because of its complex behaviour.

Table 2. Fit parameters for the evolution of the variance in the logarithmic surface density σ_η (Equation (8)).

Model name	A	ωt_{rot}	t_{onset}/t_{rot}
$Q1\_\mathcal{M}21$	0.032 ± 0.001	2.41 ± 0.05	0.60 ± 0.01
$Q1\_\mathcal{M}29$	0.047 ± 0.001	2.62 ± 0.08	0.47 ± 0.01
$Q1\_\mathcal{M}36$	0.062 ± 0.002	3.06 ± 0.08	0.38 ± 0.01

Notes. The fit is performed using a functional form given by Equation 9. We show the best fits as dashed lines in the right-hand panel of Figure 5.

projection in Figure 6 for the same runs and times as in Figure 4. Since our galaxy rotates clockwise, the positively-sloped features visible in the plot correspond to trailing spiral features (tips pointing opposite to galactic rotation). We can immediately see that the feathers in the $\mathcal{M}_c$ = 14 and 21 runs appear as straight lines of nearly constant slope with a periodicity in the azimuthal direction. The complex morphology of the $\mathcal{M}_c$ = 29 and 36 runs appear as thinner spirals with a larger variation in their orientations and lengths compared to the $\mathcal{M}_c$ = 14 and 21 cases. In these runs we also see distinctive "spur"-like arrangements of the feathers located periodically along spirals, which are visible for example in the distinctive alternating pattern from $\theta \approx -1$ to 0 in the $\mathcal{M}_c$ = 36 run.

To quantify these morphological differences, we take "tilted" 2D Fourier transforms (Savchenko 2012; Puerari et al. 2014) of the windows shown in Figure 7. We define

$$A(m,p) = \int_{u_{min}}^{u_{max}} \int_0^{2\pi} \eta(\theta,u) e^{i(m\theta+pu)}\, \mathrm{d}\theta\, \mathrm{d}u, \tag{10}$$

where $u = \ln R$, η is the logarithmic surface density (defined in Equation (8)), and (u_{min}, u_{max}) denote the radial bounds of our annuli. The term $e^{i(m\theta+pu)}$ can be viewed as a filter function that picks up m-armed logarithmic spirals with a pitch angle of $\tan\alpha = -m/p$. We show the amplitude $|A(m,p)|$ normalised to the mean value $\bar{A}(m,p) = \iint A(m,p)\,\mathrm{d}m\,\mathrm{d}p / \iint \mathrm{d}m\,\mathrm{d}p$ in Figure 8, plotted with m on the abscissa and p on the ordinate. Different panels show runs with varying $\mathcal{M}_c$, increasing from left to right. We see that there is maximum in all the runs,

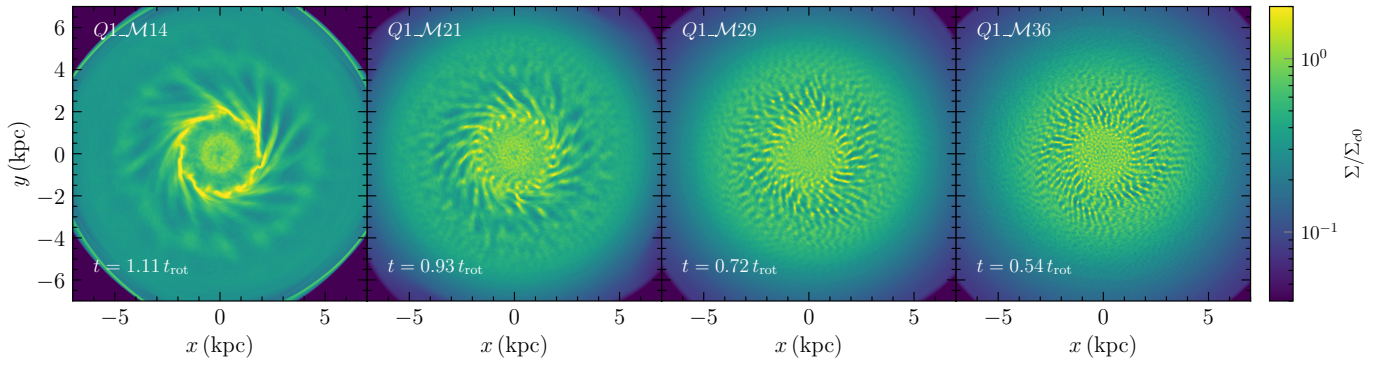

Fig. 6. Same as Figure 4, but now showing the different runs at different times. The time is chosen such that the standard deviation of the logarithmic surface density $\log_{10}\sigma_\eta = -0.3$ in all runs. We see systematic differences in the filament morphology even when the filament forming regions have similar density contrasts. The filaments are large scale and uniform in the $\mathcal{M}_c = 14$ and 21 runs compared to the more complex and finely spaced in the $\mathcal{M}_c = 29$ and 36 cases.

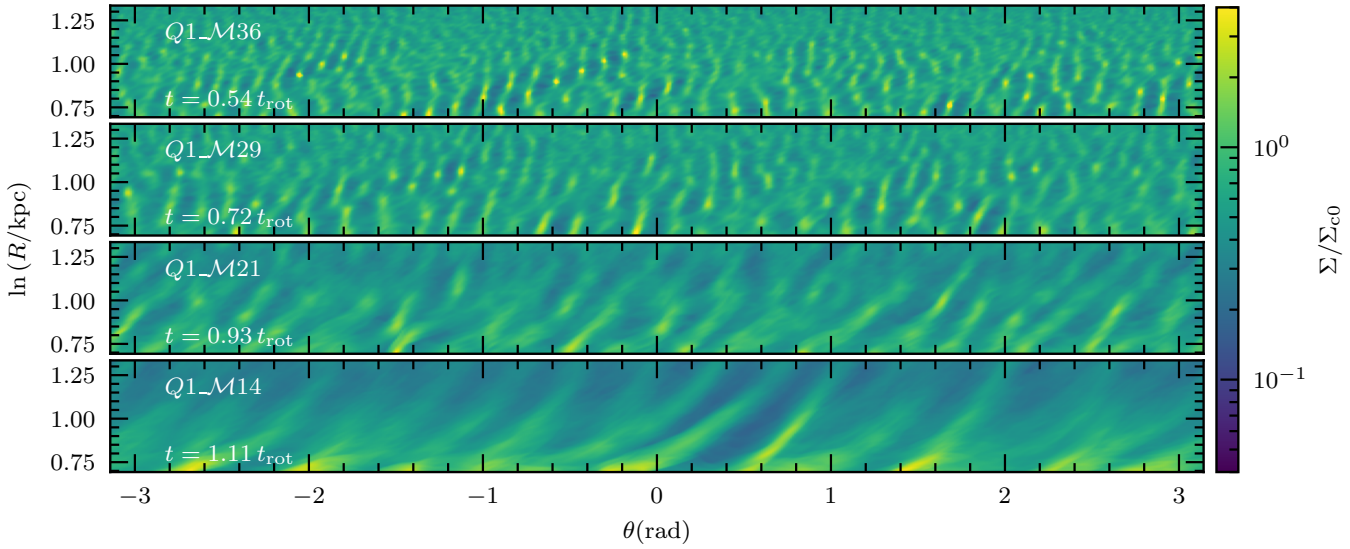

Fig. 7. Normalised surface density Σ/Σ_{c0} in the $(\ln R, \theta)$ plane for the same runs and times as shown in Figure 6. The radial range in this figure is chosen to highlight the annulus from 2–4 kpc where feather formation is strongest. We can see the feathers appear as sloped lines that are periodic in azimuth, with length, thickness, orientation and spacing that vary with $\mathcal{M}_c$. The associated time evolution movies are available online.

and from the position of this maximum we can read off the preferred azimuthal scale and orientation of the filaments. Shifts in the position of the maximum and the shape of the distribution around it reflect the morphological differences seen between the feathers of different runs. We see that as $\mathcal{M}_c$ increases, power shifts to higher m and more positive p, and that the distribution in the (m, p) plane broadens. These shifts mirror the more tightly packed and morphologically-complex filamentary pattern we see in going from low to high $\mathcal{M}_c$ in Figure 6.

3.3.1. Pitch angle

The 2D Fourier transform contains information on both the arm number and the pitch angle of the perturbations. To extract the latter we follow the approach of Savchenko (2012) by finding the m-mode of maximum power and then examining the range of p value, recalling that the pitch angle $\alpha = \tan^{-1}(-m/p)$. Quantitatively, for each simulation we define m_{max} as the value of m at which the maximum of $A(m, p)$ occurs. We then fit $A(m_{max}, p)$ with a Gaussian functional form in p, which provides a reasonably good description of the data. We demonstrate this in Figure 9, which shows $A(m_{max}, p)$ versus p, and our best Gaussian fits to it, for the same four snapshots shown in Figure 7.

We carry out this procedure for every snapshot of runs Q1_M14 to Q1_M36, extracting the amplitude A, mean μ, and dispersion σ of the best-fitting Gaussian at each time. We then take $\alpha = \tan^{-1}(-m_{max}/\mu)$ as our best estimate for the pitch angle. For the uncertainty in α, we take the dispersion of our fit as an estimate for the uncertainty in p, that is $\Delta p = \sigma$, and then propagate it to the uncertainty in pitch angle via standard error propagation, which gives

$$\Delta\alpha = \left|\frac{\mathrm{d}(\tan^{-1}(-m_{max}/p))}{\mathrm{d}(-m_{max}/p)}\Delta(-m_{max}/p)\right| = \left|\cos^2\alpha\frac{m_{max}}{\mu^2}\sigma\right|. \quad (11)$$

We show the pitch angle as a function of time after the onset of the instability that we derive from this procedure in Figure 10. The upper panel is for the $\mathcal{M}_c = 14$ and 21 runs and the lower panel for the $\mathcal{M}_c = 29$ and 36 cases. We see that, independent of $\mathcal{M}_c$, the average pitch angle of all the runs decreases with time. This is also seen visually in the time evolution movies of the surface densities in the $(\ln R, \theta)$ plane (available online). This is

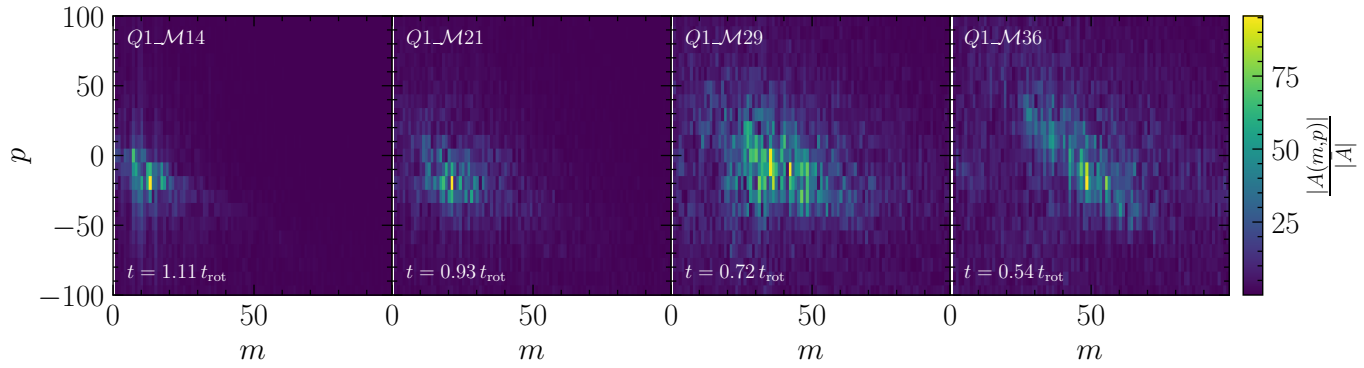

Fig. 8. Normalised amplitude of the 2D Fourier transform of the galactic annuli shown in Figure 7. Panels show runs with varying $\mathcal{M}_c$ (increasing from left to right). We can see that as $\mathcal{M}_c$ increases the maximum shifts to higher m and the width of the distribution increases.

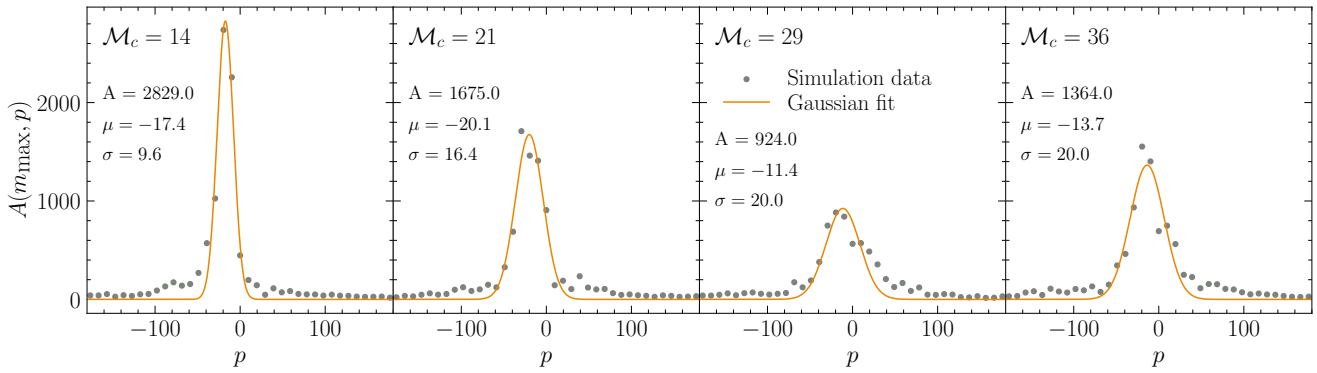

Fig. 9. Function $A(m_{\max}, p)$ for runs with $\langle Q \rangle = 1$ and varying $\mathcal{M}_c$ (as indicated in the panels), along with their Gaussian fits. Black points show the amplitude of the Fourier transform $A(m_{\max}, p)$ as a function of p (cf., Equation (10)), where $m_{\max}$ is the value of m for which $A(m, p)$ has its maximum. Orange lines show Gaussian fits to the data, with the amplitude A, mean μ, and dispersion σ of each fit as indicated in the legend.

expected for material arms being sheared by the differential rotation of the galaxy, since more rapid rotation of the inner regions winds up the arms. In terms of Figure 7, this corresponds to a systematic decrease in the slopes of the spiral features with time. This decrease is much more uniform in the $\mathcal{M}_c = 14$ and 21 cases when compared to the other two. Moreover, the spread in pitch angle systematically decreases with time for the $\mathcal{M}_c = 14$ and 21 runs but remains nearly constant, and a factor of two larger, for the $\mathcal{M}_c = 29$ and 36 runs. This difference reflects the more complex and clumpy morphology visible in the higher $\mathcal{M}_c$ runs.

3.3.2. Spacing

To quantify feather spacing we integrate the 2D transform over the p direction to yield $A(m) = \int A(m, p)\, \mathrm{d}p$. We find that $A(m)$ does not vary appreciably after $t_{\rm onset}$, and thus for simplicity we carry out our analysis only on the snapshots shown in Figure 7; results for other snapshots are qualitatively identical. As with our analysis of the pitch angle, we fit an empirically chosen functional form to $A(m)$; since m is a positive-definite quantity, we use a lognormal-like rather than a normal form,

$$A(m) = \frac{A_m}{m\sigma_m\sqrt{2\pi}} \exp\left[\frac{(\log m - \mu_m)^2}{2\sigma_m^2}\right], \tag{12}$$

where A_m is the amplitude, μ_m is the location of the peak in $\log m$, and σ_m is the width in $\log m$. In Figure 11 we show $A(m)$ along with our best empirical fits, the parameters for which we report in Table 3. The figure demonstrates that our chosen functional form provides a reasonable description of the data. From the empirical fit we extract the median, given by $m_{\rm fil} = \exp(\mu_m)$, as a representation of the dominant azimuthal mode, and the distribution's 16th and 84th percentiles given by $\exp(\mu_m \mp \sigma_m)$, as its lower and upper spread.

We show $m_{\rm fil}$ as a function of $\mathcal{M}_c$ for our four runs in Figure 12. The right vertical axis of this plot shows the physical spacing corresponding to this value of $m_{\rm fil}$, which is $\lambda_{\rm fil} = 2\pi R_{\rm gal}/m_{\rm fil}$, where $R_{\rm gal} = 3$ kpc is the mean radius of the annulus we use in our analysis. We find that the $m_{\rm fil}$ varies approximately linearly with $\mathcal{M}_c$. A χ^2 fit to this relationship of the form

$$m_{\rm fil} = a\mathcal{M}_c + b, \tag{13}$$

yields $a = 2.13 \pm 0.02$ and $b = -15.5 \pm 0.6$, and we show this fit via the black dashed line in Figure 12.

3.4. Feather density structure and evolution

Finally, we examine the three-dimensional density structure of the feathers. Our goal here is understanding how this depends on $\mathcal{M}_c$, and to see whether the feathers are likely to be sites for star formation. Figure 13, where we shows the mass-weighted probability density function (PDF) of $\log_{10}$ of $\rho/\rho_{\rm mid}$, where ρ is the density of the gas and $\rho_{\rm mid}$ is the radial average of the initial density of the region of interest. We do this for the cylindrical region bounded by 1 kpc thick radial annuli centred at 3 kpc. The left panel is for all the "feather forming" runs with $\langle Q \rangle = 1$

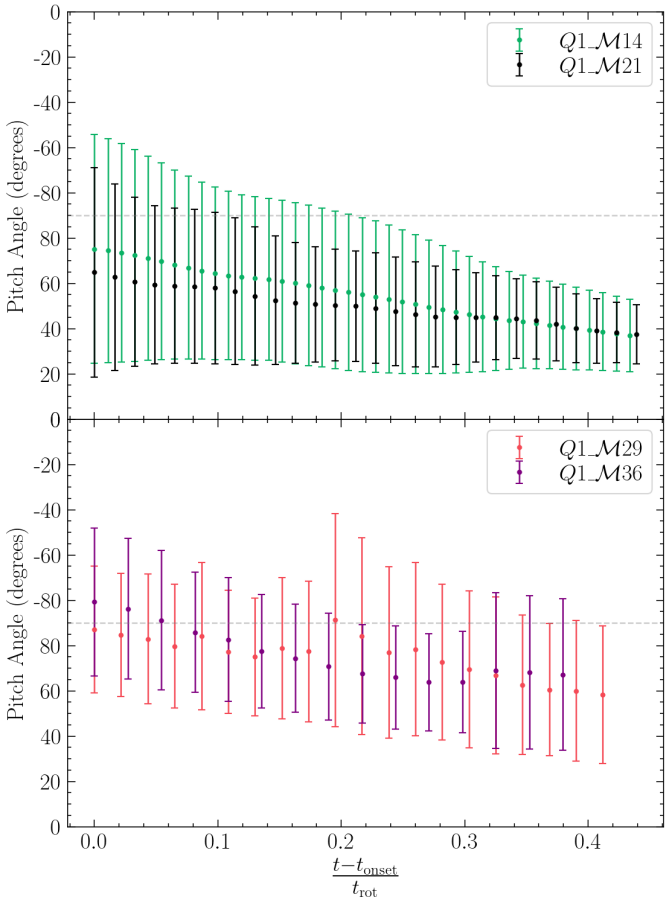

Fig. 10. Time evolution of the pitch angle, $\alpha = \tan^{-1}(-m/p)$, of the filaments in the runs with $\langle Q \rangle = 1$ and varying $\mathcal{M}_c$. The upper panel shows the $\mathcal{M}_c = 14$ and 21 runs, and the lower shows $\mathcal{M}_c = 29$ and 36. All panels show results after the onset of the instability, and all times are normalised by the rotation period of the galaxy at $R = 3$ kpc. Circular points represent the mean pitch angle and error bars show the standard deviation. The dashed line shows $\alpha = 90°$, that marks the transition between the trailing spirals with a positive pitch angles to leading spiral with negative ones. We see that all the runs show a decreasing trend in the pitch angle as the feathers get sheared due to differential rotation of the galaxy.

and varying $\mathcal{M}_c$ at times when they are similarly evolved; see snapshots in Figure 7. In the right panel we show the PDF at several different times for the $Q1\_\mathcal{M}36$ run.

In this plot, the stratified medium of the background galaxy corresponds to the parts of the PDF with $\rho/\rho_{\rm mid} \leq 1$. Filaments and further dense regions inside them are represented in the higher-density tails. Looking at the left panel, we can see that all of our runs form the high-density tail, which is expected from feather-forming galaxies. However, we also see a systematic trend that the higher $\mathcal{M}_c$ runs have longer tails extending towards higher densities. This densest part contains little mass and is largely de-coupled from the initial phase of the instability, and is instead driven by self-gravity.

To confirm the importance of self-gravity, in the right panel we add a vertical dashed line marking the Jeans density for the $Q1\_\mathcal{M}36$ run, defined as $\rho_{\rm Jeans} = (c_s/4\Delta x_{\rm min})^2(\pi/G)$, which is the density at which self-gravitating structures become unresolved on the grid scale (Truelove et al. 1997, formally, our expression is the density for which the Jeans length is equal to $4\Delta x_{\rm min}$). Here, c_s is the sound speed and $\Delta x_{\rm min}$ is the length of the grid cells. We see that the high-density tail of the PDF does not reach a steady-state, and instead rises until it reaches the Jeans density at our resolution. This likely indicates that the high-density tail of the PDF is made up of gas in a state of runaway collapse, where star formation is likely to occur in the future. A detailed study of how this star formation proceeds is beyond the scope of this work.

Table 3. Fit parameters for the lognormal-like fit (see Equation (12)) on $A(m)$ from our simulations at the times shown in Figure 11.

Model name	$A_m/10^6$	μ_m	σ_m
$Q1\_\mathcal{M}14$	2.95 ± 0.10	2.72 ± 0.03	0.78 ± 0.03
$Q1\_\mathcal{M}21$	3.88 ± 0.10	3.40 ± 0.03	0.80 ± 0.02
$Q1\_\mathcal{M}29$	5.59 ± 0.15	3.81 ± 0.02	0.69 ± 0.02
$Q1\_\mathcal{M}36$	7.87 ± 0.23	4.11 ± 0.03	0.82 ± 0.02

4. Discussion

In this section we discuss our results in the light of existing observational, numerical and theoretical works and point out limitations of our approach. In Section 4.1 we comment on the nature of instability that is responsible for feather formation, and in Section 4.2 we compare the filament spacing found in our simulations with observations of nearby galaxies. Lastly, in Section 4.3, we outline the limitations of our simulations and hint on future avenues.

4.1. Nature of instability

In order to better understand the physical mechanism responsible for feather formation in our simulations, we compare the mean azimuthal spacing of the filaments calculated in Section 3.3.2 to the length scales of various instabilities expected to be present in the disc: the wavelength of the most unstable Toomre mode (Toomre 1964), the Jeans length (Jeans 1902) in the galactic mid-plane, and the length scale of the Swing amplification mechanism (Fuchs 2001; Kim & Ostriker 2002; Meidt & van der Wel 2024). These are given by $\lambda_{\rm Toomre} = 2{c_s}^2/G\Sigma$, $\lambda_{\rm Jeans} = (\pi {c_s}^2/G\rho_{\rm mid})^{1/2}$ and $\lambda_{\rm Swing} = \lambda_{\rm Jeans} X_J$, respectively, where $\rho_{\rm mid}$ is the mid-plane density of the galaxy and X_J measures the characteristic length of the swing amplification in terms of the Jeans length and has been found to be $\approx$3 for a wide range of perturbing wavelengths (Meidt & van der Wel 2024); we adopt $X_J = 3$ exactly for our comparison.

These length scales all depend on the local properties of the disc, and thus vary with position and time within our analysis region. In order to reduce this complexity to a single parameter for each run, we take averages over our region of interest using the initial configurations in the simulations. Specifically, for each length scale λ, we defined

$$\langle \lambda \rangle = \frac{1}{R_{\rm out} - R_{\rm in}} \int_{R_{\rm in}}^{R_{\rm out}} \lambda(R, t = 0)\, {\rm d}R, \tag{14}$$

where $R_{\rm in} = 2$ kpc and $R_{\rm out} = 4$ kpc are the bounding radii of our annulus and $\lambda(R, t = 0)$ represents the length scale of interest evaluated for the initial disc state at radius R. We also compute the standard deviations of λ over this radial range, defined as

$$\sigma_\lambda = \left\{ \frac{1}{R_{\rm out} - R_{\rm in}} \int_{R_{\rm in}}^{R_{\rm out}} [\lambda(R, t = 0) - \langle \lambda \rangle]^2 \, {\rm d}R \right\}^{1/2}. \tag{15}$$

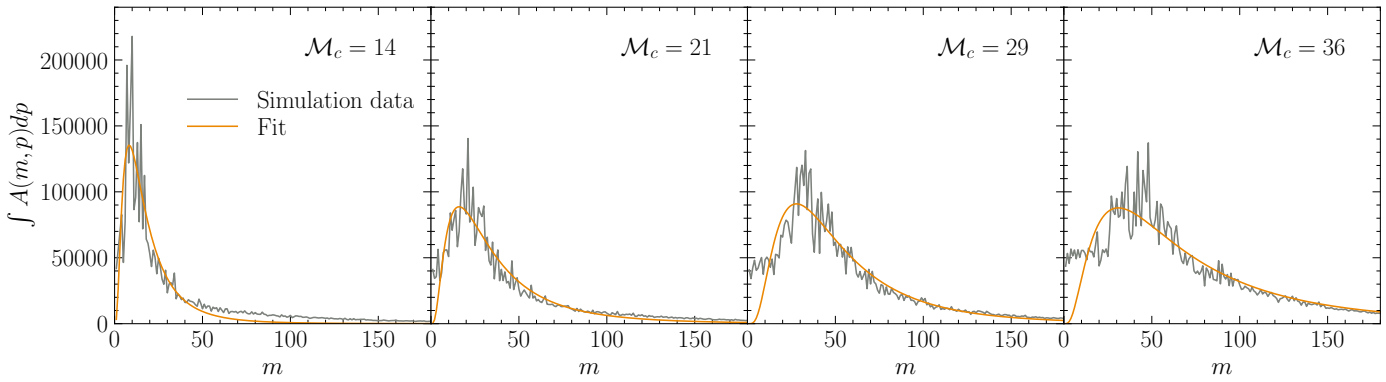

Fig. 11. Amplitude of the 2D Fourier transform $A(m, p)$ of the logarithmic surface density (see Equation (10)) in the region 2–4 kpc, integrated over p. Different panels are for runs with $\langle Q \rangle = 1$ and varying $\mathcal{M}_c$, evaluated at the same times as in Figure 6. The grey curves are simulation data and the orange ones are the empirical fits to the data (see text for details). We can see how the power shifts toward higher values of m with increasing $\mathcal{M}_c$.

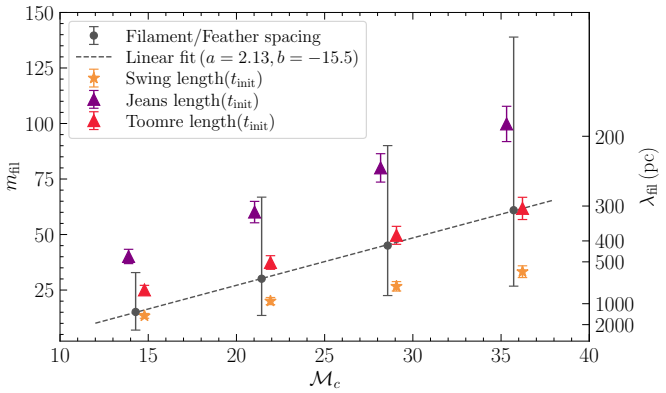

Fig. 12. Azimuthal mode of the filaments ($m_{\rm fil}$) and various instabilities, shown with the $\mathcal{M}_c$ ($\sim v_c/\sigma$) of our galaxies. Black circular points with error bars show the mean and 16th to 84th percentile range of the $m_{\rm fil}$ and corresponding physical spacing $\lambda_{\rm fil}$ for the snapshots shown in Figure 7. The dashed line is a linear fit to the median values of $m_{\rm fil}$ (Equation (13)). Purple, red, and orange points with error bars represent the radial averages $\langle \lambda \rangle$ and standard deviations σ_λ (Equation (14) and Equation (15)) of the wavelength of the most unstable Toomre mode, the Jeans length and the Swing amplification length – see main text for details. These points are slightly offset from their overlapping $\mathcal{M}_c$ values for visibility. The simulations show an increase in the median value of $m_{\rm fil}$ and a broadening of the 16th to 84th percentile range with increasing $\mathcal{M}_c$. The median filament spacing agrees well with the Toomre length of the $\mathcal{M}_c = 21, 29$ and 36 runs, and with the swing length for $\mathcal{M}_c = 14$ run.

We plot $\langle \lambda \rangle$ for each of our candidate length scales – Jeans, Toomre, and Swing – on top of values of $\lambda_{\rm fil}$ measured from our simulations in Figure 12; in this plot, the errorbars on the points are the standard deviations of the corresponding quantities. Comparing the theoretically-predicted length scales with the measured values of $\lambda_{\rm fil}$, first we note that except for the $\lambda_{\rm Jeans}$ in the $\mathcal{M}_c = 14$ case, all lie within the spread of the measured filament spacings, but that $\lambda_{\rm Jeans}$ is consistently the farthest from the measured value of $\lambda_{\rm fil}$. The other two length scales are closer to the measurements, with $\lambda_{\rm Toomre}$ lying very close to $\lambda_{\rm fil}$ for the $\mathcal{M}_c = 29$ and 36 runs, and $\lambda_{\rm Swing}$ matching it very closely for the $\mathcal{M}_c = 14$ case. The $\mathcal{M}_c = 21$ run lies at a transition for these two behaviours.

An appealing interpretation of this trend is that filament formation is driven by the Toomre instability in the two higher $\mathcal{M}_c$ cases, while Swing amplification dominates at lower $\mathcal{M}_c$. Such a transition is expected theoretically, because the threshold value of Q required to trigger Toomre instability increases with disc thickness (Wang et al. 2010), and the low $\mathcal{M}_c$ discs are thicker than the high $\mathcal{M}_c$ ones. Thus for our series of runs at fixed Q, we might expect Toomre instability to dominate in high $\mathcal{M}_c$ discs that are thin enough to trigger Toomre instability, and for the somewhat slower-growing Swing mechanism to dominate in thicker discs that are Toomre-stable. Our results also appear to be quantitatively consistent with this hypothesis. While the exact Q threshold for Toomre instability in a finite-thickness disc is somewhat sensitive to the exact vertical distribution of the gas, Wang et al. (2010) find typical thresholds of $\simeq$0.7–0.8 for discs with $\mathcal{M}_c$ in the range 16–24. Examining Figure 1, it is clear that our discs do not quite reach such small Q values in the feather forming region from 2–4 kpc, and thus it seems likely that our $\mathcal{M}_c = 14$ and 21 cases are Toomre stable, consistent with our finding that Swing amplification dominates in these.

Swing amplification also offers an explanation for the structure formation seen at very late times in the $\langle Q \rangle = 2$ run, which has a Q value well above the threshold for Toomre instability at all radii (Appendix C).

In observations it can be even more challenging to single out the mechanism that is directly responsible for filament formation since we do not have the option to simply "switch-off" physical processes that affect gas flows. Still, there is one observational study that analyses the emergence of galactic filaments as a consequence of gravitational instability (Meidt et al. 2023). They find that their four filament-forming galaxies have $Q \geq 1$, that is, above the more conservative Toomre threshold for razor-thin discs. While the galaxies could still form filaments via the Swing amplification, we point out that the inclusion of the major stellar component (Leroy et al. 2021) will bring down this Q value potentially making them gravitationally unstable (Romeo & Falstad 2013). Meidt et al. (2023) also find that the filament spacing in these galaxies is more comparable to the estimated Jeans length, rather than the Toomre length, which however, will also change with the inclusion of the stellar component. Given the high degree of complexity of the filaments observed in these galaxies, we believe that it is more likely that they are formed due to the Toomre-like galactic scale instability.

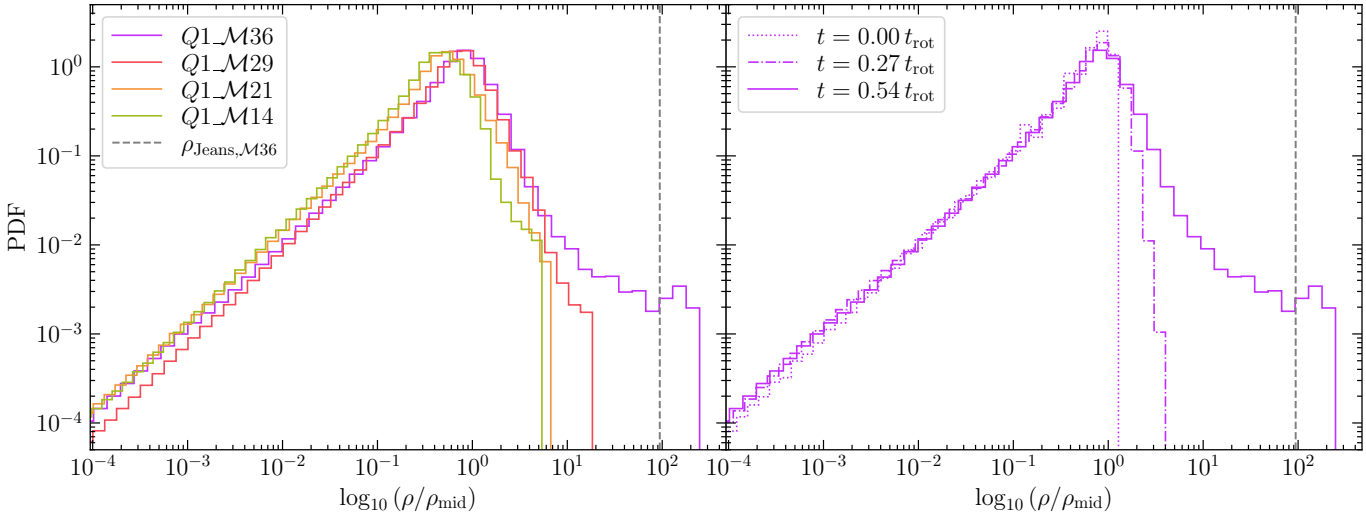

Fig. 13. Mass-weighted probability density function (PDF) of the $\log_{10}$ of the density normalised by the radially averaged mid-plane density, for the snapshots shown in Figure 7. The grey dashed line depicts the Jeans density (see text for details), at which we expect numerical effects to dominate. The left panel shows all the runs at times similar to Figure 7, and the right panel shows the time evolution of the $Q1\_\mathcal{M}36$ case leading up to the time in the left panel. We see that all the runs in the left panel form high-density tails that represent feathers and that the densest end of the tail is reaching the limit imposed by the resolution of our simulations.

We compare the filament spacings from observations with our simulations in the next section.

4.2. Comparison with observations

We now compare the filament spacing extracted from our simulations with those observed in nearby galaxies, adopting a fiducial radius of 3 kpc. We plot the filament spacing in our simulations together with observed filament spacings as a function of $\mathcal{M}_{\mathrm{c}}$ in Figure 14. In this plot we show the measured filament spacings from our simulations as black points with error bars, and the values shown match the right-axis values indicated in Figure 12; similarly, the dashed line shows the empirical curve given by Equation (13), and is identical to the dashed black line in Figure 12.

We draw the observations (shown as diamonds in Figure 14) from two sources: the JWST/MIRI 11.3 µm observations reported by Meidt et al. (2023, their Table 1), which we plot in yellow, and the HST archival data of La Vigne et al (2006, shown in blue), and with the feather spacing of these sources taken from the tabulation of Mandowara et al. (2022, their Table 4). Thilker et al. (2023) show that there is good agreement between filament catalogues derived from optical and IR data, and thus for the analysis that follows we will not differentiate between the two data sources. We extract the filament spacings and values of $\mathcal{M}_{\mathrm{c}}$ that we plot as follows. For the JWST observations, our central points correspond to the reported 50th percentile of the filament spacing, and our lower and upper error bars to the 16th and 84th percentiles, respectively, for the region $R \leq 4$ kpc; however, the choice of radius has little effect since Meidt et al. find no appreciable variation in filament spacing with galacto-centric radius. For the HST observations, Mandowara et al. report filament spacings at various galacto-centric radii, so to estimate the spacing at $R = 3$ kpc we assume that each galaxy is characterised by a single, global m_{fil} at all radii, which we extract by carrying out a simple χ^2 fit for m_{fil} to the radius-dependent values of λ_{fil} reported in Mandowara et al.'s Table 4; we then compute $\lambda_{\mathrm{fil}} = 2\pi R/m_{\mathrm{fil}}$ at $R = 3$ kpc. For $\mathcal{M}_{\mathrm{c}}$ in both sets of observations, we assume a fixed $c_{\mathrm{s}} = 7$ km s^{-1} for all galaxies, characteristic of the warm neutral medium (McClure-Griffiths et al. 2023), and take our circular velocities v_{c} from the saturated circular velocities of all galaxies calculated from CO (2–1) emission maps taken from Lang et al. (2020, their Table 4); we derive error bars in $\mathcal{M}_{\mathrm{c}}$ from their quoted uncertainties in v_{c}, assuming no uncertainty in c_{s}. The only exceptions to this are the galaxies IC 5332 and NGC 5055, which are not included in this sample. For NGC 5055, we use the H I rotation curve velocity from McGaugh & Schombert (2015) and for IC 5332 we adopt $v_{\mathrm{c}} = 120 \pm 20.6$ km s^{-1}, derived from a semi-empirical model that links the rotation curve to the stellar mass (Meidt et al. 2018), where the spread is propagated from the uncertainty in the galaxy's inclination angle (Leroy et al. 2021). These properties, along with the star formation rates (SFR) and total stellar masses (M_{stellar}), are tabulated in Table 4. The SFR and the M_{stellar} are taken from Leroy et al. (2021) for all but NGC 5055, which is taken from Leroy et al. (2019). Our sample consists of late-type main sequence star-forming galaxies.

From Figure 14, we can see that the filament spacing from our simulations agrees well with the observations despite the simplicity of our models. All but NGC 1365 fall within a factor of ∼2 of the median of our filament spacing. The trend of decreasing filament spacing with increasing $\mathcal{M}_{\mathrm{c}}$ predicted by the simulations is reproduced in the observational data, albeit with a fair amount of scatter since the data are sparse at both high and low $\mathcal{M}_{\mathrm{c}}$. The comparison is currently limited by the unavailability of kinematic data for many galaxies whose filament spacings have already been tabulated.

4.3. Limitations and future work

Our simulations consist of self-gravitating, isothermal gas. As a result, we miss some key physical processes pervasive in the ISM that are dynamically relevant on galactic scales. These include magnetic fields, cosmic rays, and feedback processes such as supernovae and winds from massive stars. Moreover, we use static analytical potentials to approximate the gravitational inter-

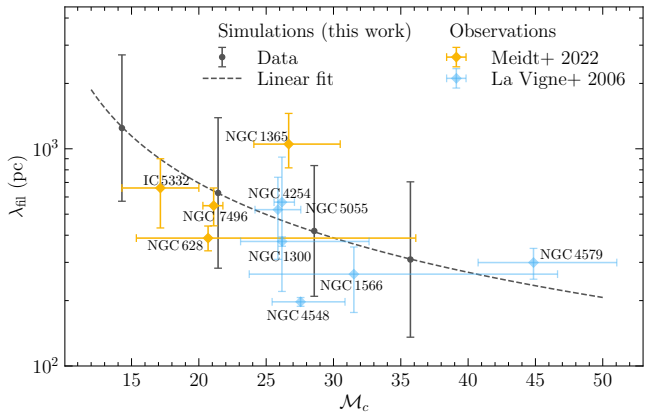

Fig. 14. Physical spacing of filaments as a function of the rotational Mach number, $\mathcal{M}_c$ ($\sim v_c/\sigma$), in our simulations (black circles; cf., Section 3.3.2) compared with observations (yellow and blue diamonds). The yellow diamonds are JWST/MIRI observations (Meidt et al. 2023) and the blue diamonds are HST observations (La Vigne et al. 2006). We see that, except for NGC 1365 and NGC 4548, the filament spacing extracted from our simulations agrees within the uncertainty ranges of the ones reported in the observations.

Table 4. Physical properties of the galaxies we use for comparison with our simulations.

Galaxy	$\lambda_{\rm fil}$ (pc)	v_c (km s^{-1})	$\log_{10}$ SFR ($M_\odot$ yr^{-1})	$\log_{10} M_{\rm stellar}$ ($M_\odot$)
NGC 628	388^{+49}_{-102} (1)	$144.8^{+108.0}_{-37.3}$	0.24	10.34
NGC 1365	1051^{+234}_{-404} (1)	$186.7^{+26.8}_{-18.1}$	1.24	10.99
IC 5332	660^{+228}_{-240} (1)	$120.0^{+20.6}_{-20.6}$	−0.39	9.67
NGC 7496	547^{+105}_{-113} (1)	$147.7^{+4.8}_{-5.6}$	0.35	10.00
NGC 1300	374^{+19}_{-19} (2)	$183.3^{+45.2}_{-21.6}$	0.07	10.62
NGC 1566	264^{+88}_{-88} (2)	$220.6^{+105.9}_{-54.4}$	0.66	10.79
NGC 4254	568^{+348}_{-348} (2)	$183.2^{+6.5}_{-4.1}$	0.49	10.42
NGC 4548	197^{+9}_{-9} (2)	$192.9^{+23.1}_{-14.8}$	−0.28	10.70
NGC 4579	299^{+48}_{-48} (2)	$314.0^{+43.3}_{-28.8}$	0.33	11.15
NGC 5055	525^{+215}_{-215} (2)	$181.1^{+11.9}_{-11.9}$	0.28	10.72

Notes. Star formation rates and stellar masses from Leroy et al. (2021) for all galaxies except NGC 5055, which is from Leroy et al. (2019). Feather spacing ($\lambda_{\rm fil}$) from 1 – Meidt et al. (2023); 2 – La Vigne et al. (2006) tabulated in Mandowara et al. (2022); circular velocities (v_c) from Lang et al. (2020) for all except NGC 5055 and IC 5332, which are from McGaugh & Schombert (2015) and Meidt et al. (2018), respectively.

action of stars and dark matter with the gas. Therefore, we miss the back-reaction of the former with the latter and vice-versa.

The inclusion of each of these aforementioned processes may affect feather formation and structure, acting as an additional source or damping mechanism for the perturbations or directly impacting the nature of the instability. For example, magnetic fields can have a stabilising effect due to the additional magnetic pressure. However, they are also known to destabilise the disc via Parker instability (Parker 1966; Körtgen et al. 2019; Arora et al. 2024) and the magneto-Jeans instability (Kim & Ostriker 2002). Further, since we expect star formation in feathers, energy and momentum injection due to feedback from stars may also affect their morphology. Finally, the presence of a live stellar component may destabilise the disc (Romeo & Wiegert 2011), which might lead to a shift in the Q thresholds for feather formation.

We point out, however, that the omission of these physical processes is intentional and motivated by our goal of conducting a clean numerical experiment to determine the role of gravity, rotation, and pressure alone in the formation of filaments, and to determine their morphological properties. Future studies will aim to incorporate more physical processes in order to study feather formation in more realistic galaxies. Future studies may also investigate the distribution of filament properties such as their masses, their velocity dispersion, and aspect ratios. The relative orientation of the filaments with respect to the local magnetic field is also of interest. These properties could help us gain insight into the variations of the initial conditions of star-forming regions residing inside feathers (for example; Thilker et al. 2023).

5. Summary

We simulate isothermal, self-gravitating, isolated disc galaxies that are initialised in equilibrium, with the aim of capturing structure formation via global gravitational instability. Our models are intentionally simplified, allowing us to isolate the dependence of structure formation on two dimensionless parameters: the radially averaged Toomre parameter $\langle Q \rangle$ and the rotational Mach number, $\mathcal{M}_c$. Our main conclusions are summarised below.

- Galaxies with $\langle Q \rangle = 1$ in the region $R \geq 2$ kpc form dense filaments and feathers within a single rotation, while galaxies with $\langle Q \rangle = 2, 3$ fail to form them within similar evolution times. This demonstrates that filaments can form solely due to galactic-scale instability driven by self-gravity overcoming the stabilising effect of rotation and thermal pressure. Thus filament formation occurs without the need for an external stellar spiral potential, magnetic fields, or supernova feedback. This does not prove that these other mechanisms cannot alternatively generate filaments, or that they do not modify the properties of filaments formed via gravitational instability; it simply establishes that gravitational instability alone is sufficient.
- The dense filaments that form in our simulations are kiloparsec long and semi-regularly spaced in azimuth. Their morphology and their density contrasts vary systematically with $\mathcal{M}_c$: morphological complexity increases with $\mathcal{M}_c$ and filament spacing varying as roughly $\mathcal{M}_c^{-1}$. Filament pitch angle decreases with time in all runs due to shearing by differential rotation, but the dispersion in pitch angle is larger at higher $\mathcal{M}_c$ as well. Filaments with a higher $\mathcal{M}_c$ also show density contrasts with longer tails that extend towards higher densities.
- The time required for onset of the filament forming instability varies $\mathcal{M}_c^{-1}$ as well; by contrast, the growth rate of variations in the density depends only weakly on $\mathcal{M}_c$, and is typically 30–50% of the galactic angular velocity. Highest for the run with higher $\mathcal{M}_c$.
- The filament spacings and their dependence on $\mathcal{M}_c$ found in our simulations are in good agreement with the characteristic length scales of the Toomre instability at higher $\mathcal{M}_c$, and with the length scale of the Swing amplification mechanism for lower $\mathcal{M}_c$. They are also consistent within observational uncertainties with values measured in nearby galaxies.

Our results demonstrate that the filamentary ISM structures revealed by modern telescopes and facilities such as the JWST

and ALMA in nearby galaxies with unprecedented resolution can at least potentially be understood as arising from very simple physical processes. Our numerical experiments show that self-gravity alone is sufficient to produce structures whose characteristics are in quantitative agreement with the observations. However, we are yet to see how this might change with the inclusion of other mechanisms such as magnetic fields, cosmic rays, or stellar feedback. In a forthcoming companion study we will quantify some of these effects.

Data availability

Movies associated to Fig. 7 are available at https://www.aanda.org

Acknowledgements. R. A. acknowledges funding by the Hamburg State Graduate Funding Program (HmbNFG) and heartfully thanks Sharon Meidt, Shivan Khullar, and Chris Matzner for insightful discussions and their enthusiasm. C. F. acknowledges funding provided by the Australian Research Council (Discovery Project grants DP230102280 and DP250101526), and the Australia-Germany Joint Research Cooperation Scheme (UA-DAAD). M. R. K. acknowledges support from the Australian Research Council through Laureate Fellowship FL220100020. We further acknowledge high-performance computing resources provided by the Leibniz Rechenzentrum and the Gauss Centre for Supercomputing (grants pr32lo, pr48pi and GCS Large-scale project 10391), the Australian National Computational Infrastructure (grants ek9 and jh2) and the Pawsey Supercomputing Centre (projects pawsey0807 and pawsey0810) in the framework of the National Computational Merit Allocation Scheme and the ANU Merit Allocation Scheme. The simulation software, FLASH, was in part developed by the Flash Centre for Computational Science at the University of Chicago and the Department of Physics and Astronomy at the University of Rochester.

References

Arora, R., Federrath, C., Banerjee, R., & Körtgen, B. 2024, A&A, 687, A276
Binney, J., & Tremaine, S. 1987, Galactic dynamics (Princeton, N.J.: Princeton University Press)
Chepurnov, A., Lazarian, A., Stanimirović, S., Heiles, C., & Peek, J. E. G. 2010, ApJ, 714, 1398
Dobbs, C. L., & Bonnell, I. A. 2006, MNRAS, 367, 873
Dubey, A., Fisher, R., Graziani, C., et al. 2008, in Numerical Modeling of Space Plasma Flows, eds. N. V. Pogorelov, E. Audit, & G. P. Zank, ASP Conf. Ser., 385, 145
Elmegreen, D. M. 1980, ApJ, 242, 528
Elmegreen, B. G., & Elmegreen, D. M. 2019, ApJS, 245, 14
Elmegreen, D. M., Elmegreen, B. G., Kaufman, M., et al. 2006, ApJ, 642, 158
Elmegreen, D. M., Elmegreen, B. G., Erroz-Ferrer, S., et al. 2014, ApJ, 780, 32
Elmegreen, B. G., Elmegreen, D. M., & Efremov, Y. N. 2018, ApJ, 863, 59
Federrath, C., Roman-Duval, J., Klessen, R. S., Schmidt, W., & Mac Low, M. 2010, A&A, 512, A81
Federrath, C., Sur, S., Schleicher, D. R. G., Banerjee, R., & Klessen, R. S. 2011, ApJ, 731, 62
Federrath, C., Roman-Duval, J., Klessen, R. S., Schmidt, W., & Mac Low, M. M. 2022, Astrophysics Source Code Library [record ascl:2204.001]
Fryxell, B., Olson, K., Ricker, P., et al. 2000, ApJS, 131, 273
Fuchs, B. 2001, A&A, 368, 107
Griv, E., & Gedalin, M. 2012, MNRAS, 422, 600
Griv, E., & Wang, H.-H. 2014, New Astron., 30, 8
Jeans, J. H. 1902, R. Soc. Lond. Philos. Trans. Ser. A, 199, 1
Jeffreson, S. M. R., Kruijssen, J. M. D., Keller, B. W., Chevance, M., & Glover, S. C. O. 2020, MNRAS, 498, 385
Khullar, S., Matzner, C. D., Murray, N., et al. 2024, ApJ, 973, 40
Kim, W.-T., & Ostriker, E. C. 2002, ApJ, 570, 132
Kim, W.-T., & Ostriker, E. C. 2006, ApJ, 646, 213
Kim, W.-T., Kim, Y., & Kim, J.-G. 2014, ApJ, 789, 68
Kim, Y., Kim, W.-T., & Elmegreen, B. G. 2015, ApJ, 809, 33
Kim, J.-H., Agertz, O., Teyssier, R., et al. 2016, ApJ, 833, 202
Kim, W.-T., Kim, C.-G., & Ostriker, E. C. 2020, ApJ, 898, 35
Körtgen, B., Banerjee, R., Pudritz, R. E., & Schmidt, W. 2019, MNRAS, 489, 5004
Kuhn, M. A., Benjamin, R. A., Zucker, C., et al. 2021, A&A, 651, L10
Lang, P., Meidt, S. E., Rosolowsky, E., et al. 2020, ApJ, 897, 122
La Vigne, M. A., Vogel, S. N., & Ostriker, E. C. 2006, ApJ, 650, 818
Lee, W.-K. 2014, ApJ, 792, 122
Lee, W.-K., & Shu, F. H. 2012, ApJ, 756, 45
Leroy, A. K., Sandstrom, K. M., Lang, D., et al. 2019, ApJS, 244, 24
Leroy, A. K., Schinnerer, E., Hughes, A., et al. 2021, ApJS, 257, 43
Levy, R. C., Bolatto, A. D., Teuben, P., et al. 2018, ApJ, 860, 92
Mandowara, Y., Sormani, M. C., Sobacchi, E., & Klessen, R. S. 2022, MNRAS, 513, 5052
McClure-Griffiths, N. M., Stanimirović, S., & Rybarczyk, D. R. 2023, ARA&A, 61, 19
McGaugh, S. S., & Schombert, J. M. 2015, ApJ, 802, 18
Meidt, S. E. 2022, ApJ, 937, 88
Meidt, S. E., & van der Wel, A. 2024, ApJ, 966, 62
Meidt, S. E., Leroy, A. K., Rosolowsky, E., et al. 2018, ApJ, 854, 100
Meidt, S. E., Rosolowsky, E., Sun, J., et al. 2023, ApJ, 944, L18
Pantaleoni González, M., Maíz Apellániz, J., Barbá, R. H., & Reed, B. C. 2021, MNRAS, 504, 2968
Parker, E. N. 1966, ApJ, 145, 811
Puerari, I., Elmegreen, B. G., & Block, D. L. 2014, AJ, 148, 133
Robinson, H., & Wadsley, J. 2024, MNRAS, 534, 1420
Romeo, A. B., & Falstad, N. 2013, MNRAS, 433, 1389
Romeo, A. B., & Wiegert, J. 2011, MNRAS, 416, 1191
Savchenko, S. S. 2012, Astrophys. Bull., 67, 310
Schinnerer, E., Meidt, S. E., Colombo, D., et al. 2017, ApJ, 836, 62
Shetty, R., & Ostriker, E. C. 2006, ApJ, 647, 997
Sormani, M. C., Sobacchi, E., Shore, S. N., Treß, R. G., & Klessen, R. S. 2017, MNRAS, 471, 2932
Thilker, D. A., Lee, J. C., Deger, S., et al. 2023, ApJ, 944, L13
Toomre, A. 1964, ApJ, 139, 1217
Tress, R. G., Sormani, M. C., Glover, S. C. O., et al. 2020, MNRAS, 499, 4455
Truelove, J. K., Klein, R. I., McKee, C. F., et al. 1997, ApJ, 489, L179
Veena, V. S., Schilke, P., Sánchez-Monge, Á., et al. 2021, ApJ, 921, L42
Wada, K., & Koda, J. 2004, MNRAS, 349, 270
Wang, H.-H., Klessen, R. S., Dullemond, C. P., van den Bosch, F. C., & Fuchs, B. 2010, MNRAS, 407, 705
Williams, T. G., Sun, J., Barnes, A. T., et al. 2022, ApJ, 941, L27
Zhao, B., Pudritz, R. E., Pillsworth, R., Robinson, H., & Wadsley, J. 2024, ApJ, submitted [arXiv:2405.18474]
Zucker, C., Battersby, C., & Goodman, A. 2015, ApJ, 815, 23

Appendix A: Dark matter potential

Here, we determine the stellar plus dark matter potential $\phi_{\rm dm}$ such that our disc is in radial equilibrium. In a reference frame that co-rotates with the disc angular frequency Ω at a given position (R, z), radial equilibrium demands that the sum of the gravitational, pressure, and centrifugal forces vanish. We can express this condition as

$$\rho \frac{\partial}{\partial R}\left(\phi_{\rm dm} + \phi_{\rm g}\right) + {c_{\rm s}}^2 \frac{\partial \rho}{\partial R} - \rho \Omega^2 R = 0, \tag{A.1}$$

where $\phi_{\rm g}$ is the potential due to disc self-gravity, which is given by Wang et al. (2010, their equation 29)

$$\phi_{\rm g} = 4\pi G \Sigma_\circ R_{\rm d} y^2 \left[I_0(y)K_0(y) - I_1(y)K_1(y)\right], \tag{A.2}$$

where $y = R/2R_{\rm d}$ and I_0, K_0, I_1, and K_1 are the modified Bessel functions of the first and second kind, of order zero and one.[2] To proceed we must now make some assumptions about the vertical structure of the disc and potential. We start by assuming that the radial variation in density is approximately exponential, $\rho(R) \propto \exp(-R/R_{\rm d})$. This assumption is exact only if the disc vertical profile is independent of radius, but is true approximately as long as the disc scale height does not vary on scales $\ll R_{\rm d}$; since this term is highly sub-dominant in any event (roughly 100× smaller than the centrifugal term), we do not seek a more accurate approximation. Finally, at the midplane we require that $\Omega = v_{\rm rot}/R$, but we must make an assumption about the variation of Ω in the z direction, or, equivalently, assume a shape for the centrifugal potential ψ, where $\partial\psi/\partial R = \Omega^2 R$. For this purpose we adopt the flattened centrifugal potential form suggested by Binney & Tremaine (1987),

$$\psi = \frac{{v_{\rm c}}^2}{2} \ln\left\{\frac{1}{R_{\rm c}^2}\left[R^2 + R_{\rm c}^2 + \left(\frac{z}{q}\right)^2\right]\right\}, \tag{A.3}$$

where q is a dimensionless parameter that determines the amount of flattening. One can readily verify that this potential satisfies our condition that $\partial\psi/\partial R = \Omega^2 R$. Following Binney & Tremaine's estimates for realistic galactic potentials, we adopt $q = 0.7$. With these assumptions, our equation of force balance reduces to

$$\rho \frac{\partial}{\partial R}\left(\phi_{\rm dm} + \phi_{\rm g} - {c_{\rm s}}^2 \frac{R}{R_d} - \psi\right) = 0, \tag{A.4}$$

which has the immediate solution

$$\phi_{\rm dm} = \psi - \phi_{\rm g} + {c_{\rm s}}^2 \frac{R}{R_{\rm d}}. \tag{A.5}$$

We have therefore succeeded in identifying the stellar plus dark matter potential required to place the disc in equilibrium.

Appendix B: Two dimensionless parameters

In this appendix we prove the assertion made in the main text that the fluid equations that we solve depend only upon the two dimensionless parameters $\langle Q\rangle$ and $\mathcal{M}_{\rm c}$. And that these together with the additional dimensionless parameters describing the initial conditions that we do not vary – $R_{\rm c}/R_{\rm d}$, $R_{\rm max}/R_{\rm d}$, q, α, and β – fully determine the evolution of the system. To do so, we non-dimensionalise the fluid variables via the transformations

$$\boldsymbol{r} = \boldsymbol{x} R_{\rm d}, \tag{B.1}$$

$$t = \tau \frac{R_{\rm d}}{c_{\rm s}}, \tag{B.2}$$

$$\boldsymbol{v} = \boldsymbol{u} c_{\rm s}, \tag{B.3}$$

$$\rho = a \frac{\Sigma_\circ}{R_{\rm d}}, \tag{B.4}$$

$$\tilde{\phi} = \frac{\phi}{{c_{\rm s}}^2}. \tag{B.5}$$

where x, τ, u, a, and $\tilde{\phi}$ are dimensionless length, time, velocity, density and the gravitational potential, respectively, scaled by the appropriate combinations of the disc scale length $R_{\rm d}$, the sound speed $c_{\rm s}$ and the surface density scaling of our galaxies $\Sigma_\circ$. The equations of mass and momentum conservation plus the Poisson equation under this transformation are

$$\frac{\partial a}{\partial \tau} + \frac{1}{\mathcal{M}_{\rm c}} \boldsymbol{\nabla}_{\boldsymbol{x}}(a\boldsymbol{u}) = 0, \tag{B.6}$$

$$\mathcal{M}_{\rm c} \frac{\partial \boldsymbol{u}}{\partial \tau} + (\boldsymbol{u}\cdot\nabla_x)\cdot\boldsymbol{u} = -\frac{\nabla_x a}{a} - \nabla_x\left(\tilde{\phi}_{\rm g} + \tilde{\phi}_{\rm dm}\right), \tag{B.7}$$

$$\nabla_x^2 \tilde{\phi} = \xi \frac{\mathcal{M}_{\rm c}}{\langle Q\rangle} a, \tag{B.8}$$

where ∇_x indicates gradient with respect to the dimensionless position variable $\mathbf{x}$ and ξ is a dimensionless constant given by

$$\begin{aligned}\xi &= \frac{4\sqrt{2}}{X_{\rm max}} \int_0^{X_{\rm max}} \frac{1}{\exp\left[-X - \beta\exp\left(-\alpha X\right)\right]} \frac{\sqrt{X^2 + 2X_{\rm c}^2}}{X^2 + X_{\rm c}^2}\, dX \\ &\approx 19.43.\end{aligned} \tag{B.9}$$

In the expression above, we have defined $X = R/R_{\rm d}$ as the dimensionless cylindrical radius, $X_{\rm c}$ and $X_{\rm max}$ are defined analogously, and the numerical evaluation is for our fixed values of these quantities, α, and β. Note that we have used the isothermal equation of state to substitute for the pressure (equation 3). Finally, we can rewrite the various components of the gravitational potential that contributed to $\tilde{\phi}$ using the same non-dimensionalisation procedure. Substituting into equation A.5 we have

$$\tilde{\phi}_{\rm dm} = \tilde{\psi} - \tilde{\phi}_{\rm g} + X, \tag{B.10}$$

$$\tilde{\psi} = \frac{\mathcal{M}_{\rm c}^2}{2} \ln\left\{X_{\rm c}^{-2}\left[X^2 + X_{\rm c}^2 + \left(\frac{Z}{q}\right)^2\right]\right\}, \tag{B.11}$$

$$\tilde{\phi}_{\rm g} = \frac{\mathcal{M}_{\rm c}}{\langle Q\rangle \xi} X^2 \left[I_0\left(\frac{X}{2}\right)K_0\left(\frac{X}{2}\right) - I_1\left(\frac{X}{2}\right)K_1\left(\frac{X}{2}\right)\right], \tag{B.12}$$

where $Z = z/R_{\rm d}$ is the dimensionless vertical height. This completes the non-dimensionalisation of the system, and demonstrates that the results depend only on $\langle Q\rangle$, $\mathcal{M}_{\rm c}$, $X_{\rm c}$, $X_{\rm max}$, q, α, and β as claimed.

Appendix C: Toomre $\langle Q\rangle = 2$ run

In this Appendix we present the long-term evolution of the $\langle Q\rangle = 2$ run ($Q2\_\mathcal{M}29$), which does not produce significant structure on the same $\sim t_{\rm rot}$ timescales as the $\langle Q\rangle = 1$ runs presented in the main body. We continue this run to time $t = 2.5\, t_{\rm rot}$, and show the projected surface density as a function of time in Figure C.1. We see that the galaxy does develop structures with

[2] Formally the expression that Wang et al. (2010) provide is for a purely exponential disc, without the central flattening we have introduced. However, since our disc differs in mass from a pure exponential disc by only ≈ 5%, we expect the difference in potential to be small.

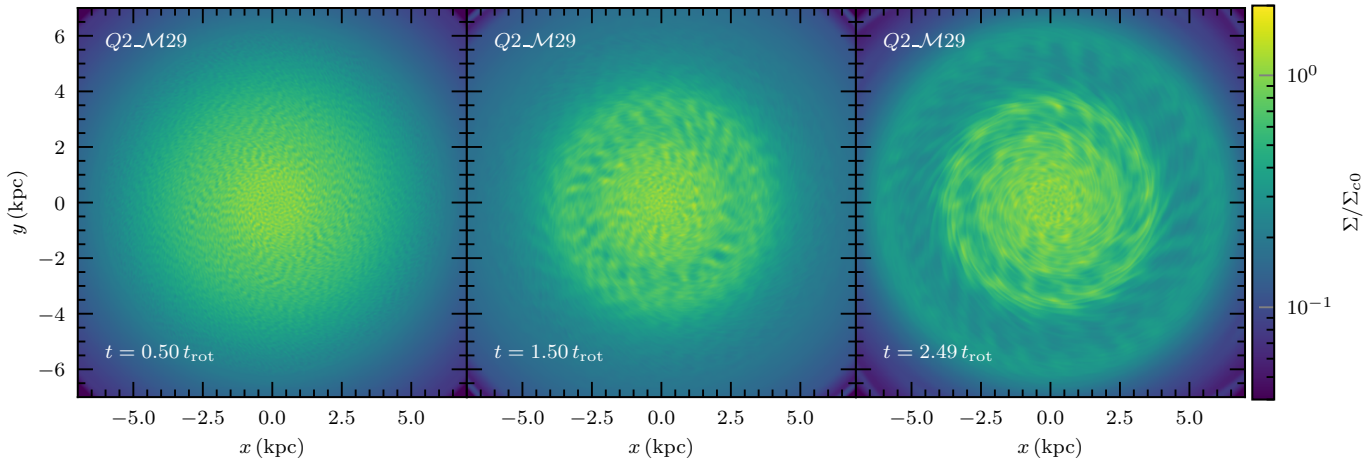

Fig. C.1. Same as Figure 2, but for the longer time evolution of the $Q = 2$ run. We see that there are faint structures at early times in the first two panels. The third panel shows a structure with somewhat more density contrast, visually confirming the slow growth of an instability.

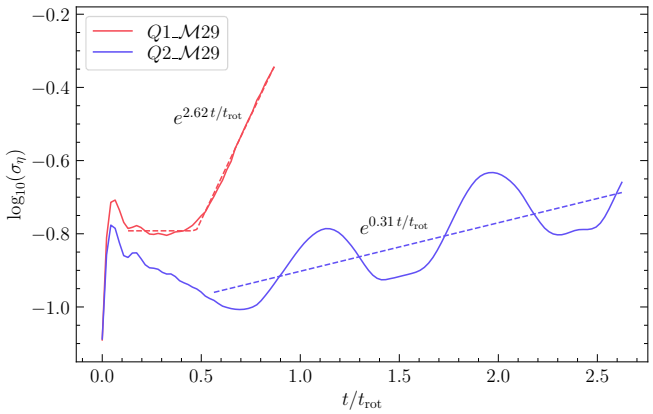

Fig. C.2. Same as Figure 5, but only for $Q1\_\mathcal{M}29$ and $Q2\_\mathcal{M}29$ runs, where the latter was evolved to a later time than shown in the main text. We see the oscillatory peaks in the $Q = 2$ run, but also a steady, yet slow growth over time. This growth is visibly smaller than in the $Q1\_\mathcal{M}29$ run.

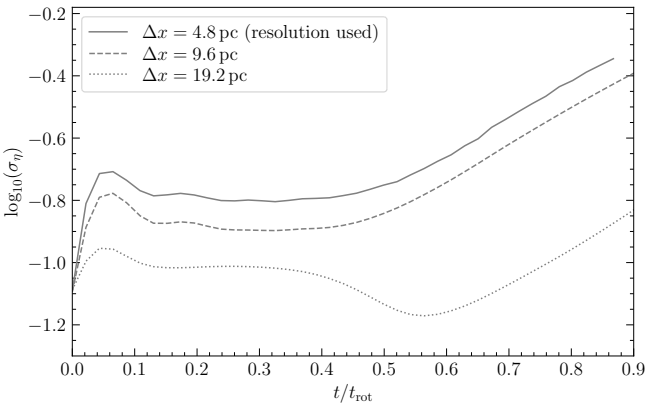

Fig. D.1. Same as Figure 5, but for the $Q1\_\mathcal{M}29$ run at three different resolutions. The solid line depicts the resolution used in the main text ($\Delta x = 4.8$ pc) and the other two lines are runs with resolutions reduced by a factor of two each.

noticeable density contrast by $t = 2.5\,t_{\rm rot}$ at $R = 3$ kpc, and that as in the $\langle Q \rangle = 1$ cases, these structures are regularly spaced in the azimuth. However, there are also significant differences. First, the structures in the $\langle Q \rangle = 2$ run clearly have lower pitch angles and density contrasts. Second, their azimuthal spacing is also different - counting the number of dense structures along the azimuth we estimate $m_{\rm fil} \simeq 15$ to be the dominant mode of the filaments. This is a factor of two less than the $Q1\_\mathcal{M}29$ run, that has the same $\mathcal{M}_{\rm c}$ value as the $\langle Q \rangle = 2$ run. Moreover, the number of filaments in the $Q2\_\mathcal{M}29$ case is around the value expected from the swing amplification mechanism, which is = 13.

To compare the growth rate of filaments of both the cases, we plot the time evolution of the variation of the logarithmic density contrast (σ_η) of the $Q1\_\mathcal{M}29$ run and the $Q2\_\mathcal{M}29$ run together in Figure C.2. This is similar to the left panel of the Figure 5, except for the x-axis that extends to longer times. The dashed lines show the empirical fit on the two runs. The $Q1\_\mathcal{M}29$ run has the piecewise-fit of the form equation 9, identical to the one shown in the right panel of the Figure 5. We fit only the exponential part of the fit for the $Q2\_\mathcal{M}29$ run after $t = 0.55\,t_{\rm rot}$, since we are interested exclusively in the rising part of the curve. As seen in the main text, the $Q2\_\mathcal{M}29$ shows an initial decline in σ_η. However, from $t \approx 0.55$ onwards, it shows periodic oscillations with a rising mean. From our empirical fit to this part of the curve, we find $\omega t_{\rm rot} = 0.31$, which is ≈ 8 times smaller than $Q1\_\mathcal{M}29$ case.

Appendix D: Resolution study

For a resolution study, we perform two runs with resolutions that are a factor of two ($\Delta x = 9.6$ pc) and four ($\Delta x = 19.2$ pc) lower than the one used in the main text. Similar to Figure 5, we show the time evolution of the standard deviation of the logarithmic surface density (defined in Equation (8)) of the annuli $R = 2$–4 kpc of the three runs in Figure D.1. We see similar qualitative evolution in all the three cases as seen for all the $\langle Q \rangle = 1$ runs. The steady value of σ_η after the initial relaxation relaxation phase increases with increasing resolution. This is expected since we resolve the initial turbulent velocity fluctuations and the resulting density fluctuations with more cells. However, this change in σ_η between runs with consecutive increasing resolutions is less than a factor of two. The time of the onset of exponential growth, as well as the slopes of the lines following the onset are very similar, especially for the two runs with the highest resolutions.

4 Conclusion

Using controlled numerical experiments, we explored the role of self-gravity, magnetic fields and spiral arms in seeding dense structure in disc galaxies via galactic instabilities. This outlines the role of galactic-scale processes in organising the dense, semi-regularly spaced structure observed in nearby galaxies that decides the initial conditions and environment for star formation.

4.1 Summary

4.1.1 Paper I

In the first part of the project, we quantified the effects of pervasive magnetic fields on the spiral arm instability. For this, we run a suite of 3D global simulations of isolated galaxies with self-gravity, magnetic fields, optically thin heating and cooling and an external spiral potential with varying initial magnetisation.
We find that magnetic fields affects the instability, regardless of their initial strength. In the case of moderate initial magnetic fields ($\beta_{\rm init} = 10$), they completely stabilize the spiral arm against fragmentation due to the added magnetic pressure that support against compression. This in contrast to the unstable arms in the hydrodynamical $\beta = \infty$ and weak field $\beta = 50$ cases. In the weak initial magnetic field ($\beta_{\rm init} = 50$) run, the magnetic fields, at first, follow the fluid flow and get aligned with the spiral arms. As a consequence of this, the initial evolution of the disc is similar to the hydrodynamic case ($\beta = \infty$). However, the magnetic fields also get amplified due to compression, field tangling and cooling, and rise to equipartition levels within the spiral arms as the gas is funnelled into spirals due to the external spiral arm potential. As a result, we form dense spiral arms with equipartition magnetic fields within them ($\beta_{\rm arm} \sim 1$). This ultimately leads to differences in the spiral arm instability between the $\beta = 50$ and the $\beta = \infty$ cases. We find that, not only do the magnetic fields increase the cloud spacings and the length-scale of operation of the instability, but also increase its growth rate within a factor of two. This later effect is in contrast with existing 2D linear studies that report a stabilising effect of magnetic fields due to the additional magnetic pressure. Thus, we find that the three-dimensional environment was crucial for capturing the effects of magnetic fields in its entirety. The increased growth rates and the change in the length scales of the formed clouds both agree with the linear calculations of the Parker instability. Moreover, a zoom-in 3D visualisation of a spiral arm, as it was undergoing fragmentation revealed the characteristic hill and valley structure associated with the instability. These are indications that Parker instability could have played a role in aiding cloud formation in the magnetic case. The physical spacing of over-densities that result from the spiral arm instability in both the hydrodynamical and magnetic case fall within the range of available observations of cloud spacings along spiral arms.

4.1.2 Paper II

In the second part of our work, we turned our attention to the origin of inter-arm dense features called feathers. The origin of this feature had previously been attributed by several works to different physical processes. Many works connecting it to the spiral arm instability, the Parker instability of large scale magnetic fields or correlated

supernovae feedback in the spiral arms. However, we demonstrated that self-gravity by itself, can form feathers in galaxies via global gravitational instability. Independent of the need/presence of spiral arms, magnetic fields or supernovae.
For this, we used numerical experiments of 3D, high-resolution, isothermal disc galaxies that start-out in equilibrium. The minimal-setup of our simulations allows us to define all our models with just two dimensionless parameters. This is the disc averaged Toomre-$\langle Q \rangle$ and the rotational mach number $\mathcal{M}_{\rm c}$. These quantify the gravitational stability of the disc and the relative contribution of the rotation to the pressure respectively. As expected from gravitational instability, we find that discs with $\langle Q \rangle = 1$ are unstable to feather formation while $\langle Q \rangle > 1$ are not. The formed feathers are kiloparsec-scale features semi-regularly spaced in the azimuth. We find that while $\langle Q \rangle$ dictates feather formation, their morphology, onset time of formation and density contrasts depend upon the $\mathcal{M}_{\rm c}$. The morphological complexity and the density contrast increase with $\mathcal{M}_{\rm c}$, with filament spacing and onset time varying as $\mathcal{M}_{\rm c}^{-1}$. The timescale of formation is only weakly dependent upon $\mathcal{M}_{\rm c}$, with growth rates $\sim 0.5\ \Omega$. Moreover, we test the empirical scaling of feather spacings with $\mathcal{M}_{\rm c}$ found in our work with JWST/MIRI and HST observations of nearby galaxies and find them to be in agreement. This shows that the regularity of these dense galactic structures may be explained by the simple action of a large scale gravitational instability on the gas, and the variety in observed spacings could be a result of the natural variation in the $\mathcal{M}_{\rm c}$ of galaxies.
Paper I and Paper II, together, also demonstrate that the formation of clouds/overdensities from the spiral arm instability does not guarantee their shearing into the inter-arm region to form feathers, as was put-forward in many prior works.

4.2 Future work

Although our work shows that gravitational instability may be enough for feather formation, it does not rule out the possibility of feather formation being affected by other physical mechanisms. This opens up future avenues of exploration. Magnetic fields, as outlined in Section 1.4.3 and as seen in our work on the spiral arm instability, can fundamentally change the nature of gas flows and instabilities in the disc. Thus, a natural step forward is their inclusion in the setup.
After studying galactic-scale instabilities and the effects of magnetic fields on dense structure formation in galaxies. We could also further expand the study to molecular cloud scales that are directly relevant to the process of star formation. Our current resolution, however, does not allow this and we would need to employ a zoom-in technique for the same. This would allow us to quantify the effects of galactic environment on the star formation efficiency in a self-consistent manner.

References

Aditya, K. (2023, June). Stability of galaxies across morphological sequence. *MNRAS 522*(2), 2543–2552.

Agertz, O., F. Renaud, S. Feltzing, J. I. Read, N. Ryde, E. P. Andersson, M. P. Rey, T. Bensby, and D. K. Feuillet (2021, June). VINTERGATAN - I. The origins of chemically, kinematically, and structurally distinct discs in a simulated Milky Way-mass galaxy. *MNRAS 503*(4), 5826–5845.

Armstrong, J. W., B. J. Rickett, and S. R. Spangler (1995, April). Electron Density Power Spectrum in the Local Interstellar Medium. *ApJ 443*, 209.

Asplund, M., N. Grevesse, A. J. Sauval, and P. Scott (2009, September). The Chemical Composition of the Sun. *ARA&A 47*(1), 481–522.

Baade, W. (1963). *Evolution of Stars and Galaxies*.

Bailey, M. E., C. J. Butler, and J. McFarland (2005, April). Bailey, Butler, McFarland: Discovery of Spiral Nebulae: Unwinding the discovery of spiral nebulae. *Astronomy and Geophysics 46*(2), 2.26–2.28.

Balbus, S. A. and J. F. Hawley (1991, July). A Powerful Local Shear Instability in Weakly Magnetized Disks. I. Linear Analysis. *ApJ 376*, 214.

Balbus, S. A. and J. F. Hawley (1998, January). Instability, turbulence, and enhanced transport in accretion disks. *Reviews of Modern Physics 70*(1), 1–53.

Basu, S., T. C. Mouschovias, and E. V. Paleologou (1997, May). Dynamical Effects of the Parker Instability in the Interstellar Medium. *ApJ 480*(1), L55–L58.

Beck, R., L. Chamandy, E. Elson, and E. G. Blackman (2020). Synthesizing observations and theory to understand galactic magnetic fields: Progress and challenges. *Galaxies 8*(1).

Binney, J. (2020, July). The shearing sheet and swing amplification revisited. *MNRAS 496*(1), 767–783.

Binney, J. and S. Tremaine (1987). *Galactic dynamics*.

Chakrabarti, S., G. Laughlin, and F. H. Shu (2003, October). Branch, Spur, and Feather Formation in Spiral Galaxies. *ApJ 596*(1), 220–239.

Chandrasekhar, S. (1961). *Hydrodynamic and hydromagnetic stability*. Oxford University Press.

Chevance, M., M. R. Krumholz, A. F. McLeod, E. C. Ostriker, E. W. Rosolowsky, and A. Sternberg (2023, July). The Life and Times of Giant Molecular Clouds. In S. Inutsuka, Y. Aikawa, T. Muto, K. Tomida, and M. Tamura (Eds.), *Protostars and Planets VII*, Volume 534 of *Astronomical Society of the Pacific Conference Series*, pp. 1.

Choudhuri, A. R. (1998). *The Physics of Fluids and Plasmas: An Introduction for Astrophysicists*. "Cambridge University Press".

Chown, R., A. K. Leroy, K. Sandstrom, J. Chastenet, J. Sutter, E. W. Koch, H. B. Koziol, L. Neumann, J. Sun, T. G. Williams, D. Baron, G. S. Anand, A. T. Barnes, Z. Bazzi, F. Belfiore, A. Bolatto, M. Boquien, Y. Cao, M. Chevance, D. Colombo, D. A. Dale, O. V. Egorov, C. Eibensteiner, E. Emsellem, H. Hassani, J. D. Henshaw, H. He, J. Kim, K. Kreckel, S. E. Meidt, E. J. Murphy, E. K. Oakes, E. C. Ostriker, H.-A. Pan, D. Pathak, E. Rosolowsky, S. K. Sarbadhicary, E. Schinnerer, and Y.-H. Teng (2024, October). Polycyclic Aromatic Hydrocarbon and CO(2-1) Emission at 50-150 pc Scales in 66 Nearby Galaxies. *arXiv e-prints*, arXiv:2410.05397.

Cox, D. P. (2005, September). The Three-Phase Interstellar Medium Revisited. *ARA&A 43*(1), 337–385.

Dale, J. E. (2015, October). The modelling of feedback in star formation simulations. *New A Rev. 68*, 1–33.

Dobbs, C. and J. Baba (2014, September). Dawes Review 4: Spiral Structures in Disc Galaxies. *PASA 31*, e035.

Efremov, Y. N. (2009, August). Regularities in the distribution of star/gas complexes in the spiral arms of our galaxy and M31. *Astronomy Letters 35*(8), 507–517.

Efremov, Y. N. (2010, July). On the chains of star complexes and superclouds in spiral arms. *MNRAS 405*(3), 1531–1543.

Elmegreen, B. G. (1987, January). Supercloud Formation by Nonaxisymmetric Gravitational Instabilities in Sheared Magnetic Galaxy Disks. *ApJ 312*, 626.

Elmegreen, B. G. (1995, August). An effective Q parameter for two-fluid instabilities in spiral galaxies. *MNRAS 275*(4), 944–950.

Elmegreen, B. G. (2011, August). Gravitational Instabilities in Two-component Galaxy Disks with Gas Dissipation. *ApJ 737*(1), 10.

Elmegreen, B. G. and D. M. Elmegreen (1983, April). Regular strings of HII regions and superclouds in spiral galaxies : clues to the origin of cloudy structure. *MNRAS 203*, 31–45.

Elmegreen, B. G. and D. M. Elmegreen (1987, September). H i Superclouds in the Inner Galaxy. *ApJ 320*, 182.

Elmegreen, B. G. and D. M. Elmegreen (2019, November). Highly Embedded 8 μm cores of Star Formation in the Spiral Arms and Filaments of 15 Nearby Disk Galaxies. *ApJS 245*(1), 14.

Elmegreen, B. G., D. M. Elmegreen, and Y. N. Efremov (2018, August). Regularly Spaced Infrared Peaks in the Dusty Spirals of Messier 100. *ApJ 863*(1), 59.

Elmegreen, D. M. (1980, December). Properties of spurs in spiral galaxies. *ApJ 242*, 528–532.

Elmegreen, D. M., B. G. Elmegreen, S. Erroz-Ferrer, J. H. Knapen, Y. Teich, M. Popinchalk, E. Athanassoula, A. Bosma, S. Comerón, Y. N. Efremov, D. A. Gadotti, A. Gil de Paz, J. L. Hinz, L. C. Ho, B. Holwerda, T. Kim, J. Laine, E. Laurikainen, K. Menéndez-Delmestre, T. Mizusawa, J.-C. Muñoz-Mateos, M. W. Regan, H. Salo, M. Seibert, and K. Sheth (2014, January). Embedded Star Formation in S^4G Galaxy Dust Lanes. *ApJ 780*(1), 32.

Elmegreen, D. M., B. G. Elmegreen, M. Kaufman, K. Sheth, C. Struck, M. Thomasson, and E. Brinks (2006, May). Spitzer Space Telescope IRAC and MIPS Observations of the Interacting Galaxies IC 2163 and NGC 2207: Clumpy Emission. *ApJ 642*(1), 158–170.

Federrath, C. and R. S. Klessen (2012, December). The Star Formation Rate of Turbulent Magnetized Clouds: Comparing Theory, Simulations, and Observations. *ApJ 761*, 156.

Fensch, J. and F. Bournaud (2021, August). The role of gas fraction and feedback in the stability and evolution of galactic discs: implications for cosmological galaxy formation models. *MNRAS 505*(3), 3579–3589.

Fensch, J., F. Bournaud, N. Brucy, Y. Dubois, P. Hennebelle, and J. Rosdahl (2023, April). Universal gravity-driven isothermal turbulence cascade in disk galaxies. *Astronomy & Astrophysics 672*, A193.

Ferrière, K. (2020, January). Plasma turbulence in the interstellar medium. *Plasma Physics and Controlled Fusion 62*(1), 014014.

Foglizzo, T. and M. Tagger (1994, July). The Parker instability in disks with differential rotation. *A&A 287*, 297–319.

Fuchs, B. (2001, March). Density waves in the shearing sheet. I. Swing amplification. *A&A 368*, 107–121.

Fujimoto, M. (1966, November). Gas flows through a model spiral arm. *AJ 71*, 856.

Goldbaum, N. J., M. R. Krumholz, and J. C. Forbes (2016, August). Mass Transport and Turbulence in Gravitationally Unstable Disk Galaxies. II: The Effects of Star Formation Feedback. *ApJ 827*, 28.

Goldreich, P. and D. Lynden-Bell (1965, January). II. Spiral arms as sheared gravitational instabilities. *MNRAS 130*, 125.

Goodman, A. A., J. Alves, C. N. Beaumont, R. A. Benjamin, M. A. Borkin, A. Burkert, T. M. Dame, J. Jackson, J. Kauffmann, T. Robitaille, and R. J. Smith (2014, December). The Bones of the Milky Way. *ApJ 797*(1), 53.

Griv, E. and M. Gedalin (2012, May). Stability of galactic discs: finite arm-inclination and finite-thickness effects. *MNRAS 422*(1), 600–609.

Gusev, A. S. and Y. N. Efremov (2013, September). Regular chains of star formation complexes in spiral arms of NGC 628. *MNRAS 434*(1), 313–324.

Gusev, A. S. and E. V. Shimanovskaya (2020, August). Spatial regularity of the young stellar population in the ring of NGC 6217. *A&A 640*, L7.

Gusev, A. S., E. V. Shimanovskaya, and N. A. Zaitseva (2022, August). Spatial regularity of the young stellar population in spiral arms of late-type galaxies NGC 895, NGC 5474, and NGC 6946. *MNRAS 514*(3), 3953–3964.

Hanawa, T. and D. Kikuchi (2012, July). Dynamical Stability of Galactic Shocks: Numerical Instability and Physical Stability. In N. V. Pogorelov, J. A. Font, E. Audit, and G. P. Zank (Eds.), *Numerical Modeling of Space Plasma Slows (ASTRONUM 2011)*, Volume 459 of *Astronomical Society of the Pacific Conference Series*, pp. 310.

Hartmann, J. (1904, May). Investigations on the spectrum and orbit of delta Orionis. *ApJ 19*, 268–286.

Heintz, E., C. Bustard, and E. G. Zweibel (2020, March). The Role of the Parker Instability in Structuring the Interstellar Medium. *ApJ 891*(2), 157.

Hennebelle, P., R. Banerjee, E. Vázquez-Semadeni, R. S. Klessen, and E. Audit (2008, August). From the warm magnetized atomic medium to molecular clouds. *A&A 486*(3), L43–L46.

Hennebelle, P. and G. Chabrier (2011, December). Analytical Star Formation Rate from Gravoturbulent Fragmentation. *ApJ 743*, L29.

Herschel, W. (1785, January). On the Construction of the Heavens. *Philosophical Transactions of the Royal Society of London Series I 75*, 213–266.

Jeffreson, S. M. R., J. M. D. Kruijssen, B. W. Keller, M. Chevance, and S. C. O. Glover (2020, October). The role of galactic dynamics in shaping the physical properties of giant molecular clouds in Milky Way-like galaxies. *MNRAS 498*(1), 385–429.

Jog, C. J. (1996, January). Local stability criterion for stars and gas in a galactic disc. *MNRAS 278*(1), 209–218.

Jog, C. J. and P. M. Solomon (1984, January). Two-fluid gravitational instabilities in a galactic disk. *ApJ 276*, 114–126.

Johns, T. C. and A. H. Nelson (1986, May). Global simulations of gas flow in disc galaxies. I - Response to a spiral density wave. *MNRAS 220*, 165–183.

Julian, W. H. and A. Toomre (1966, December). Non-Axisymmetric Responses of Differentially Rotating Disks of Stars. *ApJ 146*, 810.

Kennicutt, Jr., R. C. (1989, September). The Star Formation Law in Galactic Disks. *ApJ 344*, 685.

Kennicutt, Jr., R. C. (1998, May). The Global Schmidt Law in Star-forming Galaxies. *ApJ 498*(2), 541–552.

Khullar, S., C. D. Matzner, N. Murray, M. Y. Grudić, D. Guszejnov, A. Wetzel, and P. F. Hopkins (2024, September). Playing with FIRE: A Galactic Feedback-halting Experiment Challenges Star Formation Rate Theories. *ApJ 973*(1), 40.

Kim, J., M. Chevance, J. M. D. Kruijssen, A. Schruba, K. Sandstrom, A. T. Barnes, F. Bigiel, G. A. Blanc, Y. Cao, D. A. Dale, C. M. Faesi, S. C. O. Glover, K. Grasha, B. Groves, C. Herrera, R. S. Klessen, K. Kreckel, J. C. Lee, A. K. Leroy, J. Pety, M. Querejeta, E. Schinnerer, J. Sun, A. Usero, J. L. Ward, and T. G. Williams (2021, June). On the duration of the embedded phase of star formation. *MNRAS 504*(1), 487–509.

Kim, W., E. C. Ostriker, and J. M. Stone (2002, December). Three-dimensional Simulations of Parker, Magneto-Jeans, and Swing Instabilities in Shearing Galactic Gas Disks. *The Astrophysical Journal 581*(2), 1080–1100.

Kim, W.-T., C.-G. Kim, and E. C. Ostriker (2020, July). Local Simulations of Spiral Galaxies with the TIGRESS Framework. I. Star Formation and Arm Spurs/Feathers. *ApJ 898*(1), 35.

Kim, W.-T., Y. Kim, and J.-G. Kim (2014, July). Nature of the Wiggle Instability of Galactic Spiral Shocks. *ApJ 789*(1), 68.

Kim, W.-T. and E. C. Ostriker (2001, September). Amplification, Saturation, and Q Thresholds for Runaway: Growth of Self-Gravitating Structures in Models of Magnetized Galactic Gas Disks. *The Astrophysical Journal 559*(1), 70–95. arXiv:astro-ph/0105375.

Kim, W.-T. and E. C. Ostriker (2002, May). Formation and Fragmentation of Gaseous Spurs in Spiral Galaxies. *ApJ 570*(1), 132–151.

Kim, W.-T. and E. C. Ostriker (2006a, July). Formation of Spiral-Arm Spurs and Bound Clouds in Vertically Stratified Galactic Gas Disks. *ApJ 646*(1), 213–231.

Kim, W.-T. and E. C. Ostriker (2006b, July). Formation of Spiral-Arm Spurs and Bound Clouds in Vertically Stratified Galactic Gas Disks. *ApJ 646*(1), 213–231.

Kim, W.-T., E. C. Ostriker, and J. M. Stone (2003, December). Magnetorotationally Driven Galactic Turbulence and the Formation of Giant Molecular Clouds. *ApJ 599*(2), 1157–1172.

Kim, Y., W.-T. Kim, and B. G. Elmegreen (2015, August). WIGGLE INSTABILITY OF GALACTIC SPIRAL SHOCKS: EFFECTS OF MAGNETIC FIELDS. *The Astrophysical Journal 809*(1), 33. Publisher: The American Astronomical Society.

Kim, Y., W.-T. Kim, and B. G. Elmegreen (2015, August). Wiggle Instability of Galactic Spiral Shocks: Effects of Magnetic Fields. *ApJ 809*(1), 33.

Kjellgren, K., P. Girichidis, J. Göller, N. Brucy, R. S. Klessen, R. G. Tress, J. Soler, C. Pfrommer, M. Werhahn, S. C. O. Glover, R. Smith, L. Testi, and S. Molinari (2025, February). The dynamical impact of cosmic rays in the Rhea magnetohydrodynamics simulations. *arXiv e-prints*, arXiv:2502.02635.

Kolmogorov, A. (1941, January). The Local Structure of Turbulence in Incompressible Viscous Fluid for Very Large Reynolds' Numbers. *Akademiia Nauk SSSR Doklady 30*, 301–305.

Körtgen, B., R. Banerjee, R. E. Pudritz, and W. Schmidt (2019, November). Global dynamics of the interstellar medium in magnetized disc galaxies. *MNRAS 489*(4), 5004–5021.

Koyama, H. and S.-I. Inutsuka (2000, April). Molecular Cloud Formation in Shock-compressed Layers. *ApJ 532*(2), 980–993.

Koyama, H. and S.-i. Inutsuka (2002, January). An Origin of Supersonic Motions in Interstellar Clouds. *ApJ 564*(2), L97–L100.

Krumholz, M. R. (2014, June). The big problems in star formation: The star formation rate, stellar clustering, and the initial mass function. *Physics Reports 539*(2), 49–134.

Krumholz, M. R. and C. F. McKee (2005, September). A General Theory of Turbulence-regulated Star Formation, from Spirals to Ultraluminous Infrared Galaxies. *ApJ 630*, 250–268.

Kuznetsov, V. D. and V. S. Ptuskin (1983, July). Stability of the equilibrium distributions of interstellar gas, cosmic rays, and magnetic field in an external gravitational field. *Ap&SS 94*(1), 5–21.

La Vigne, M. A., S. N. Vogel, and E. C. Ostriker (2006, October). A Hubble Space Telescope Archival Survey of Feathers in Spiral Galaxies. *ApJ 650*(2), 818–834.

Lai, T. S. Y., J. D. T. Smith, S. Baba, H. W. W. Spoon, and M. Imanishi (2020, December). All the PAHs: An AKARI-Spitzer Cross-archival Spectroscopic Survey of Aromatic Emission in Galaxies. *ApJ 905*(1), 55.

Larson, R. B. (1981, March). Turbulence and star formation in molecular clouds. *MNRAS 194*, 809–826.

Lee, W.-K. (2014, September). Feathering Instability of Spiral Arms. II. Parameter Study. *ApJ 792*(2), 122.

Lee, W.-K. and F. H. Shu (2012, September). Feathering Instability of Spiral Arms. I. Formulation of the Problem. *ApJ 756*(1), 45.

Leroy, A. K., E. Schinnerer, A. Hughes, E. Rosolowsky, J. Pety, A. Schruba, A. Usero, G. A. Blanc, M. Chevance, E. Emsellem, C. M. Faesi, C. N. Herrera, D. Liu, S. E. Meidt, M. Querejeta, T. Saito, K. M. Sandstrom, J. Sun, T. G. Williams, G. S. Anand, A. T. Barnes, E. A. Behrens, F. Belfiore, S. M. Benincasa, I. Bešlić, F. Bigiel, A. D. Bolatto, J. S. den Brok, Y. Cao, R. Chandar, J. Chastenet, I.-D. Chiang, E. Congiu, D. A. Dale, S. Deger, C. Eibensteiner, O. V. Egorov, A. García-Rodríguez, S. C. O. Glover, K. Grasha, J. D. Henshaw, I. T. Ho, A. A. Kepley, J. Kim, R. S. Klessen, K. Kreckel, E. W. Koch, J. M. D. Kruijssen, K. L. Larson, J. C. Lee, L. A. Lopez, J. Machado, N. Mayker, R. McElroy, E. J. Murphy, E. C. Ostriker, H.-A. Pan, I. Pessa, J. Puschnig, A. Razza, P. Sánchez-Blázquez,

F. Santoro, A. Sardone, F. Scheuermann, K. Sliwa, M. C. Sormani, S. K. Stuber, D. A. Thilker, J. A. Turner, D. Utomo, E. J. Watkins, and B. Whitmore (2021, December). PHANGS-ALMA: Arcsecond CO(2-1) Imaging of Nearby Star-forming Galaxies. *ApJS 257*(2), 43.

Leroy, A. K., F. Walter, F. Bigiel, A. Usero, A. Weiss, E. Brinks, W. J. G. de Blok, R. C. Kennicutt, K.-F. Schuster, C. Kramer, H. W. Wiesemeyer, and H. Roussel (2009, June). Heracles: The HERA CO Line Extragalactic Survey. *AJ 137*(6), 4670–4696.

Leroy, A. K., F. Walter, E. Brinks, F. Bigiel, W. J. G. de Blok, B. Madore, and M. D. Thornley (2008, December). The Star Formation Efficiency in Nearby Galaxies: Measuring Where Gas Forms Stars Effectively. *AJ 136*, 2782–2845.

Lynds, B. T. (1970, January). The Distribution of Dark Nebulae in Late-Type Spirals. In W. Becker and G. I. Kontopoulos (Eds.), *The Spiral Structure of our Galaxy*, Volume 38 of *IAU Symposium*, pp. 26.

MacNeice, P., K. M. Olson, C. Mobarry, R. de Fainchtein, and C. Packer (2000, April). PARAMESH: A parallel adaptive mesh refinement community toolkit. *Computer Physics Communications 126*(3), 330–354.

Mandowara, Y., M. C. Sormani, E. Sobacchi, and R. S. Klessen (2022, July). The physical origin and the properties of arm spurs/feathers in local simulations of the wiggle instability. *MNRAS 513*(4), 5052–5075.

McGee, R. X. and J. A. Milton (1964, March). A sky survey of neutral hydrogen at λ 21 cm. III. Gas at higher radial velocities. *Australian Journal of Physics 17*, 128.

Meidt, S. E., E. Rosolowsky, J. Sun, E. W. Koch, R. S. Klessen, A. K. Leroy, E. Schinnerer, A. T. Barnes, S. C. O. Glover, J. C. Lee, A. Van Der Wel, E. J. Watkins, T. G. Williams, F. Bigiel, M. Boquien, G. A. Blanc, Y. Cao, M. Chevance, D. A. Dale, O. V. Egorov, E. Emsellem, K. Grasha, J. D. Henshaw, J. M. D. Kruijssen, K. L. Larson, D. Liu, E. J. Murphy, J. Pety, M. Querejeta, T. Saito, K. M. Sandstrom, R. J. Smith, M. C. Sormani, and D. A. Thilker (2023, February). PHANGS–JWST First Results: Interstellar Medium Structure on the Turbulent Jeans Scale in Four Disk Galaxies Observed by JWST and the Atacama Large Millimeter/submillimeter Array. *The Astrophysical Journal Letters 944*(2), L18.

Meidt, S. E. and A. van der Wel (2024, May). Bottom's Dream and the Amplification of Filamentary Gas Structures and Stellar Spiral Arms. *ApJ 966*(1), 62.

Mouschovias, T. C. (1974, August). Static Equilibria of the Interstellar Gas in the Presence of Magnetic and Gravitational Fields: Large-Scale Condensations. *ApJ 192*, 37–50.

Mouschovias, T. C. (1996). The Parker Instability in the Interstellar Medium. In K. C. Tsinganos (Ed.), *Solar and Astrophysical Magnetohydrodynamic Flows*, pp. 475–504. Dordrecht: Springer Netherlands.

Mouschovias, T. C., M. W. Kunz, and D. A. Christie (2009, July). Formation of interstellar clouds: Parker instability with phase transitions. *MNRAS 397*(1), 14–23.

Mulcahy, D. D., R. Beck, and G. H. Heald (2017, April). Resolved magnetic structures in the disk-halo interface of NGC 628. *A&A 600*, A6.

Ostriker, E. C. and R. Shetty (2011, April). Maximally Star-forming Galactic Disks. I. Starburst Regulation Via Feedback-driven Turbulence. *ApJ 731*(1), 41.

Padoan, P. and Å. Nordlund (2011, March). The Star Formation Rate of Supersonic Magnetohydrodynamic Turbulence. *ApJ 730*, 40.

Parker, E. N. (1966, September). The Dynamical State of the Interstellar Gas and Field. *ApJ 145*, 811.

Pessa, I., E. Schinnerer, A. K. Leroy, E. W. Koch, E. Rosolowsky, T. G. Williams, H.-A. Pan, A. Schruba, A. Usero, F. Belfiore, F. Bigiel, G. A. Blanc, M. Chevance, D. Dale, E. Emsellem, J. Gensior, S. C. O. Glover, K. Grasha, B. Groves, R. S. Klessen, K. Kreckel, J. M. D. Kruijssen, D. Liu, S. E. Meidt, J. Pety, M. Querejeta, T. Saito, P. Sanchez-Blazquez, and E. J. Watkins (2022, July). Variations in the $\Sigma_{\rm sfr} - \Sigma_{\rm mol} - \Sigma$ plane across galactic environments in PHANGS galaxies. *Astronomy & Astrophysics 663*, A61.

Proshina, I. S., A. V. Moiseev, and O. K. Sil'chenko (2022, March). Young Star-Forming Complexes in the Ring of the S0 Galaxy NGC 4324. *Astronomy Letters 48*(3), 139–152.

Ragan, S. E., T. Henning, J. Tackenberg, H. Beuther, K. G. Johnston, J. Kainulainen, and H. Linz (2014, August). Giant molecular filaments in the Milky Way. *A&A 568*, A73.

Roberts, W. W. (1969, October). Large-Scale Shock Formation in Spiral Galaxies and its Implications on Star Formation. *ApJ 158*, 123.

Roberts, Jr., W. W. (1970, January). Large-Scale Galactic Shock Phenomena and the Implications on Star Formation. In W. Becker and G. I. Kontopoulos (Eds.), *The Spiral Structure of our Galaxy*, Volume 38 of *IAU Symposium*, pp. 415.

Rodrigues, L. F. S., G. R. Sarson, A. Shukurov, P. J. Bushby, and A. Fletcher (2016, January). The Parker Instability in Disk Galaxies. *ApJ 816*(1), 2.

Romeo, A. B. and J. Wiegert (2011, September). The effective stability parameter for two-component galactic discs: is $Q^{-1} \approx {Q^{-1}}_{stars} + {Q^{-1}}_{gas}$? *MNRAS 416*(2), 1191–1196.

Rosse, T. E. O. (1850, January). Observations on the Nebulae. *Philosophical Transactions of the Royal Society of London Series I 140*, 499–514.

Safronov, V. S. (1960, February). On the gravitational instability in flattened systems with axial symmetry and non-uniform rotation. *Annales d'Astrophysique 23*, 979.

Sandstrom, K. M., E. W. Koch, A. K. Leroy, E. Rosolowsky, E. Emsellem, R. J. Smith, O. V. Egorov, T. G. Williams, K. L. Larson, J. C. Lee, E. Schinnerer, D. A. Thilker, A. T. Barnes, F. Belfiore, F. Bigiel, G. A. Blanc, A. D. Bolatto, M. Boquien, Y. Cao, J. Chastenet, M. Chevance, I.-D. Chiang, D. A. Dale, C. M. Faesi, S. C. O.

Glover, K. Grasha, B. Groves, H. Hassani, J. D. Henshaw, A. Hughes, J. Kim, R. S. Klessen, K. Kreckel, J. M. D. Kruijssen, L. A. Lopez, D. Liu, S. E. Meidt, E. J. Murphy, H.-A. Pan, M. Querejeta, T. Saito, A. Sardone, M. C. Sormani, J. Sutter, A. Usero, and E. J. Watkins (2023, February). PHANGS-JWST First Results: Tracing the Diffuse Interstellar Medium with JWST Imaging of Polycyclic Aromatic Hydrocarbon Emission in Nearby Galaxies. *ApJ 944*(2), L8.

Schinnerer, E., S. E. Meidt, D. Colombo, R. Chandar, C. L. Dobbs, S. García-Burillo, A. Hughes, A. K. Leroy, J. Pety, M. Querejeta, C. Kramer, and K. F. Schuster (2017, February). The PdBI Arcsecond Whirlpool Survey (PAWS): The Role of Spiral Arms in Cloud and Star Formation. *ApJ 836*(1), 62.

Schmidt, M. (1959, March). The Rate of Star Formation. *ApJ 129*, 243.

Shetty, R. and E. C. Ostriker (2006, August). Global Modeling of Spur Formation in Spiral Galaxies. *ApJ 647*(2), 997–1017.

Shu, F. H. (1968, January). On the Effects of Finite Disk Thickness and Gas Content on Spiral Structure. *The Astronomical Journal Supplement 73*, 201.

Shukurov, A. and K. Subramanian (2021). *Astrophysical Magnetic Fields: From Galaxies to the Early Universe*. Cambridge Astrophysics. Cambridge University Press.

Sun, J., A. K. Leroy, E. C. Ostriker, S. Meidt, E. Rosolowsky, E. Schinnerer, C. D. Wilson, D. Utomo, F. Belfiore, G. A. Blanc, E. Emsellem, C. Faesi, B. Groves, A. Hughes, E. W. Koch, K. Kreckel, D. Liu, H.-A. Pan, J. Pety, M. Querejeta, A. Razza, T. Saito, A. Sardone, A. Usero, T. G. Williams, F. Bigiel, A. D. Bolatto, M. Chevance, D. A. Dale, J. Gensior, S. C. O. Glover, K. Grasha, J. D. Henshaw, M. J. Jiménez-Donaire, R. S. Klessen, J. M. D. Kruijssen, E. J. Murphy, L. Neumann, Y.-H. Teng, and D. A. Thilker (2023, March). Star Formation Laws and Efficiencies across 80 Nearby Galaxies. *ApJ 945*(2), L19.

Tharakkal, D., A. Shukurov, F. A. Gent, G. R. Sarson, and A. Snodin (2023a, October). Steady states of the Parker instability: the effects of rotation. *MNRAS 525*(2), 2972–2984.

Tharakkal, D., A. Shukurov, F. A. Gent, G. R. Sarson, and A. Snodin (2023b, October). Steady states of the Parker instability: the effects of rotation. *MNRAS 525*(2), 2972–2984.

Thilker, D. A., J. C. Lee, S. Deger, A. T. Barnes, F. Bigiel, M. Boquien, Y. Cao, M. Chevance, D. A. Dale, O. V. Egorov, S. C. O. Glover, K. Grasha, J. D. Henshaw, R. S. Klessen, E. Koch, J. M. D. Kruijssen, A. K. Leroy, R. A. Lessing, S. E. Meidt, F. Pinna, M. Querejeta, E. Rosolowsky, K. M. Sandstrom, E. Schinnerer, R. J. Smith, E. J. Watkins, T. G. Williams, G. S. Anand, F. Belfiore, G. A. Blanc, R. Chandar, E. Congiu, E. Emsellem, B. Groves, K. Kreckel, K. L. Larson, D. Liu, I. Pessa, and B. C. Whitmore (2023, February). PHANGS-JWST First Results: The Dust Filament Network of NGC 628 and Its Relation to Star Formation Activity. *ApJ 944*(2), L13.

Thompson, T. A., E. Quataert, and N. Murray (2005, September). Radiation Pressure-supported Starburst Disks and Active Galactic Nucleus Fueling. *ApJ 630*(1), 167–185.

Toomre, A. (1964, May). On the gravitational stability of a disk of stars. *ApJ 139*, 1217–1238.

Vandervoort, P. O. (1970, July). Density Waves in a Highly Flattened, Rapidly Rotating Galaxy. *ApJ 161*, 87.

Vazquez-Semadeni, E., G. C. Gomez, A. K. Jappsen, J. Ballesteros-Paredes, R. F. Gonzalez, and R. S. Klessen (2007, March). Molecular Cloud Evolution. II. From Cloud Formation to the Early Stages of Star Formation in Decaying Conditions. *The Astrophysical Journal 657*(2), 870–883.

Veena, V. S., P. Schilke, Á. Sánchez-Monge, M. C. Sormani, R. S. Klessen, F. Schuller, D. Colombo, T. Csengeri, M. Mattern, and J. S. Urquhart (2021, November). A Kiloparsec-scale Molecular Wave in the Inner Galaxy: Feather of the Milky Way? *ApJ 921*(2), L42.

Wada, K. and J. Koda (2004, March). Instabilities of spiral shocks - I. Onset of wiggle instability and its mechanism. *MNRAS 349*(1), 270–280.

Wang, B. and J. Silk (1994, June). Gravitational Instability and Disk Star Formation. *ApJ 427*, 759.

Wang, H.-H., R. S. Klessen, C. P. Dullemond, F. C. van den Bosch, and B. Fuchs (2010, September). Equilibrium initialization and stability of three-dimensional gas discs. *MNRAS 407*(2), 705–720.

Weaver, H. F. (1970, January). Some Characteristics of Interstellar Gas in the Galaxy. In H. J. Habing (Ed.), *Interstellar Gas Dynamics*, Volume 39 of *IAU Symposium*, pp. 22.

Williams, T. G., J. Sun, A. T. Barnes, E. Schinnerer, J. D. Henshaw, S. E. Meidt, M. Querejeta, E. J. Watkins, F. Bigiel, G. A. Blanc, M. Boquien, Y. Cao, M. Chevance, O. V. Egorov, E. Emsellem, S. C. O. Glover, K. Grasha, H. Hassani, S. Jeffreson, M. J. Jiménez-Donaire, J. Kim, R. S. Klessen, K. Kreckel, J. M. D. Kruijssen, K. L. Larson, A. K. Leroy, D. Liu, I. Pessa, J. Pety, F. Pinna, E. Rosolowsky, K. M. Sandstrom, R. Smith, M. C. Sormani, S. Stuber, D. A. Thilker, and B. C. Whitmore (2022, December). PHANGS-JWST First Results: Spurring on Star Formation: JWST Reveals Localized Star Formation in a Spiral Arm Spur of NGC 628. *ApJ 941*(2), L27.

Zucker, C., C. Battersby, and A. Goodman (2015, December). The Skeleton of the Milky Way. *ApJ 815*(1), 23.